DEVELOPMENT AND VALIDATION OF DISSIPATIVE PARTICLE DYNAMICS WITH ENERGY CONSERVATION PARTICLE METHOD TO SIMULATE SHOCK RESPONSE OF HIGH ENERGETIC MATERIALS AT MICROMETER LENGTH SCALES

A Dissertation
Presented to
The Academic Faculty

By

Parveen Sood

In Partial Fulfillment
Of the Requirements for the Degree
Master of Science in Materials Science and Engineering

Georgia Institute of Technology

December 2014

DEVELOPMENT AND VALIDATION OF DISSIPATIVE PARTICLE DYNAMICS WITH ENERGY CONSERVATION PARTICLE METHOD TO SIMULATE SHOCK RESPONSE OF HIGH ENERGETIC MATERIALS AT MICROMETER LENGTH SCALES

Dr. Sunil K. Dwivedi, Advisor
School of Materials Science and Engineering
Georgia Institute of Technology

Dr. Sathya V. Hanagud
School of Aerospace Engineering
Georgia Institute of Technology

Dr. David McDowell
School of Materials Science and Engineering
Georgia Institute of Technology

Dr. Naresh Thadhani
School of Materials Science and Engineering
Georgia Institute of Technology

Dr. Arun M. Gokhale
School of Materials Science and Engineerng
Georgia Institute of Technology

Dr. John K. Brennan
Weapons and Materials Research Directorate
U.S. Army Research Lab

Date Approved: 08 14, 2014

ACKNOWLEDGEMENTS

I wish to thank Dr. Sunil K. Dwivedi for his advice and financial support during the duration of this research project. I also wish to thank Georgia Tech for providing the office facilities and related infrastructure so that this research project can be accomplished. I also wish to express my regards and appreciation for the graduate office of MSE department at GaTech for their time and patience with the huge amount of paperwork that they have to process for a graduate student. They have always been very helpful.

I also wish to sincerely thank Prof. Thadhani for his time and support during the execution of this project. Despite his busy schedule, he was able to make himself available and give valuable contributions both as a member of my thesis committee and as the chair of MSE. I also wish to thank my thesis committee for their time, continued support and valuable feedback.

I wish to convey my sincere gratitude to all my friends and colleagues in the High Strain Rate Lab from whom I have learnt a lot about shock propagation in materials. I wish to thank all my friends outside of the workplace for their support.

Finally, I wish to thank Defence Threat Reduction Agency (DTRA) and the program monitor, Dr. Suhithi Peiris at DTRA for sponsoring this project through DTRA award number HDTRA1-12-1-0004.

TABLE OF CONTENTS

page

LIST OF TABLES

page

LIST OF FIGURES

page

NOMENCLATURE

${}^{t}\mathbf{r}_i$, ${}^{t+\Delta t}\mathbf{r}_i$	Position of particle ‘i’ at time t and $t+\Delta t$ respectively
${}^{0}\mathbf{r}_i$, ${}^{0}\mathbf{r}_j$	Position vectors of particle ‘i' and ‘j’ in the reference configuration
${}^{t}\mathbf{v}_i$, ${}^{t+\Delta t}\mathbf{v}_i$	Velocity of particle ‘i’ at time t and $t+\Delta t$ respectively
${}^{t}\mathbf{p}_i$, ${}^{t+\Delta t}\mathbf{p}_i$	Momentum of particle ‘i’ at time t and $t+\Delta t$ respectively
${}^{t}\mathbf{f}_i$	Total force acting on particle ‘i’
${}^{t}\mathbf{F}_{ij}^{P}$	Conservative force acting on particle ‘i’ due to particle ‘j’
${}^{t}\mathbf{F}_{ij}^{D}$	Dissipative force acting on particle ‘i’ due to particle ‘j’
${}^{t}\mathbf{F}_{ij}^{R}$	Random force acting on particle ‘i’ due to particle ‘j’
${}^{t}\mathbf{F}_{ij}^{v}$	Artificial viscosity force acting on particle ‘i’ due to particle ‘j’
${}^{t}\mathbf{F}_{i}^{ext}$	External force acting on particle ‘i’
$\mathbf{F}_i^C$	Resultant conservative force on particle i
$\mathbf{F}_{ij}^C$	Conservative force between pair of particles ‘i’and ‘j’
γ_{ij}, γ	Amplitude of the dissipative force
σ_{ij}, σ	Amplitude of the random force
ω^D	Weight function of the dissipative force
ω^R	Weight function of the random force
A	Area of cross section

NOMENCLATURE (Contd.)

Δt	Time step
r_c	Cutoff distance for random and dissipative interaction
${}^t r_{ij}$, r	Distance between particles 'i' and 'j' at time t
r	Distance between the particles
${}^t \mathbf{n}_{ij}$	Unit vector from particle 'j' to 'i'
${}^t \mathbf{r}_{ij}$	${}^t \mathbf{r}_i - {}^t \mathbf{r}_j$
${}^t \mathbf{v}_{ij}$	${}^t \mathbf{v}_i - {}^t \mathbf{v}_j$
${}^t \mathbf{p}_{ij}$	${}^t \mathbf{p}_i - {}^t \mathbf{p}_j$
α_{LJ}	Force parameter of the Lennard-Jones interaction
m, n	m and n parameters of Lennard-Jones interaction
u_i	Internal energy of particle 'i'
C_v	Specific heat
θ_i , θ_j	Meso temperature of particle 'i' and 'j'
Θ_{ij}^{-1}	Harmonic mean of θ_i and θ_j
C_1 and C_2	Constants of artificial viscosity force
κ_{ij}	Mesoscopic thermal conductivity
ω^{Dq} and ω^{Rq}	Weight functions of dissipative and random forces for heat conduction
ζ_{ij}	Random number from the normal distribution

NOMENCLATURE (Contd.)

ρ_p	Probability Density
T	Temperature
ρ_p^{eq}	Probability density at equilibrium
ρ	Mass Density
$\mathbf{p}$	Momentum density
E^0	Energy density
ρ_n	Number Density of DPD particles
m_i	Mass of particle ‘i'
a_{ij} , a	Repulsion parameter of DPD fluid
p	Virial pressure
V	Volume of the simulation cell
α	Thermal diffusivity
$\boldsymbol{\sigma}_K$	Kinetic component of stress tensor
$\boldsymbol{\sigma}_P$	Potential component of stress tensor
$\boldsymbol{\sigma}_T$	$\left(\boldsymbol{\sigma}_K + \boldsymbol{\sigma}_P\right)$, Total Stress tensor
$B\left({}^t\mathbf{r}_i, {}^t\mathbf{r}_j, \mathbf{R}\right)$	Bond function
$\mathbf{R}$	Field point in Hardy’s averaging
$\mathbf{X}$	Field point in material coordinates
Δ	Localization function

NOMENCLATURE (Contd.)

$\mathbf{u}$	Mass averaged velocity
u^{α}, u^{β}	α and β components of mass averaged velocity, $\mathbf{u}$
${}^{t}\mathbf{w}_i$	${}^{t}\mathbf{v}_i - \mathbf{u}$
k_B	Boltzmann constant

SUMMARY

There is a need for a unified framework to simulate mesoscale response of high energetic (HE) materials at micron and submicron length scales. Dissipative Particle Dynamics with Energy Conservation (DPDE) particle method is a relatively recent simulation method that holds promise, due to the built-in conservation of mass, momentum and energy coupled with a sound statistical mechanics foundation for fluctuation-dissipation phenomena to naturally account for heat transport. Developed for gases and liquids at atomic and molecular length scales and later extended to polymeric liquids and coarse grained solids, it has not been extended, to the best of our knowledge, to simulate the mesoscale response of solids at micron and sub-micron length scales. This work presents the development of DPDE method and its extension to simulate shock response of solid HE materials at micron and sub-micron length scales. Validation, at various stages of development, was performed through simulations of equation-of-state of a DPD fluid, thermal equilibrium of ideal gas, Fourier heat transfer in an RDX slab, and quasi-static compression of an RDX sample. The Fourier heat transfer simulation yielded the fluctuation-dissipation parameter, κ_0, which was used in all the simulations. In-depth simulations were carried out to simulate the shock response of RDX under assumed planar parallel plate impact experiment conditions at 208 m/s and 876 m/s impact velocities. In-situ average response parameters were obtained by incorporating Hardy's averaging method extended, for the first time, to yield converged values at micron length scale. The free surface velocity, longitudinal and lateral stresses, and in-situ mass density were predicted in accordance with the uniaxial shock propagation

theory. The artificial viscosity force was added to DPDE for the first time, and yielded smooth temporal profiles of these quantities similar to those found in the results from hydrocode simulations. The variation in parameters of the Lennard-Jones form of the inter-particle potential force used in this work provided variation in in-situ mass density and stresses in accordance with RDX stiffness reduction introduced by the variation. The computed shock velocity and longitudinal stress in RDX at the two impact velocities were in reasonable agreement with experimental data in the literature. However, the present work did not predict the observed two wave fronts at 876 m/s due to the absence of inelasticity in the inter-particle potential force used. For the same reason, the temperature calculation under shock loading performed by assuming dissipation of 90% of the potential energy needs to be treated as a model calculation. While the DPDE method has been successfully extended in the current work to simulate mesoscale response of HE materials at micron and sub-micron length scales for the first time, it needs to be further extended by incorporating a contact algorithm to model impactor-target interaction, a more refined inter-particle potential force and incorporating anisotropy in the simulation.

CHAPTER 1

INTRODUCTION

1.1 Introduction

The ability to simulate the response of materials under different loading conditions yields predictive capabilities and helps narrow down the search space in which targeted experiments need to be done thereby saving both cost and effort. In addition, the computational modeling of materials can be easily taken up in a laboratory even for those experimental conditions which may be very difficult or even impossible to achieve in experiment. This allows the materials' response to be explored under unique loading conditions along with the simulation of specific experimental conditions which helps advance the understanding of materials. For example, it may be very difficult experimentally to obtain a single, isolated molecule of material for study but simulations of such isolated molecules are done routinely. Different methodologies exist for modeling the material behavior at different length and time scales. These methodologies can be broadly classified as continuum methods as exemplified by the Finite Element Methods (FEM)[1] and particle methods as exemplified by molecular dynamics (MD)[2]. There are many other particle methods that operate between FEM and MD, for example, smooth particle hydrodynamics (SPH)[3], discrete element method[4] (DEM), particle-in-cell method[5], particle kernel methods[6] etc. Figure 1 shows the different spatial and temporal regimes in which different simulation methodologies operate[7]

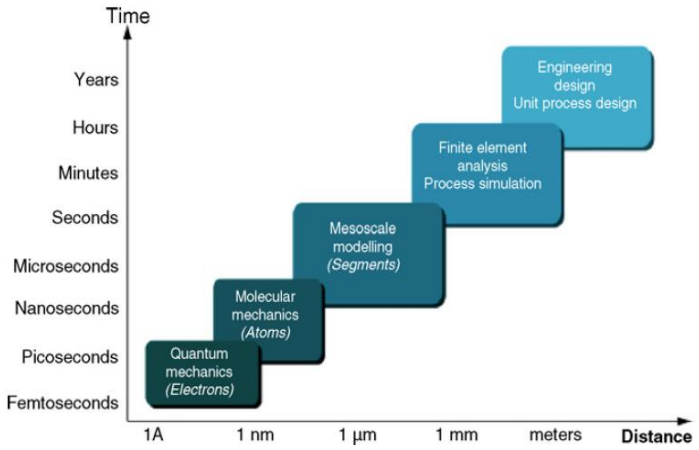

Figure 1 Spatial and temporal regimes for various simulation methodologies[7]

Originally developed based on continuum mechanics for analysis of aeroplane structures in 1960's and large scale structures, the FEM has become the primary method for modeling and simulation of the response of materials under different loading conditions. The spatial and temporal regimes are in the range of few microns and beyond and nano-seconds and beyond respectively. Similarly, the MD method has gained prominence in exploring materials' response in the spatial and temporal regime of nanometer (nm) and nanoseconds and below respectively employing particle interactions at atomic and molecular level. Both of these approaches have their advantages and limitations. The FEM method suffers from mesh distortion issues as the spatial length scale is reduced below few microns. MD in principle can be used to model mesoscale behavior. However, this requires the solution of equations of motion of billions or even trillions of atoms/molecules which is beyond the capabilities of most of the powerful computers of the day. MD simulations for a system of billions of atoms have been carried out in few select[8] studies but they are limited to large scale computational facilities.

However, particle methods by their very nature incorporate the discreteness of the material and are naturally well suited for modeling heterogeneities in the material. Within the spatial and temporal scales modeled by FEM and MD is the mesoscale regime which has gained increasing attention in the last two decades. Dissipative particle dynamics with energy conservation (DPDE) method[9], a recently introduced modeling technique, is a stochastic particle method that holds promise due to the inbuilt conservation of mass, momentum and energy. DPDE has been derived from thermodynamics and statistical mechanics principles. Developed originally as the isothermal dissipative particle dynamics (DPD) method[10] for simulating gases and extended to polymeric liquids at the molecular length scales, the incorporation of internal energy and meso temperature variables extended DPD to DPDE formulation allowing temperature and heat transport calculations without solving separate heat transport equations. The method has been successfully applied to coarse grained molecular scales for HE and to macromolecular scale for polymers. However, it is yet to be applied at the micron and sub-micron length scales of solids.

Existing particle methods have been extensively used for simulation of shock phenomenon[4, 11-15]. These include MD, DPDE and DEM. Extensive work has been done in MD for simulation of shock propagation in materials. Holian et al.[11] introduced the momentum mirror technique in MD for shock wave simulations. In the momentum mirror technique, an imaginary momentum reflecting mirror is placed at the piston end of material subjected to shock. The position of the mirror is augmented by piston velocity every time step. All particles that go beyond the piston outside of the simulation cell are reflected back into the simulation cell across the mirror plane and with their velocities

reversed. Kadau et al.[12] performed multimillion atom MD simulation to study phase transformation in solid iron. The simulated U_s-U_p equation of state and the P-V Hugoniot agreed well with the experiment. At high shock strengths, a phase transition from bcc to hcp iron was obtained and the orientational relationship between the hcp and the bcc region was the same as observed in the martensitic transformation of bcc iron. Farrow et al.[14] used non equilibrium MD simulations to study shock propagation in quartz using the momentum mirror technique. The computed Hugoniot was in good agreement with experimental data upto 25 GPa. A modified form of the simple BKS potential[16] was used to model interparticle interactions in their work on quartz.

DPDE and its variants have also been used to model shock response of lipids and polymeric materials. Ganzenmuller et al.[13] used DPDE to simulate shock wave propagation in lipid bilayers. A damage parameter was introduced into the simulation to study the damage behavior of the lipid. Each lipid was modeled as a mesoscopic chain with hydrophilic head and two hydrophobic tail beads. The water molecule was modeled by coarse graining four water molecules to one mesoscopic water bead. The interactions between them were modeled by Week-Chandler-Andersen potential[17, 18]. The pressure profiles at different times were obtained and their effect on the damage parameter was studied. However, their work deals with soft polymeric materials only and coarse graining is limited to agglomeration of few molecules and therefore does not go to a micron or submicron scale regime. Stoltz[19] used a mesoscopic modeling technique very similar to DPDE to model shock propagation inside a 2D slab of polymeric material. The inter particle interactions in the material were modeled by a form of Rydberg potential[20]. The parameters of the potential were obtained by requiring that the potential function

correctly reproduces the stress in uniaxial compression. Unlike DPDE, Stoltz[19] used a scheme in which the dissipative and random forces are not projected along the line connecting the two particles. The integration scheme used was a variant of the Shardlow splitting scheme[21] in which the stochastic and deterministic forces were integrated separately. Internal energy changes due to mesoscopic conduction were neglected and the evolution of internal energy was entirely due to dissipative forces in the system. Stoltz's[19] simulation results for the temporal evolution of temperature in the material as a result of shock propagation in it were in good agreement with the all atom simulation results. However, in this work, only the 2D case was simulated and for a polymeric material. The meso-particles were point particles and not micron and sub-micron sized meso- particles. In this work, it was assumed that the material is inert and no reaction accompanied the passage of shock through the material. Extending this work to the reactive case, Maillet et al.[22] modeled the passage of shock through a material wherein the shock triggered an exothermic reaction. To this end, each mesoparticle was assigned a progress variable that tracked the progress of the chemical reaction for that meso-particle. The evolution of position and momentum are similar to the inert case. The progress variable tracked the extent of reaction for the mesoparticle. The evolution of internal energy is based on the dissipative interactions as in the inert case and also the exothermicity associated with the reaction. In this work, the meso-particles were point sized particles arranged in random fashion in a RVE, something that cannot be used to model a crystalline, anisotropic high explosive (HE) material. Maillet et al.[23] also used DPDE to simulate the detonation of high explosive liquid with thermodynamic properties similar to nitromethane. To each mesoparticle was assigned a reaction progress variable that tracked the progress of the

reaction for that particle and the decomposition of the liquid was modeled by a first order kinetics. Moore et al.[24] studied the effect of various parameters of the DPDE formulation on the shock response of RDX and compared their results with all atomistic simulations. They also obtained temperature profiles in RDX for various values of the amplitude of the dissipative force, γ, and specific heat, C_v. The temperature profiles were qualitatively similar demonstrating the robustness of their approach but differed from the all atomistic profiles. The meso-particles in the work of Moore et al.[24] were obtained by coarse graining from RDX molecules and several molecules were coarse grained into a meso-particle. This level of coarse graining is several orders of magnitude lower than a micron or submicron regime, the true mesoscale regime, which is the focus of this work.

While MD, DPDE and variants of DPDE have been used to model shock response in materials, it is clear that these studies have been limited to soft polymeric materials, liquids and lipids. In these works, the particles were either point particles or when the system was coarse grained, the coarse graining was limited to at best macromolecular level. None of these works have explored DPDE for modeling phenomenon in solids at micron and submicron length scales, the true mesoscale regime.

DEM is another particle method that has been used to model shock response at mesoscale. Yano et al.[4] used DEM for modeling the shock response of copper. The DEM method utilizes particles with the diameter in micron range as elements to simulate grains with average diameter of several tens of microns. Depending on the distance of separation of the particles and their history, two particles can have different states of interaction. Each different state of interaction is associated with a different set of inter-particle forces. In this method, the chemical interaction between the particles is modeled

by the Lennard-Jones form of potential[4]. A flyer plate impacting a stationary target was simulated and the simulation results were compared with the results of Mescheryakov's experiment[25]. Yano et al.[15] also used 2D DEM to simulate alpha to epsilon transition in iron. Simulation results were presented for quasi-static as well as shock loading conditions. The grains were composed of circular disk shaped elements and the inter-particle forces between these elements were dependent on their link status. Each element was assigned a phase identification variable which changed value when the element satisfied a certain criterion. This criterion may be the temperature and/or pressure of the element. This phase identification variable was used to model phase change. However, despite using inter-particle potential, the DEM methodology is primarily based on continuum mechanics and phenomenologies and requires separate heat conduction solution.

Shock propagation in high explosive (HE) materials has been studied experimentally as well. Hooks[26] et al. experimentally studied shock propagation in single crystal RDX at a pressure of 2.25 GPa. They obtained VISAR particle velocity histories for impact experiments on (210), (111) and (100) RDX planes using LiF as a window material. From their shock wave experiments, they obtained U_s-U_p relationship for the equation of state of RDX for shock propagation in different crystallographic directions of RDX.

The modeling of the shock response of HE materials is challenging because of the generation of new chemical species accompanied by phase evolution on one hand and mechanical failure on the other. The shock response of HE materials leading to detonation has a transitory stage in which a solid phase undergoing deformation and

failure at mesoscale, a decomposed state due to solid sublimation and a gas phase coexist. The system is heterogeneous not only in terms of different phases but even within a single solid phase, because of failure, mechanical heterogeneities exist. The reactions within the transitory stage contribute also to energy release and heating of the reaction mix as new chemical species are generated as products. This presents a complex problem in which different length scales and phases coexist along with energy exchange between them. Finite element method has been used for inhomogeneous mesoscale simulations[27] of solids while fluid dynamics methods have been used to study detonation in detonation shock dynamics field (DSD)[28]. To the best of our knowledge, no computational tool exists to model and simulate the coupled response of the heterogeneous transitory state with mixture of phases and length scales. The DPDE method is envisioned to be an amenable particle method for such simulations. Originally developed at the molecular length scales, DPDE can model heterogeneities such as solid failures (fracture and voids) by dissociating particles from its neighbors, different phases by transitioning to different set of inter-particle potentials, etc. provided the method can be extended to submicron and micron length scales. The focus of the present work is to explore if DPDE can be extended and applied at the sub-micron and micron mesoscale length scales for solids preserving its core advantages. It is envisioned that if DPDE can be extended and applied to simulate phenomenon at the micron length scale, a unified simulation framework that transitions seamlessly across different length scales accounting for heterogeneities may be feasible.

1.2 Literature Survey

Dissipative Particle Dynamics[10] (DPD) augmented with energy conservation[9, 29, 30] (DPDE) are new methodologies envisioned to be applicable at wide range of length scales. DPDE is based on adding energy conservation to DPD and, other than the energy aspects, retains the basic structure of DPD as its core. The built-in conservation of energy is a desirable aspect of the DPDE method that serves to make it a potential tool for simulation of shock propagation in materials.

1.2.1 Dissipative Particle Dynamics (DPD)

The original motivation behind DPD was to combine the best features of MD[2] and Lattice Gas Automata (LGA)[31] or Lattice Gas Cellular Automata (LGCA)[32], two methods that were available for simulating complex material behavior before the formulation of DPD[10]. MD is a physically sound methodology that has Galilean invariance and isotropy intrinsically built into it. LGA allows an incremental time step several orders of magnitude higher than MD and is computationally efficient[10]. However, in LGA particles are required to move on a regular lattice and LGA does not have Galilean invariance and isotropy built into it which is a major drawback[10]. Frisch et al.[31] showed that LGA can be extended to incorporate these fundamental principles for the case of single phase flows. However, for complex fluid systems and multiphase fluids, the number of possible states for each lattice site increase significantly thereby making the LGA model cumbersome and difficult to extend[10]. A methodology that would combine the rigor and extensibility of MD with the time step of LGA would be very desirable.

DPD, the basis of DPDE, was introduced by Hoogerbrugge and Koelman[10] to simulate the hydrodynamic behavior of polymeric fluids in a computationally efficient

manner. In their original model, Hoogerbrugge and Koelman[10] consider the equations of motion of N particles moving in a simulation cell of volume V . The specification of the positions and the velocities of N particles constituting the system at every time step completely specifies the system. The system is updated in discrete time steps in two phases: a collision phase and a propagation phase. In the collision phase, the momenta of the particles are updated as[10]

$$^{t+\Delta t}\mathbf{p}_i = {}^{t}\mathbf{p}_i + \sum_j \Omega_{ij}\, {}^{t}\mathbf{n}_{ij} \tag{1}$$

Here, $^{t+\Delta t}\mathbf{p}_i$ is the momentum of particle ‘i' after the collision and $^{t}\mathbf{p}_i$ is the momentum of particle ‘i' before the collision. Δt is the time step and $^{t}\mathbf{n}_{ij}$ is a unit vector from particle ‘j’ to particle ‘i'. Ω_{ij} is the momentum transferred from particle ‘j’ to particle ‘i'. Following the collision phase is the propagation phase, in which the positions of particles are updated as[10]

$$^{t+\Delta t}\mathbf{r}_i = {}^{t}\mathbf{r}_i + \frac{\Delta t}{m_i}\, {}^{t+\Delta t}\mathbf{p}_i \tag{2}$$

Here, $^{t+\Delta t}\mathbf{r}_i$ is the updated position vector and $^{t}\mathbf{r}_i$ is the position vector of the particle ‘i' at the beginning of time increment Δt and m_i is mass of the particle. The momentum transferred between the particles Ω_{ij} is given as[10]

$$\Omega_{ij} = W\left(\left|{}^{t}\mathbf{r}_i - {}^{t}\mathbf{r}_j\right|\right)\left\{\Pi_{ij} - \omega\left({}^{t}\mathbf{p}_i - {}^{t}\mathbf{p}_j\right)\cdot {}^{t}\mathbf{n}_{ij}\right\} \tag{3}$$

Here, ω is a positive number and $W\left(\left|{}^{t}\mathbf{r}_i - {}^{t}\mathbf{r}_j\right|\right)$ is a dimensionless non negative weight function that vanishes beyond a specified cutoff distance. $W\left(\left|{}^{t}\mathbf{r}_i - {}^{t}\mathbf{r}_j\right|\right)$ is normalized so

that its integral over all space is the inverse of average particle density. Π_{ij} [10] is a random number sampled from the distribution with mean $\langle \Pi_{ij} \rangle = \Pi_0$ and variance $\left\langle \left(\Pi_{ij} - \Pi_0 \right)^2 \right\rangle = \delta\Pi^2$. Further, $\Pi_{ij} = \Pi_{ji}$ for every pair of particles (i,j).

The combination of stochastic inter-particle forces introduced in the DPD formulation distinguishes DPD from coarse grained MD. This aspect retains the basic advantageous features of MD; the formulation is built on inter-particle forces which allows it to be easily extensible. However, the combination of stochastic forces compensates in an average manner for the degrees of freedom lost by coarse graining in coarse grained MD. The first stochastic term in equation (3) is the random term and tends to heat the system. The second term in equation (3) tends to oppose relative motion between the two particles thereby dissipating energy from the system. The two terms tend to maintain the system at a constant temperature and act as a thermostat. Koelman and Hoogerbrugge[33] showed that an adequate quantitative description of the isothermal fluid flow is obtained with this simple formulation using a fraction of particles compared to MD.

Hoogerbrugge and Koelman[10] tested and validated their formulation by applying DPD to simulate fluid flow under periodic boundary conditions in a two-dimensional geometry. Using DPD, they obtained the pressure and velocity distribution of the particles and the dependence of drag coefficient on particle radius for low Reynold's number in good agreement with the theory[10]. To further validate their novel methodology, Koelman and Hoogerbrugge[33] also used DPD to study hard sphere suspensions under steady shear. They observed good agreement between their DPD simulations for concentrated suspensions at high Peclet[33] number and the experimental

results. These simulations were limited to isothermal conditions. This showed DPD to be a promising particle simulation technique for simulating fluid phenomenon under isothermal conditions. However, the fluid particles had no spatial extent and so the applicability of DPD to simulate finite sized particles as well as solid materials remained unexplored. Besides, their original formulation did not have the framework to simulate non-isothermal situations.

However, the success of DPD in combining the extensibility and rigor of MD with the larger incremental time step of LGA and at the same time using a fraction of particles needed for MD did not go unnoticed. Since then, DPD has been applied extensively to model fluid flow using point sized particles. Extensive literature exits on the application of DPD to model soft materials and polymeric melts[34-39].

Boek et al.[34] applied DPD to study the rheology of dilute and concentrated (upto 40%) suspensions of spheres, rods and disks. They computed reduced viscosity as a function of the solid concentration in the suspension and obtained good agreement with the experiment. The cubic scaling behavior obtained for rods and disks and the computed intrinsic viscosity of dilute suspensions of rods and disks was in excellent agreement with theoretical predictions. Liu et al.[35] used DPD to simulate contact angles and wetting behavior of fluids for multiphase flow inside a capillary and cross fracture junction. They simulated three different wetting regimes: Total wetting, moderate wetting and non-wetting by changing the interaction parameters for the fluid-fluid and fluid-solid interaction. Their DPD simulation results compared favorably to those obtained from SPH, thereby, validating the DPD methodology. Martys[36] used DPD to simulate the flow of suspensions under different test conditions and compared the results with theoretical

predictions. Both Couette and Poiseuille flow were simulated. DPD reproduced the velocity profiles of these standard test cases. DPD was also able to account for the theoretical results on the intrinsic viscosity of dilute suspensions as predicted by Einstein's theory. The simulations for concentrated suspensions were compared with experimentally obtained results and those from the Stokesian dynamics method and excellent agreement was observed. This demonstrated the strength of DPD methodology.

Ripoll and Ernst[37] investigated a random DPD solid using both analytical and simulation techniques. The motivation for this work was that the Lorentz gas contains only the mechanism of kinetic transport by which energy and momentum can be transported. On the other hand, a random DPD solid contains only the mechanism of collisional transport for exchange of energy and momentum. A random DPD solid provides an idealized system in which the transport properties can be exactly evaluated in the high density limit[37]. Diffusivities as a function of density for two and three dimensional systems were studied and related to the parameters of the model in the high density limit. The decay of a perturbation in the fluid was examined to validate the model against hydrodynamic predictions. Willemsen et al.[38] applied DPD to study the flow of polymer in the square capillary which is an idealization for the hydrodynamic chromatography technique. The results for the simulation of axial velocity profile in the capillary agreed very well with the experiment. Willemsen et al.[38] also used DPD to simulate the melting of polymer in a shear flow. The velocity and temperature profile were obtained for the melting of a particle placed between two moving plates.

Ball and Melrose[40] presented a simulation technique, very similar to DPD, to study the quasi static motion of particles under the influence of pairwise conservative and

dissipative forces. They observed that for quasi static motion of powders, Brownian motion could be neglected but where fluctuations played an important role, random forces must be taken into account. They discussed the choice of time step for the algorithm and the imposition of boundary conditions for their scheme. Some numerical simulation results which were in qualitative agreement with the experiment were presented for the rheology of concentrated suspension of spheres under shear flow. They also motivated a connection between their simulation technique and DPD in the diffusive limit. However, their work, like the previous ones modeled a suspension and not a solid.

Espanol[41] presented a generalization of DPD that included shear forces between particles. The shear force was assumed to be proportional to the relative velocity of particles. Angular momentum conservation was taken into account by attaching an angular momentum variable to each meso-particle. An increase or decrease in the angular momentum of the meso-particle was reflected in the change in the spin variable attached to the meso-particle. By imposing the condition that the equilibrium distribution be the Gibb's canonical ensemble, correct thermodynamic behavior was obtained. It was observed that this new generalized version of DPD has the same structure as that of SPH. Their work demonstrated the easy extensibility of DPD without disrupting the core formulation of the methodology.

All the above mentioned applications of DPD had served to validate the core idea of DPD; the incorporation of stochastic forces in the formulation in addition to the deterministic forces. They had conclusively demonstrated the utility of incorporating stochastic forces in the formulation. Besides, they had spawned a lot of interest in the

DPD methodology and in overcoming its main drawback, i.e. its limitation to model isothermal phenomenon only.

However, all of the above successes of DPD were limited to soft, polymeric fluids and little was said about its applicability to solids. The DPD particles were either point particles or agglomerates of DPD point particles constrained to move as a unit. The application of DPD to solids and at mesoscale regime remained unexplored.

In the original formulation of DPD, the dissipative and random forces were independent of one another. Mesoscale particle methodologies such as DEM[4] exist and they also incorporate stochastic forces in their formulation. However, in DEM[4] the stochastic forces are independent and are not based on statistical mechanics arguments. Such a theoretical basis is needed for the rigorous theoretical development of any new methodology. Espanol and Warren[42] provided a firm statistical mechanics basis for DPD by formulating a fluctuation-dissipation theorem for the stochastic forces in the DPD formulation. They obtained the coupled stochastic differential equations (SDE) for DPD and then derived the Fokker-Planck equation corresponding to this set of stochastic differential equations[42].

The stochastic differential equations describe the update for the position and momenta of the particles[42]. The update of the position and momenta are respectively given by[42]

$$d\,{}^{t}\mathbf{r}_i = \frac{{}^{t}\mathbf{p}_i}{m_i}\Delta t \tag{4}$$

$$d\,{}^{t}\mathbf{p}_i = \left[\sum_{j\neq i}\mathbf{F}_{ij}^{c}\left({}^{t}r_{ij}\right) + \sum_{j\neq i} -\gamma_{ij}\omega^{D}\left({}^{t}r_{ij}\right)\left({}^{t}\mathbf{n}_{ij}\cdot{}^{t}\mathbf{v}_{ij}\right){}^{t}\mathbf{n}_{ij}\right]\Delta t + \sum_{j\neq i}\sigma_{ij}\omega^{R}\left({}^{t}r_{ij}\right){}^{t}\mathbf{n}_{ij}dW_{ij} \tag{5}$$

Here, $\mathbf{F}_{ij}^{C}\left({}^{t}r_{ij}\right)$ is the conservative force acting between the pair of particles 'i' and 'j' that depends only on the distance, ${}^{t}r_{ij}=r,$ between the particles 'i' and 'j'. $\gamma_{ij}=\gamma$ and ω^{D} are respectively the amplitude and weight functions of the dissipative force. $\sigma_{ij}=\sigma$ and ω^{R} are respectively the amplitude and weight function of the random force. The weight functions ω^{D} and ω^{R} are functions of the inter-particle separation ${}^{t}r_{ij}$ between the particles 'i' and 'j'. ${}^{t}\mathbf{v}_{ij}={}^{t}\mathbf{v}_{i}-{}^{t}\mathbf{v}_{j}$ where ${}^{t}\mathbf{v}_{i}$ and ${}^{t}\mathbf{v}_{j}$ are respectively the velocities of particle 'i' and 'j' at time t. $dW_{ij}=dW_{ji}$ are independent increments of the Wiener process. Espanol and Warren[42] then derived the Fokker-Planck equation for the time evolution of the probability distribution $\rho_{p}({}^{t}\mathbf{r}_{i},{}^{t}\mathbf{p}_{i};t)$ corresponding to the above stochastic differential equation (SDE). The Fokker Planck equation is given by[42]

$$\partial_{t}\rho_{p}\left({}^{t}\mathbf{r}_{i},{}^{t}\mathbf{p}_{i};t\right)=L_{C}\rho_{p}\left({}^{t}\mathbf{r}_{i},{}^{t}\mathbf{p}_{i};t\right)+L_{D}\rho_{p}\left({}^{t}\mathbf{r}_{i},{}^{t}\mathbf{p}_{i};t\right) \tag{6}$$

where the operators L_{C} and L_{D} are defined as[42]

$$L_{C}\rho_{p}\left({}^{t}\mathbf{r}_{i},{}^{t}\mathbf{p}_{i};t\right)\equiv-\left[\sum_{i}\frac{{}^{t}\mathbf{p}_{i}}{m_{i}}\frac{\partial}{\partial{}^{t}\mathbf{r}_{i}}+\sum_{i,j\neq i}\mathbf{F}_{ij}^{c}\frac{\partial}{\partial{}^{t}\mathbf{p}_{i}}\right]\rho_{p}\left({}^{t}\mathbf{r}_{i},{}^{t}\mathbf{p}_{i};t\right) \tag{7}$$

$$\begin{aligned}L_{D}\rho_{p}\left({}^{t}\mathbf{r}_{i},{}^{t}\mathbf{p}_{i};t\right)\equiv&\sum_{i,j\neq i}{}^{t}\mathbf{n}_{ij}\frac{\partial}{\partial{}^{t}\mathbf{p}_{i}}\left[\gamma_{ij}\omega^{D}\left({}^{t}r_{ij}\right)\left({}^{t}\mathbf{n}_{ij}\cdot{}^{t}\mathbf{v}_{ij}\right)\right]\rho_{p}\left({}^{t}\mathbf{r}_{i},{}^{t}\mathbf{p}_{i};t\right)+\\&\sum_{i,j\neq i}{}^{t}\mathbf{n}_{ij}\frac{\partial}{\partial{}^{t}\mathbf{p}_{i}}\left[\frac{\sigma_{ij}{}^{2}}{2}\left(\omega^{R}\right)^{2}\left({}^{t}r_{ij}\right){}^{t}\mathbf{n}_{ij}\left(\frac{\partial}{\partial{}^{t}\mathbf{p}_{i}}-\frac{\partial}{\partial{}^{t}\mathbf{p}_{j}}\right)\right]\rho_{p}\left({}^{t}\mathbf{r}_{i},{}^{t}\mathbf{p}_{i};t\right)\end{aligned} \tag{8}$$

The operator L_C is the Liouville operator and takes into account the effect of conservative force. The operator L_D takes into account the effect of dissipative and random forces and contains second order derivatives. At equilibrium, the probability distribution is stationary and does not evolve in time. This implies that at equilibrium

$$\partial_t \rho_p = 0 \tag{9}$$

The equilibrium Gibbs canonical distribution is given by

$$\rho_p{}^{eq}\left({}^t\mathbf{r}_i, {}^t\mathbf{p}_i\right) = \frac{1}{Z}\exp\left[-H\left({}^t\mathbf{r}_i, {}^t\mathbf{p}_i\right)\Big/k_B T\right] = \frac{1}{Z}\exp\left[-\left(\sum_i \frac{{}^t\mathbf{p}_i \cdot {}^t\mathbf{p}_i}{2m_i} + V\left(\left|{}^t\mathbf{r}_{ij}\right|\right)\right)\Big/k_B T\right] \tag{10}$$

Here, H is the Hamiltonian of the system, and $V\left(\left|{}^t\mathbf{r}_{ij}\right|\right)$ is the potential function from which the conservative force is derived, k_B is the Boltzmann constant, T is the equilibrium temperature and Z is the normalizing partition function of the ensemble.

Operator L_c in equation (7) when operating upon the equilibrium probability density, ρ_p^{eq}, in equation (10) gives

$$\left[\sum_i \frac{{}^t\mathbf{p}_i}{m_i}\frac{\partial}{\partial {}^t\mathbf{r}_i} + \sum_{i,j\neq i}\mathbf{F}_{ij}^c \frac{\partial}{\partial {}^t\mathbf{p}_i}\right]\rho_p^{eq} = \sum_i \frac{{}^t\mathbf{p}_i}{m_i}\frac{\partial\left(\rho_p^{eq}\right)}{\partial {}^t\mathbf{r}_i} + \sum_{i,j\neq i}\mathbf{F}_{ij}^c \frac{\partial\left(\rho_p^{eq}\right)}{\partial {}^t\mathbf{p}_i} \tag{11}$$

The first term on the RHS of equation (11) gives

$$\left(\frac{{}^t\mathbf{p}_i}{m_i}\frac{\partial}{\partial {}^t\mathbf{r}_i} + \frac{{}^t\mathbf{p}_j}{m_j}\frac{\partial}{\partial {}^t\mathbf{r}_j}\right)\rho_p^{eq} = \mathbf{F}_{ij}^C\left(\frac{1}{k_B T}\right)\left(\frac{{}^t\mathbf{p}_i}{m_i}\right)\rho_p^{eq} + \mathbf{F}_{ji}^C\left(\frac{1}{k_B T}\right)\left(\frac{{}^t\mathbf{p}_j}{m_j}\right)\rho_p^{eq} \tag{12}$$

since the conservative force is derivable from the potential. The second term on the RHS in equation (11) gives

$$\sum_{i,j\neq i}\mathbf{F}_{ij}^{c}\frac{\partial}{\partial {}^{t}\mathbf{p}_{i}}\left(\rho_{p}^{eq}\right)=\left(\mathbf{F}_{ij}^{c}\frac{\partial}{\partial {}^{t}\mathbf{p}_{i}}+\mathbf{F}_{ji}^{c}\frac{\partial}{\partial {}^{t}\mathbf{p}_{j}}\right)\left(\rho_{p}^{eq}\right) \tag{13}$$

The derivatives of ρ_{p}^{eq} w.r.t. momenta are

$$\begin{aligned}\frac{\partial}{\partial {}^{t}\mathbf{p}_{i}}\left(\rho_{p}^{eq}\right)&=\rho_{p}^{eq}\left(-\frac{1}{k_{B}T}\right)\left(\frac{{}^{t}\mathbf{p}_{i}}{m_{i}}\right)\\ \frac{\partial}{\partial {}^{t}\mathbf{p}_{j}}\left(\rho_{p}^{eq}\right)&=\rho_{p}^{eq}\left(-\frac{1}{k_{B}T}\right)\left(\frac{{}^{t}\mathbf{p}_{j}}{m_{j}}\right)\end{aligned} \tag{14}$$

Substituting equation (14) in equation (13) gives

$$\mathbf{F}_{ij}^{C}\left(-\frac{1}{k_{B}T}\right)\left(\frac{{}^{t}\mathbf{p}_{i}}{m_{i}}\right)\rho_{p}^{eq}+\mathbf{F}_{ji}^{C}\left(-\frac{1}{k_{B}T}\right)\left(\frac{{}^{t}\mathbf{p}_{j}}{m_{j}}\right)\rho_{p}^{eq} \tag{15}$$

The sum of terms in equation (12) and equation (15) cancels to zero. Consequently,

$$L_{C}\rho_{p}^{eq}=0 \tag{16}$$

The operation of operator L_{D} in equation (8) on ρ_{p}^{eq} in equation (10) gives

$$L_{D}\rho_{p}^{eq}\equiv\sum_{i,j\neq i}{}^{t}\mathbf{n}_{ij}\frac{\partial}{\partial {}^{t}\mathbf{p}_{i}}\left[\begin{array}{l}\gamma_{ij}\omega^{D}\left({}^{t}r_{ij}\right)\left({}^{t}\mathbf{n}_{ij}\cdot{}^{t}\mathbf{v}_{ij}\right)+\\ \frac{\sigma_{ij}{}^{2}}{2}\left(\omega^{R}\right)^{2}\left({}^{t}r_{ij}\right){}^{t}\mathbf{n}_{ij}\left(\frac{\partial}{\partial {}^{t}\mathbf{p}_{i}}-\frac{\partial}{\partial {}^{t}\mathbf{p}_{j}}\right)\end{array}\right]\rho_{p}^{eq} \tag{17}$$

Using equation (14), the cross term containing double derivatives in equation (17) can be written as

$$\begin{aligned}&\sum_{i,j\neq i}{}^{t}\mathbf{n}_{ij}\frac{\partial}{\partial {}^{t}\mathbf{p}_{i}}\left[\frac{\sigma_{ij}{}^{2}}{2}\left(\omega^{R}\right)^{2}\left({}^{t}r_{ij}\right){}^{t}\mathbf{n}_{ij}\left(\frac{\partial}{\partial {}^{t}\mathbf{p}_{i}}-\frac{\partial}{\partial {}^{t}\mathbf{p}_{j}}\right)\right]\rho_{p}^{eq}=\\ &\sum_{i,j\neq i}{}^{t}\mathbf{n}_{ij}\frac{\partial}{\partial {}^{t}\mathbf{p}_{i}}\left[\frac{\sigma_{ij}{}^{2}}{2}\left(\omega^{R}\right)^{2}\left({}^{t}r_{ij}\right)\left({}^{t}\mathbf{n}_{ij}\cdot{}^{t}\mathbf{v}_{ij}\right)\left(-\frac{1}{k_{B}T}\right)\right]\rho_{p}^{eq}\end{aligned} \tag{18}$$

Substituting equation (18) in equation (17), we obtain

$$L_D\rho_p^{eq} = \sum_{i,j\neq i} {}^t\mathbf{n}_{ij} \frac{\partial}{\partial {}^t\mathbf{p}_i}\left[\gamma_{ij}\omega^D\left({}^t r_{ij}\right)\left({}^t\mathbf{n}_{ij}\cdot{}^t\mathbf{v}_{ij}\right)\right]\rho_p^{eq} + \sum_{i,j\neq i} {}^t\mathbf{n}_{ij} \frac{\partial}{\partial {}^t\mathbf{p}_i}\left[\frac{{\sigma_{ij}}^2}{2}\left(\omega^R\right)^2\left({}^t r_{ij}\right)\left({}^t\mathbf{n}_{ij}\cdot{}^t\mathbf{v}_{ij}\right)\left(-\frac{1}{k_BT}\right)\right]\rho_p^{eq} \tag{19}$$

The only way $L_D\rho_p^{eq}$ can be zero at *all* times is if

$$\omega^D = \left(\omega^R\right)^2 \tag{20}$$

$$\sigma_{ij} = \left(2k_BT\gamma_{ij}\right)^{1/2} \tag{21}$$

Equations (20) and equation (21) were first obtained by Espanol and Warren[42]. This is the statement of the fluctuation dissipation theorem[42] for the DPD system. With these conditions imposed, Espanol and Warren[42] found that the algorithm is stable only if the time step is sufficiently small

The theoretical machinery of DPD methodology was further developed by Marsh et al.[43] who obtained the Fokker-Planck equation for the DPD fluid and related the Navier-Stokes equation governing the hydrodynamic behaviour of the fluid to it. The equation is then solved by the kinetic theory technique of Chapman-Enskog (see for example Reinecke and Kremer[44]) method. Thermodynamic and transport properties of the DPD fluid are expressed in terms of the parameters of the DPD simulation. They also present macroscopic flow equation for momentum and energy for the DPD fluid. Essentially, in their work, the DPD method is motivated as a technique for simulating the transport properties of fluids and suspensions. Marsh and Coveney[45] formulated the H theorem for the multicomponent isothermal DPD system. H theorem is essentially a statement of second law of thermodynamics which says that during an irreversible process, the entropy of the system cannot decrease or the related quantity H cannot

increase. They formulated the H functional for DPD and showed that at equilibrium, the H functional attained its stationary value and the equilibrium statistical distribution is obtained.

The development of fluctuation-dissipation theorem and H theorem for DPD was a critical step in its establishment as a physically sound and theoretically rigorous methodology. The statistical mechanics basis meant that the entire machinery of statistical mechanics can be used to develop and get insight into the working of this recently introduced method. This was also an important step in the incorporation of energy conservation to DPD to yield DPDE and thereby overcoming its major limitation; to be applicable only to isothermal cases.

Groot and Warren[46] critically reviewed DPD as a simulation technique for atomistic and sub-mesoscopic regimes for polymeric fluids composed of point particles. The conservative force in their work was a soft repulsive force whose form is given by

$$\begin{aligned} \mathbf{F}_{ij}^{C} &= a_{ij}\left(1-{}^{t}r_{ij}\right){}^{t}\mathbf{n}_{ij} \quad \text{if } \left({}^{t}r_{ij}<1\right) \\ &= 0 \qquad\qquad\quad \text{if } \left({}^{t}r_{ij}\geq 1\right) \end{aligned} \tag{22}$$

Here, a_{ij}, is a repulsion parameter which is determined by matching some property of the system which in the case of liquids can be compressibility. The weight functions for the dissipative and random force are functions only of the distance ${}^{t}r_{ij}$ between the particles and are given as

$$\begin{aligned} \omega^{D}\left({}^{t}r_{ij}\right) = \left[\omega^{R}\left({}^{t}r_{ij}\right)\right]^{2} &= \left(1-{}^{t}r_{ij}\right)^{2} \quad \text{for } \left({}^{t}r_{ij}<1\right) \\ &= 0 \qquad\qquad\quad \text{for } \left({}^{t}r_{ij}\geq 1\right) \end{aligned} \tag{23}$$

Starting from the relationship between dissipative and random forces as established by Espanol and Warren[42], Groot and Warren[46] established the convergence ranges of the parameters for the dissipative and random interactions. Rather than using the Euler algorithm, Groot and Warren[46] also introduced the modified velocity-Verlet for integration of equations of motion of the DPD fluid. In this algorithm the velocity is updated in two steps but the force is computed just once. This algorithm reduces to the standard velocity-Verlet in the limit that the forces are independent of velocity. Groot and Warren[46] demonstrated that the scheme is stable only within a range of time step outside of which the simulation does not converge. The parameter a_{ij} of the conservative force is determined by the fluctuations of the liquid. The fluctuations in the liquid determine the thermodynamic state of the liquid and so if the thermodynamic behavior of the liquid is to be described correctly, the fluctuations in the liquid need to be correctly accounted for. The fluctuations in the liquid are determined by the compressibility of the liquid. Using the virial theorem, Groot and Warren[46] made the connection between the experimentally determined compressibility of the liquid and the repulsion parameter a_{ij} of the conservative force used to model chemical interactions between the particles. This relationship is given as

$$\kappa^{-1} = \frac{1}{k_B T}\left(\frac{\partial p}{\partial \rho_n}\right)_T \tag{24}$$

where κ^{-1} is a dimensionless compressibility whose value for a large class of polymeric liquids is experimentally known. $\left(\frac{\partial p}{\partial \rho_n}\right)$ is the derivative of virial pressure, p, w.r.t the

number density, ρ_n, of DPD particles in the system. The virial pressure p can be obtained from the virial theorem as

$$p = \rho_n k_B T + \frac{1}{3V}\left\langle \sum_{j>i} \left({}^{t}\mathbf{r}_i - {}^{t}\mathbf{r}_j \right) \cdot \mathbf{F}_{ij}^{C} \right\rangle \tag{25}$$

The subscript $j > i$ on the summation ensures that each pair is counted exactly once. This established a general approach for determining the unknown parameters of the conservative force in the DPD methodology. In general, experimental data on compressibility can be modeled using atomistic simulations. So Groot and Warren's[46] approach of determining the parameters of the conservative force used to describe mesoscopic behavior connects the mesoscopic DPD technique to experiments and atomistic simulations. Demonstrating this approach, Groot and Warren[46] derived a relationship between the parameters of the conservative force and the χ parameter of the Flory-Huggins model[47, 48]. Groot and Warren[46] carried out simulations for various values of particle number density and observed a parabolic relationship between the reduced pressure normalized by the repulsive force parameter when plotted as a function of number density. Using this parabolic behavior, Groot and Warren[46] established the equation of state of the DPD fluid for the first time. This equation of state of the DPD fluid has the form

$$p = \rho_n k_B T + \delta a \rho_n^{\,2} \qquad (\delta = 0.101 \pm 0.001) \tag{26}$$

where the pressure p of the DPD fluid has been related to the repulsive parameter of the conservative force a $(= a_{ij} = a_{ji})$. Groot and Warren[46] also modeled a physical system by simulating the surface tension between unlike polymers of equal length. Comparison of

DPD simulations with experimentally measured surface tension in the PS/PMMA system showed good agreement. Equations for viscosity and self-diffusion coefficient, the experimentally observed transport coefficients for polymeric fluids, were obtained in terms of the parameters of the DPD formulation. It was observed that the viscosity increases with the dissipation force parameter γ of equation (21) and the self-diffusion coefficient decreases with γ.

The work of Groot and Warren[46] was an important milestone in the development of DPD methodology since it presented a general approach for connecting DPD simulations to experimentally observed parameters. However, Groot and Warren's[46] work is based on modeling a fluid system composed of point sized DPD particles and not a crystalline solid. To model phenomenon at the submicron and micron scale using point particles would need an enormous number of particles defeating the very purpose of the mesoscale simulation technique. Besides, the conservative forces used to model interparticle interactions are of soft repulsive nature and do not go to infinity as the interparticle distance goes to zero. This is a serious limitation because in a true solid, the interparticle repulsion goes to infinity as the interparticle distance is reduced. Besides, this work does not consider dynamic loading of the RVE, something that is paramount for simulating shock propagation in solids. In DPD energy is not conserved. So without incorporating energy conservation, phenomenon such as shock propagation with conservation of mass, momentum and energy cannot be simulated.

Shardlow[21] presented an alternate integration scheme for integrating the equations of motion of DPD. In this integration scheme, the integration of the equations of motion is split into a stochastic component wherein the effects of stochastic forces, namely

dissipative and random, are taken into account and a deterministic component where the velocities are augmented by the conservative forces. Just like the integration scheme introduced by Groot and Warren[46], this scheme has been extensively used in DPD literature. Similar to the scheme by Groot and Warren[46], this scheme converges rapidly only within certain range of time step beyond which it is unstable.

1.2.2 Dissipative Particle Dynamics with Energy Conservation (DPDE)

DPD conserves mass and momentum but it does not conserve energy. DPD by itself is therefore an isothermal method. It cannot be used to model phenomenon where energy transfer explicitly needs to be taken into account. Mackie et al.[9], Avalos et al.[29] and independently of them Espanol[30] added energy conservation to the DPD formulation to yield DPDE. It is worthwhile to mention here that DPD and DPDE differ in that DPDE particles are characterized by two *additional* variables in addition to the standard variables for DPD particles. The ideas and theory that were originally developed for DPD carry over to DPDE with regard for these variables. The theoretical developments in DPD are therefore at the core of the DPDE methodology.

In DPDE, an internal energy reservoir is attached to each meso-particle. The measure of internal energy is the meso-temperature of the meso-particle. Consequently, in DPDE, in addition to the position momentum and force variable associated with each particle, each particle is assigned an internal energy variable and a meso temperature variable. Because each particle is individually assigned a meso temperature variable that is different from the overall temperature of the system, the energy exchange between meso-particles is not coupled to the average temperature of the system. So the DPDE

scheme, an extension of the DPD scheme can be used to model non isothermal processes such as heat conduction and shock.

The internal energy of the meso particle is related to the meso temperature of the particle by an equation of state. A simple equation of state that can adequately describes metal is of the form[49]

$$u_i = mC_v\theta_i \tag{27}$$

Here, u_i is the internal energy of the meso-particle 'i' with mass m_i, specific heat C_v and meso-temperature θ_i. Other equations of state can be readily incorporated in the formulation. In DPDE, it is assumed that the internal states of the particle are always in equilibrium with one another so that the only change in the state of the particle can come from its interaction with another particle. This allows the assignment of a mesoscopic entropy to each particle. As in standard thermodynamics, the change in internal energy and mesoscopic entropy for a particle are related by an equation of the form

$$\theta_i ds_i = du_i \tag{28}$$

Here, s_i is the mesoscopic entropy of the particle 'i'. The inter particle forces are assumed to be pairwise additive and conserve momentum as in DPD. In addition, when the change in internal energy variable attached to the particle is taken into account, energy is also conserved. The energy lost or gained by the meso-particle comes from the internal energy reservoir attached to the particle which causes a decrease or increase respectively in the mesoscopic temperature of the meso-particle.

In the standard formulation of DPDE, the change in internal energy of the DPDE meso particle can come from two sources: change due to mechanical interaction and

change due to mesoscopic heat conduction. Mackie et al.[9] and Avalos et al.[29] presented stochastic differential equations for the update of positions, momenta and internal energies of the DPDE meso particle. The equation for the update of positions is similar to DPD and is given by[9]

$$d\,{}^{t}\mathbf{r}_i = \frac{{}^{t}\mathbf{p}_i}{m_i}\Delta t \tag{29}$$

The equation for the update of momenta is given by[9]

$$\dot{\mathbf{p}}_i = \sum_{j\neq i}\left({}^{t}\mathbf{F}_{ij}^{P} + {}^{t}\mathbf{F}_{ij}^{D} + {}^{t}\mathbf{F}_{ij}^{R} + {}^{t}\mathbf{F}_{i}^{ext}\right) \tag{30}$$

Here, $\dot{\mathbf{p}}_i$ is the time rate of change of momentum of the particle. ${}^{t}\mathbf{F}_{ij}^{P}$, ${}^{t}\mathbf{F}_{ij}^{D}$, ${}^{t}\mathbf{F}_{ij}^{R}$, ${}^{t}\mathbf{F}_{i}^{ext}$ are respectively the conservative, dissipative, random and external force acting between the particles ‘i' and ‘j’. This is similar to the update of positions and velocities in DPD. In DPDE, in addition, there is a stochastic differential equation for the update of the internal energy variable u_i. This update of internal energy is given by[29]

$$\dot{u}_i = \frac{1}{2m_i}\left({}^{t}\mathbf{p}_j - {}^{t}\mathbf{p}_i\right)\cdot\left({}^{t}\mathbf{F}_{ij}^{D} + {}^{t}\mathbf{F}_{ij}^{R}\right) + \dot{q}_{ij}^{D} + \dot{q}_{ij}^{R} \tag{31}$$

Here, $\dot{q}_{ij}^{D}$ and $\dot{q}_{ij}^{R}$ are respectively the dissipative and random heat flows. The forms of the dissipative and random forces in the work of Avalos et al.[29] are given by

$$\begin{aligned} {}^{t}\mathbf{F}_{ij}^{D} &= \zeta(r)\frac{1}{m}\,{}^{t}\mathbf{r}_{ij}\,{}^{t}\mathbf{r}_{ij}\cdot({}^{t}\mathbf{p}_j - {}^{t}\mathbf{p}_i) \\ {}^{t}\mathbf{F}_{ij}^{R} &= {}^{t}\mathbf{r}_{ij}\Gamma_{ij}F_{ij}(t) \end{aligned} \tag{32}$$

$\zeta(r)$ and Γ_{ij} are respectively the products of amplitude and weight functions for the dissipative and random force. $F_{ij}(t)$ is a stationary, Gaussian and white noise. The dissipative and random heat flows are given as[29]

$$\begin{aligned} \dot{q}_{ij}^{D} &= \lambda_h(r)\left(\frac{1}{\theta_i}-\frac{1}{\theta_j}\right) \\ \dot{q}_{ij}^{R} &= sign(i-j)\Lambda_{ij}Q_{ij}(t) \end{aligned} \tag{33}$$

Here, $\lambda_h(r)$ is a positive coefficient, $sign(i-j)$ is a permutation function of 'i' and 'j' and is 1 if $i>j$ and -1 if $(i<j)$. The coefficient Λ_{ij} takes into account the effect of random forces on mesoscopic heat conduction. $Q_{ij}(t)$ is a stationary, Gaussian white noise that can be different from the Gaussian noise $F_{ij}(t)$ in equation (32). The $sign(i-j)$ function ensures that $\dot{q}_{ij}^{R}=-\dot{q}_{ji}^{R}$ thereby conserving energy.

Analogous to DPD[42], Mackie et al.[9], Avalos et al.[29] and independently Espanol[30] derived the statistical mechanics of DPDE. Based on the stochastic differential equations above for the update of position, momentum and internal energy of the particle, they independently obtained the Fokker-Planck equation and derived the statement of the fluctuation dissipation theorem for the DPDE system. Following Avalos et al.[29], the Fokker-Planck equation for the DPDE system can be written as[29]

$$\frac{\partial}{\partial t}\rho_p\left(\{{}^t\mathbf{r}_i\},\{{}^t\mathbf{p}_i\},\{u_i\}\right)=L^{con}\rho_p\left(\{{}^t\mathbf{r}_i\},\{{}^t\mathbf{p}_i\},\{u_i\}\right)+L^{dif}\rho_p\left(\{{}^t\mathbf{r}_i\},\{{}^t\mathbf{p}_i\},\{u_i\}\right) \tag{34}$$

where L^{con} and L^{dif} are the convective and diffusive operators and $\rho_p\left(\left\{{}^t\mathbf{r}_i\right\},\left\{{}^t\mathbf{p}_i\right\},\{u_i\}\right)$ is the probability density for the DPDE system analogous to ρ_p for the DPD system defined in equation (6). The form of L^{con} is given by[29]

$$L^{con} \equiv -\sum_{i=1}^{N}\left[\frac{\partial}{\partial {}^t\mathbf{r}_i}\cdot\frac{{}^t\mathbf{p}_i}{m_i}+\frac{\partial}{\partial {}^t\mathbf{p}_i}\cdot\mathbf{F}_i^{ext}\right]- \sum_{i,j\neq 1}^{N}\left\{\begin{array}{l}\dfrac{\partial}{\partial {}^t\mathbf{p}_i}\cdot\left[\mathbf{F}_{ij}^{C}+\zeta\left({}^t r_{ij}\right)\dfrac{1}{m_i}\,{}^t\mathbf{r}_{ij}\,{}^t\mathbf{r}_{ij}\cdot\left({}^t\mathbf{p}_j-{}^t\mathbf{p}_i\right)\right]+ \\ \dfrac{\partial}{\partial u_i}\left[\dfrac{1}{2m_i^{\,2}}\zeta({}^t r_{ij})\left[{}^t\mathbf{r}_{ij}\cdot\left({}^t\mathbf{p}_j-{}^t\mathbf{p}_i\right)\right]^2+\lambda_h\left({}^t r_{ij}\right)\left(\dfrac{1}{\theta_i}-\dfrac{1}{\theta_j}\right)\right]\end{array}\right\} \tag{35}$$

The form of L^{dif} is given by[29]

$$L^{dif} \equiv \sum_{i,j\neq i}^{N}\left\{\begin{array}{l}\dfrac{\partial}{\partial {}^t\mathbf{p}_i}\cdot\dfrac{1}{2}\Gamma_{ij}^{2}\,{}^t\mathbf{r}_{ij}\,{}^t\mathbf{r}_{ij}\cdot L_{ij}+ \\ \dfrac{\partial}{\partial u_i}\left[\dfrac{1}{2m_i}\left({}^t\mathbf{p}_j-{}^t\mathbf{p}_i\right)\cdot\dfrac{1}{2}\Gamma_{ij}^{2}\,{}^t\mathbf{r}_{ij}\,{}^t\mathbf{r}_{ij}\cdot L_{ij}+\dfrac{1}{2}\Lambda_{ij}^{2}\left(\dfrac{\partial}{\partial u_i}-\dfrac{\partial}{\partial u_j}\right)\right]\end{array}\right\} \tag{36}$$

where the operator L_{ij} is defined by[29]

$$L_{ij}\equiv\left(\frac{\partial}{\partial {}^t\mathbf{p}_i}-\frac{\partial}{\partial {}^t\mathbf{p}_j}\right)+\frac{1}{2m_i}\left({}^t\mathbf{p}_j-{}^t\mathbf{p}_i\right)\left(\frac{\partial}{\partial u_i}+\frac{\partial}{\partial u_j}\right) \tag{37}$$

Imposing that the equilibrium probability distribution has the form of a Gibbs canonical distribution, Avalos et al.[29] deduced the following relationship between the coefficients of the dissipative and random force

$$\begin{aligned}\Gamma_{ij}^{2}&=2k_B\Theta_{ij}\zeta\left(r\right)\\ \Lambda_{ij}^{2}&=2k_B\lambda_h\left(r\right)\end{aligned} \tag{38}$$

Here, $\Theta_{ij}^{-1} = \frac{1}{2}\left(\frac{1}{\theta_i} + \frac{1}{\theta_j}\right)$. This is the statement of the fluctuation dissipation theorem for the DPDE system and is analogous to the statement of fluctuation dissipation theorem for DPD in equation (21) .

Ripoll et al.[39] demonstrated that both the micro canonical and canonical ensemble can be simulated using DPDE. They applied the DPDE model for simulation of a solid which was modeled as a quiescent fluid. Periodic boundary conditions were imposed in all three directions for the equilibrium case. In this work, the meso-particles used were point particles and they were used to simulate a quiescent fluid and not a solid. So the application of DPDE to simulation of crystalline solid remains uninvestigated. For the non-equilibrium case, the boundary conditions were periodic in two directions while a temperature gradient was imposed in the third. They demonstrated that DPDE methodology can be used to simulate heat flow under a temperature gradient and successfully simulated the Fourier law of heat conduction using DPDE. Using simple equations for the meso-temperature and mesoscopic thermal conductivity, they obtained a probability distribution for the energies of the particles in exact agreement with the theoretical predictions.

Lisal et al.[49] presented a formulation of DPD under isothermal, isobaric, isoenergetic and isenthalpic conditions along with the statements of fluctuation-dissipation theorem for these cases. The extension of Shardlow's[21] splitting scheme for the Velocity-Verlet algorithm, for particles of unequal mass, was presented for the first time in their work. The generic isobaric DPD formulation presented in their work for the Langevin barostat[50] can be specialized to Hoover barostat[50]. The isobaric and isoenergetic formulations were combined to obtain an isenthalpic formulation[49]. Building on the work

of Groot and Warren[46] on the equation of state of a DPD fluid, a single DPD fluid and a mixture of two different DPD fluids was simulated in their work. The interactions between the fluid particles were modeled using a soft repulsive interaction similar to equation (22) in the work of Groot and Warren[46]. Additionally, a coarse grained solid that represented Ni in terms of physical and chemical properties was simulated in their work. The inter-particle interactions between the coarse grained Ni particles were modeled using a shifted Sutton-Chen embedded potential[51]. The model for solid Ni was obtained by agglomerating four f.c.c. unit cells into 1 coarse grained DPD particle. To utilize this level of coarse graining to model a micron sized particle at a sub-mesoscale or mesoscale regime would require enormous number of atoms thereby putting DPDE at the same disadvantage as MD.

1.2.3 Inter-Particle Potential

As mentioned earlier, the inter-particle conservative force $\mathbf{F}_{ij}^{C}$ is the major component, in addition to dissipative and random forces, that make DPDE applicable to any material (solid, liquid or gases) or a mixture of phases. $\mathbf{F}_{ij}^{C}$, which describes the chemical interactions between the particles is obtained from an inter-particle[52, 53] potential. Several potentials exist in literature such as Mie potential[54], Morse potential[55], Lennard-Jones potential[56], Smith-Bharadwaj[57] potential, etc.

Three important parameters are used to characterize the quality of potential: accuracy, transferability and computation cost. Accuracy refers to the extent to which a potential represents the inter-particle interactions. For computational chemistry, a highly accurate potential is desirable since material properties are computed from isolated molecules. The parameters of a potential are obtained by fitting to a set of experimental

data followed by optimization of the fit parameters[58]. Transferability[59] refers to the ability of the potential to adequately describe the inter-particle interactions in new situations to which it was not fit. The calculation of forces from some potentials such as Lennard-Jones and Mie potential is computationally less expensive compared to more complicated potentials. This affects the speed of computation and consequently the computational cost characteristic of the potential is important. The existing potentials can also be classified based on their range as short range or long range potentials. A potential is considered short range if the force derived from it decreases with inter-particle distance, r, quicker than r^{-d}, where d is the dimensionality of the system. To reduce computation time, a potential can also be specified with a suitable cut off beyond which it is assumed to be zero, thereby limiting its range. Van der Waals forces are short range interactions while coulomb forces are long range interactions. Potentials can also be classified as soft and hard potentials depending upon the behavior of the potential as the inter-particle distance approaches zero. As the inter-particle distance is reduced to zero, the inter-particle force approaches infinity for a hard potential while for a soft potential the inter-particle force approaches a finite limiting value.

The Mie potential[54] and its variant, the Lennard-Jones potential[56], are well known in literature. The Mie potential[54] is given as

$$V_{mie}(r) = \left(\frac{n}{n-m}\right)\left(\frac{n}{m}\right)^{m/(n-m)} \varepsilon_{pot}\left[\left(\frac{\sigma_{pot}}{r}\right)^{n} - \left(\frac{\sigma_{pot}}{r}\right)^{m}\right] \tag{39}$$

Here, r is the inter-particle distance, ε_{pot} is the well depth and σ_{pot} is the inter-particle distance where the potential V_{mie} is zero. m and n are parameters of the Mie potential that can be adjusted to describe different materials[4]. The Mie potential and its

variants have been extensively used for modeling solids[60-62] and fluids[63]. The Lennard-Jones potential is a special case of the general Mie potential with $n=12$ and $m=6$.

Morse potential[55] and its variants have been extensively used for metals[64, 65] and diatomic molecules[66]. The form of the Morse potential is given as[55]

$$V_{morse}\left(r\right)=\varepsilon_{pot}\left(1-e^{-a_{pot}\left(r-r_e\right)}\right)^2 \tag{40}$$

Here, r_e is the equilibrium bond distance. a_{pot} is the parameter that controls the width of the potential.

Zarkova et al.[67] presented the Lennard–Jones potential with temperature dependent parameters for ethane, propene, butane and cyclopropane. The form of this potential is given by[67]:

$$V_{zar}\left(R,T\right)=\frac{\varepsilon_{pot}\left(T\right)}{n-6}\left[6\left(\frac{R_m\left(T\right)}{R}\right)^n-n\left(\frac{R_m\left(T\right)}{R}\right)^6\right] \tag{41}$$

Here, $V_{zar}\left(R,T\right)$ is the intermolecular interaction energy which is a function of temperature; R is the center of mass distance; $R_m\left(T\right)$ is the equilibrium distance; $\varepsilon_{pot}\left(T\right)$ is the potential well depth which has a dependence on temperature and n is the repulsive parameter. The functional forms of $R_m\left(T\right)$ and $\varepsilon_{pot}\left(T\right)$ are respectively given by:

$$R_m\left(T\right)=R_m\left(T=0\text{ K}\right)+\delta_0\cdot f\left(T\right) \tag{42}$$

Here, the term $\delta_0\cdot f\left(T\right)$ accounts for the effective enlargement of molecular size. In the potential of Zarkova et al.[67], the potential well depth $\varepsilon_{pot}\left(T\right)$ is given as

$$\varepsilon_{pot}\left(T\right)=\varepsilon_{pot}\left(0\right)\left[R_m\left(0\right)/R_m\left(T\right)\right]^6 \tag{43}$$

Al-Matar et al.[68] presented a form of Lennard-Jones potential using temperature dependent interaction parameters. Interaction parameters as a function of temperature were determined from an optimization process. The form of the potential is

$$V_{alm}(r) = 4\varepsilon_{pot}\left[\left(\frac{\sigma_{pot}}{r}\right)^{12} - \left(\frac{\sigma_{pot}}{r}\right)^{6}\right] \tag{44}$$

The optimized interaction parameters as a function of temperature in the potential of Al-Matar et al.[68] are given by

$$\begin{aligned} \sigma_{pot} &= 3.672 - \frac{22.30}{T} \\ \frac{\varepsilon_{pot}}{k_B} &= 117.655 + \frac{778.012}{T} \end{aligned} \tag{45}$$

The potential was applied to the study of Argon.

Abell[69] introduced the REBO potential that has the form:

$$V_{abe}(r) = \sum_i \sum_{j>i} f_c(r)\left[V_R(r) + \overline{b_{ij}} V_A(r)\right] \tag{46}$$

Here, V_A, V_R *and* r are respectively the attractive part, the repulsive part and the interatomic distance between the particles. $\overline{b_{ij}}$ is the bond order term that represents the weakening of the bond due to bond rotation, torsion and coordination number. f_c is the cutoff function that limits the interactions to nearest neighbor particles. Originally, V_A and V_R were represented by Morse type terms which was too restrictive. In the second generation REBO potentials[70], the interatomic interactions V_R and V_A are given as

$$V_R(r) = \left[1 + \frac{Q_{rebo}}{r}\right] A \exp(-\alpha_{rebo} r)$$
$$V_A(r) = \sum_{n=1,3} B_n \exp(-\beta_n r) \tag{47}$$

Here, Q_{rebo}, α_{rebo} and β_n are parameters. In the temperature dependent REBO potential[71], A and B_n are assumed to be temperature dependent so that the form of V_R and V_A are given as

$$V_R(r) = \left[1 + \frac{Q_{rebo}}{r}\right] A(T) \exp(-\alpha_{rebo} r)$$
$$V_A(r) = \sum_{n=1,3} B_n(T) \exp(-\beta_n r) \tag{48}$$

In equation (48), the temperature dependence is embodied in the coefficients $A(T)$ and $B_n(T)$

Ackland[72] presented a temperature dependent form of potential for Ti which is given by

$$V_{ack}(r) = \sum_j \sum_k H(r_k - R_{ij}) a_k (r_k - R_{ij})^3 +$$
$$\sum_j A_T T^2 X^2 (1 - X)^2 H(r_0 + d - R_{ij}) H(R_{ij} - r_0) \tag{49}$$
$$-\sqrt{\sum_j \sum_k H(R_k - R_{ij}) A_k (R_k - R_{ij})^3}$$

Here, R_{ij} is the separation between i and j nearest atoms, H is the Heaviside step function and the other parameters (a_k, r_k, A_k, R_k) are specified in Ackland[72]. The parameter X is given by

$$X = (r - r_0)/d \tag{50}$$

where the range of interaction is from r_0 to $r_0 + d$

Several works have used the embedded atom potential (EAM) potential or its variation for MD simulation of solids especially metals[73-75]. The basic form of the EAM[76] potential is given by

$$V_{eam}(r) = \sum_i F_i(\rho_{h,i}) + \frac{1}{2}\sum_{\substack{i,j \\ i \neq j}} \phi_{ij}(r) \tag{51}$$

where ϕ_{ij} is the short-range pair potential, F_i is the embedding function. The host density, $\rho_{h,i}$, is assumed to be closely approximated by a sum of atomic densities ρ^a of the constituents, that is $\rho_{h,i} = \sum_{j \neq i} \rho_j^a(r)$. Here, ρ_j^a is the contribution to the density from atom j, where $\rho_{h,j}$ is the total host electron density at atom j. In this case, the energy is a function of the positions of atoms.

Holian et al.[73] presented a model EAM potential of the form

$$V_{hol}(r) = \sum_{i=1}^{N}\left[\frac{1}{2}\sum_{j \neq i}\varphi(r) + \Gamma(\rho_i)\right] \tag{52}$$

Here, φ is a density independent, pairwise additive contribution depending only on the distance r between particles and Γ is the embedding energy. Γ is a function of the local embedding density ρ_i at atom 'i', given by a pairwise sum over all neighboring particles, weighted by a spherical localization function. A nonlinear function of embedding density results in higher order many-body contributions. The function φ is taken to be the spline Lennard-Jones potential. The spline φ has been used for simulation of anisotropic response and elastic-plastic shock wave profiles for single crystals[77]. The embedding

energy function Γ is taken to be a nonlinear function that depends on the dimensionality of the system.

Berne and Pechukas[78] considered each molecule as approximated by a uniaxially stretched Gaussian distribution of the form

$$\begin{aligned} &G(\mathbf{r}) = |\gamma|^{-1/2} \exp\left(-\mathbf{r}\cdot\gamma^{-1}\cdot\mathbf{r}\right) \text{ where} \\ &\gamma = \left(l^2 - d^2\right)\hat{\mathbf{u}}\hat{\mathbf{u}} + d^2\mathbf{I} \end{aligned} \tag{53}$$

Here, $\hat{\mathbf{u}}$ and $\mathbf{I}$ are respectively the unit vector along the principal axis of the particle with length l and breadth d, and $\mathbf{I}$ is the identity matrix. Their potential is able to account for anisotropy. In Berne and Pechukas[78] approach, the potential between two interacting particles is of the form

$$V_{bp}\left(\hat{\mathbf{u}}_i, \hat{\mathbf{u}}_j, \mathbf{r}_{ij}\right) = \varepsilon_{pot}\varepsilon_1\left(\hat{\mathbf{u}}_i, \hat{\mathbf{u}}_j\right)\exp\left[-r^2 \Big/ \sigma_{pot}^2\left(\hat{\mathbf{u}}_i, \hat{\mathbf{u}}_j, \mathbf{r}_{ij}\right)\right] \tag{54}$$

Here, ε_1 is the strength anisotropy function. Several variations of this potential exist in literature[79-81].

Stillinger and Weber[82] presented a potential for silicon based on the idea that any potential energy function Φ describing interactions amongst N identical particles can be resolved into one body, two-body and three-body term and so on upto N body contributions as

$$V_{sw}(1,2,...,N) = \sum_i V_i(i) + \sum_{\substack{i,j \\ i<j}} V_i(i,j) + \sum_{\substack{i,j,k \\ i<j<k}} V_i(i,j,k) + ... + V_N(1,...,N) \tag{55}$$

Here, the one body term, $V_i(i)$, represents external forces. $V_i(i,j)$ and $V_i(i,j,k)$ respectively model two body interactions and three body interactions. In the generalized

formulation, upto N body interactions can be considered. They considered upto three body interactions and specified their forms[82].

Smith et al.[83] developed a force field for Dimethylnitramine (DMNA) and extended their work to develop a potential for HMX[57]. Molecular geometries were optimized using quantum chemistry calculations and conformational energies for nitramide and dimethylnitramine (DMNA) were obtained using different basis sets. The potential was validated through gas and liquid phase MD simulations[83]. DMNA was chosen as a building block for developing a force field for HMX and RDX for MD simulations[57]. However, the force field was developed at the atomic and molecular length scales and not for the sub-micron and micron length scale regimes.

Numerous potentials exist in literature[59]. Mishin provides a review of interatomic potentials for metals[84]. All the above potentials are for atomistic simulations. Their application to micron length scale remains unclear and has not been attempted to the best of knowledge, except for the phenomenological extension of Lennard-Jones form of potential by Yano et al[4].

Several works exist on the construction of these mesoscopic potentials and the determination of the potential parameters[85-88]. Reith et al.[85] presented a methodology for constructing mesoscopic potentials from full atomistic simulations. A potential is guessed and a simulation is performed based on a guessed potential. The distribution function obtained from the guessed potential is compared with the simulated distribution to improve the guess. This is essentially a self-consistency scheme. The methodology is applied to poly-isoprene to demonstrate the scheme. Forrest and Suter[86] introduced the bottom up scheme for coarse graining polymer chains in melts. They demonstrated the

spatial and temporal averaging needed to represent polymer chains as mesoscopic bead particles and applied the procedure to a melt of 20 C24 chain polymers.

Izvekov et al.[89] presented a bottom up scheme for constructing coarse grained models of biomolecules from atomistic MD simulations using a force matching technique. They assumed a linear dependence of force on the fitting parameters and obtained a coarse grained model of DPMC bilayer. They validated their coarse grained model against MD simulations and observed good agreement between the radial density functions (RDF) obtained from their coarse grained model and the all atomistic MD simulations. While their model yielded good agreement with MD simulations for RDF, the pressure dependence of the material was not accurately modeled. This limited the transferability of the model. In a later work, Izvekov et al.[90] proposed an improvement in their coarse grained model[89] by incorporating density dependence in it. The improved model showed better transferability across different densities. Mukherjee et al.[91] presented a systematic methodology for constructing coarse grained models of liquid crystalline compounds. Steve et al.[92] have presented a detailed review of coarse grained models.

It is clear that the above mentioned methodologies have been developed for soft polymeric materials at macro-molecular length scales. For the simulations at micron and submicron length scales for solids performed in this work, a form of inter-particle potential is required. The methodologies mentioned in the literature apply to coarse graining to macromolecular level and not to micron length scale. This presents a challenging situation. We have circumvented this problem by using a Lennard-Jones form[4] of potential at this point.

1.2.4 Boundary Conditions in DPDE

The DPDE simulation of plate impact experiment would require appropriate wall boundary conditions to prevent the escape of particles from an RVE. In general, the statistical volume element (SVE) may have periodic boundary conditions[93] imposed in the directions lateral to shock propagation to computationally simulate infinite extent lateral to shock propagation[11, 12, 93, 94] or there may be walls that prevent the escape of the particle from SVE. Since large amount of experimental data exists for shock propagation in one dimension in which the specimen is assumed to be infinite in the lateral dimensions, periodic boundary conditions provide a way to model this infinite extent with small number of particles. Alternatively, the SVE may be bounded by walls. Walls are a way to conserve mass by not allowing particles to escape from the simulation cell. In a wall bounded DPD system, material properties such as density and pressure show fluctuations close to the wall. Not only are these fluctuations nonphysical in nature, the fluctuations starting at the wall may propagate into the interior of the simulation cell making the simulation itself numerically unstable. Several ways of imposing wall boundary conditions on the SVE composed of meso-particles interacting via dissipative particle dynamics interactions exist in literature[95-99].

Altenhoff et al.[95] presented a method for simulating a stochastic boundary based on the fluctuations in the corresponding homogeneous system at equilibrium. In this approach, an imaginary wall is introduced within a homogeneous system. The total force exerted by the wall on the particle is of stochastic nature. The boundary conditions[95] are obtained by modifying the virial pressure term in homogeneous system. The success of the method was demonstrated by applying it to simulate Poiseuille flow and flow near an

oscillating plate. The fluctuations in temperature and density near the walls were significantly reduced but in regions very close to the walls some fluctuation effects remained.

Revenga et al.[96] presented three possibilities for imposing wall conditions in a DPD simulation: specular, bounce back and a stochastic Maxwell Boltzmann type of wall. The results for three types of walls were compared. In a specular wall, the component of particle velocity normal to the wall is reversed while the components tangential to the wall are left unchanged. In a bounce back wall, all three components of the velocity of the particle are reversed. In a Maxwell Boltzmann type of stochastic wall, the particle is injected back into the simulation cell with a velocity chosen from the Maxwell Boltzmann distribution corresponding to the temperature of the wall. In another work by Revenga et al.[97] , a DPD fluid in contact with a wall was modeled. The wall was composed of frozen DPD particles with a very high number density of particles that approached continuum. The DPD particles interacted with this frozen entity. Any particle that crosses the wall in a simulation step is put back into the simulation cell either by specular reflection, a bounce back reflection or by Maxwell-Boltzmann injection. This ensured impenetrability of walls and conserved system mass.

Wang et al.[98] presented a new wall boundary condition which combined the characteristics of the Maxwell's boundary conditions and the bounce back condition. On reflection from a wall, the components of velocity tangential to the wall are reversed while the component of velocity normal to the wall is given a value from the Maxwell-Boltzmann distribution of velocities at the same temperature as the walls. Simulation of the Poiseuille flow showed excellent agreement with the theoretical results.

Pivkin et al.[99] introduced a new way to impose no slip boundary conditions. The method was based on freezing DPD particles and combining this with bounce back conditions. The method involves computing the average force exerted by wall such that, within the cutoff radius, this force is balanced by the force exerted by the fluid. In doing this an effective interaction coefficient is assigned to the wall particles based on the average force per unit area exerted by the walls on a plane certain distance from the wall. The efficacy of the method was demonstrated by simulation of Poiseuille flow where it was found that the density and temperature fluctuations introduced by the wall in the middle of the fluid region were significantly reduced. Some fluctuations at the walls did remain however.

It is evident that several boundary conditions for DPD have been reported in literature and they may be adaptable to DPDE because of the close relationship between DPD and DPDE. However, these boundary conditions cannot be directly used for solid walls composed of micron length scale particles because of the finite extent of the micron sized particles. The formulation of correct wall conditions for micron sized particles forming the walls of the RVE presents a challenging problem.

1.2.4 In-situ Shock Deformation Quantities

The output from a particle method such as MD, DPD, or DPDE are the positions, velocities and forces on particles at every time step of the simulation. These quantities because of their very nature are discrete, pertaining to the specific particles that make up the simulated system. Since the micron sized particles are intended to simulate a continuum system, the derivation of continuum properties such as energy and mass densities, energy flux and stresses from the output obtained in a particle method is of

enormous interest. In addition, for many cases of interest, the experimental response of a material treated as a continuum is well known. Comparison of simulated results with experimental values provides a check on the correctness of the particle methods. The question of determining the local field properties that pertain to the continuum from the output obtained in a particle simulation has been addressed in several works.

Irving and Kirkwood[100] derived the equations of mass, momentum and energy transport from the statistical mechanics point of view for a single component, single phase fluid system and obtained expressions for the stress tensor and the heat flux in terms of microscopic variables. They showed that the equations of hydrodynamics retain their form when expressed in terms of the positions, velocities and inter-particle interactions-that is in terms of the properties of the particles constituting the fluid system. They assumed the forms of the densities of mass, momentum and energy and by requiring that these satisfy the form invariant hydrodynamic equations, they derived the expressions for the momentum and energy fluxes. These expressions for the fluxes contained both kinetic contributions and contributions from interparticle interactions. However, as noted by Hardy[101], their approach suffers from two main limitations. First, their formulas for the potential contribution to the heat flux and stresses contain infinite series which needs to be truncated for computation sake, thereby introducing an approximation in the computation of the potential part of stress and heat flux. Secondly, their formulation uses a Dirac Delta function for the position which also needs to be approximated.

Hardy[101] presented formulas for determining the local continuum properties such as mass density, energy density, energy flux and stresses from the MD simulation using a

smooth localization function. The potential contribution to the heat flux and stresses in Hardy's formulation[101] does not contain infinite series and is therefore exact when numerically computed. The local properties at a point are associated with weighted averages over a region of length l around that point. In Hardy's work, the influence of a particle to a local property at a specific point is determined by the localization function, Δ . The localization function Δ is any non-negative function that has a peak at the particle position ${}^t\mathbf{r}_i$ and tends to zero away from the particle. The localization function is normalized to the volume of the averaging domain and satisfies

$$\int_{\Omega} \Delta(\mathbf{r}) d^3 r = 1 \tag{56}$$

where $\Omega \subset R^3$ is domain of interest. For shock propagation in one dimension, the step function normalized with the volume of the averaging domain is a convenient choice. For three dimensional case, a three dimensional Gaussian can be used. The integral of the localization function along the line connecting the two particles defines the bond function. The bond function is defined as

$$B\left({}^t\mathbf{r}_i, {}^t\mathbf{r}_j, \mathbf{R}\right) \equiv \int_0^1 \Delta\left(\tau\, {}^t\mathbf{r}_{ij} + {}^t\mathbf{r}_j - \mathbf{R}\right) d\tau \tag{57}$$

τ is the variable of integration. $\mathbf{R}$ is the position vector of the field point along the line connecting the two particles. Bond function accounts for the contribution of the interparticle interaction to the momentum and energy flux.

In Hardy's work, the contribution of a particle to heat flux and momentum flux has two components: the potential contribution and the kinetic contribution. The potential contribution arises from the forces between the particles due to their interparticle

interaction. The kinetic contribution arises from the motion of the particles. Hardy's work gives the Cauchy stress in terms of the spatial coordinates. The Cauchy stress expression given by Hardy has the form

$$S_T^{\alpha\beta} = S_K^{\alpha\beta} + S_V^{\alpha\beta} \tag{58}$$

where $S_T^{\alpha\beta}, S_K^{\alpha\beta}, S_V^{\alpha\beta}$ are respectively the $\alpha\beta$ component of the total, kinetic and potential contribution to the stress tensor. The kinetic and potential contributions to the stress tensor, $S_K^{\alpha\beta}$ and $S_V^{\alpha\beta}$ are respectively given by

$$\begin{aligned} S_K^{\alpha\beta}(\mathbf{R},t) &= -\sum_i \left[m_i \left(\dot{r}_i^{\alpha} - u^{\alpha} \right) \right] \left(\dot{r}_i^{\beta} - u^{\beta} \right) \Delta\left({}^t\mathbf{r}_i - \mathbf{R} \right) \\ S_V^{\alpha\beta}(\mathbf{R},t) &= -\frac{1}{2} \sum_{ij} \mathbf{F}_{ij}^{\alpha} r_{ij}^{\beta} B\left({}^t\mathbf{r}_i, {}^t\mathbf{r}_j, \mathbf{R} \right) \end{aligned} \tag{59}$$

Here, m_i is the mass of particle i. $\dot{r}_i^{\alpha}$ and $\dot{r}_i^{\beta}$ are α and β component of the velocity of the particle 'i', ${}^t\mathbf{v}_i$. $\mathbf{u}$ is the local mass averaged velocity whose α and β components are respectively u^{α} and u^{β}. $\mathbf{F}_{ij}^{\alpha}, r_{ij}^{\beta}, B\left({}^t\mathbf{r}_i, {}^t\mathbf{r}_j, \mathbf{R} \right)$ are respectively the α component of the conservative interparticle interaction force, β component of the relative position vector ${}^t\mathbf{r}_{ij}$, and bond function respectively between the two particles 'i' and 'j'. The pressure is negative of the one third of the trace of stress tensor. Based on their definitions of mass, energy and momentum density along with the expressions for stresses and the pressures computed from them, Hardy showed that the Rankine-Hugoniot equations across the shock front are automatically satisfied with their formulation. Based on this formulation, Hardy et al.[102] also computed local velocity, temperature and pressure in MD simulations of shock propagation in 2D and compared the results of using a cosine localization function with a step function localization

function. Zimmerman et al.[103] extended Hardy's work to include temporal averaging and compared the stress obtained from Hardy's formulation with the atomic stress evaluated from virial theorem. They demonstrated that Hardy's formulation converges more rapidly to the continuum values than volume averages of the local virial stress for finite temperature deformations.

Zimmerman et al.[104] presented a material frame approach for determining continuum variables in atomistic simulations. Their approach gives the first Piola-Kirchhoff stress. Zimmerman's expression for the first Piola-Kirchoff stress is

$$\mathbf{P}(\mathbf{X},t) = -\frac{1}{2}\sum_{j=1}^{N}\sum_{i\neq j}^{N}\mathbf{F}_{ij}^{C} \otimes {}^{0}\mathbf{r}_{ij} B(\mathbf{X}) \tag{60}$$

Here, $\mathbf{P}(\mathbf{X},t)$ is the first Piola-Kirchhoff stress at the material coordinate $\mathbf{X}$. $\otimes$ denotes the tensor product. ${}^{0}\mathbf{r}_{ij} = {}^{0}\mathbf{r}_{i} - {}^{0}\mathbf{r}_{j}$ where ${}^{0}\mathbf{r}_{i}$ and ${}^{0}\mathbf{r}_{j}$ are the material coordinates of the particles 'i' and 'j'. $B(\mathbf{X})$ is the bond function for the particle pair 'i' and 'j' in the reference configuration. In contrast to Hardy's formulation, Zimmerman's[104] work computes field properties in material coordinates, that is as a function of reference configuration. Besides, in Zimmerman's work, the contribution to stress and heat flux does not contain the kinetic contribution. The first Piola-Kirchhoff stress as computed by Zimmerman[104] and the Cauchy stress as computed in Hardy's work[101] is related by Piola transform. Zimmerman demonstrates the consistency of his material frame approach with Hardy's spatial frame approach by computing the Cauchy stress from the first Piola-Kirchhoff stress through the Piola transform. Comparison with the Cauchy stress computed directly from Hardy's approach shows good agreement between the two approaches.

Shen et al.[105] defined a stress tensor based on SPH[3] approach. In contrast to Hardy's[101] and Zimmerman's[104] approach, the averaging method of Shen et al.[105] does not rely on selecting an averaging volume. Since the averaging volumes are not always known unambiguously a priori, this is an important advantage. Shen et al.[105] also define an equivalent continuum for a MD system based on SPH and their definition of continuum stress. The formulation is validated by numerical examples and the method yields smooth and highly continuous fields for both homogeneous and non-homogeneous deformation. Subramaniyan et al.[106] demonstrated the significance of the kinetic term in the virial stress. The kinetic part of the virial stress accounts for the thermal motion in the material. They showed that for finite temperatures, the kinetic contribution must be taken into account even for solids. Based on theoretical arguments and numerical simulations, they demonstrated the equivalence of spatially and temporally averaged virial stress and Cauchy stress provided the kinetic contribution is taken into account.

Eapen et al.[107] employed statistical inference techniques to obtain continuum fields from the output of MD simulation. In the statistical inference technique, the field variable is assumed to be a probability distribution function. There are two variants of the statistical inference approach, the parametric approach and the non-parametric approach. The parametric approach is used when the probability density distribution of the underlying particle property for which the field estimator is to be constructed is known while the non-parametric estimator is used when this probability density distribution is unknown. Since the probability distribution for the particle positions and stresses is not known, they are computed with the non-parametric approach. In the non-parameteric approach, the maximum entropy principle, with constraints in the form of statistical

moments of the physical quantity, is used to estimate the field. The statistical moments of the physical quantity are obtained from the discrete particle output of MD simulation.

All of the above mentioned schemes for obtaining continuum averages from discrete particle output have originally been developed for point particles. They are not directly applicable to micron sized particles which have a finite extent. An extension of these averaging schemes to micron sized particles needs to be developed. However, these averaging schemes provide guidelines and a framework on which the averaging for micron sized particles utilized in this work can be formulated.

From above discussion, it is clear that DPDE has all the features needed to simulate multi-phase, multi-length scale phenomenon that are encountered during the shock response of HE materials. DPDE is a relatively recent simulation technique that has Galilean invariance and isotropy intrinsically built into it. Therefore, DPDE methodology is physically sound compared to methods such as LGA. In MD, the time step should be small enough in the nanosecond regime so that the configuration change equivalent to a single mean free path is accomplished in several hundred time steps. However, DPDE allows a time step several orders of magnitude higher than MD. Besides, the modeling of mesoscale phenomenon using MD would require the simulation of several billions of atoms which is beyond the capability of most of the available computers. However, DPDE coarse grains, thereby reducing the number of particles and consequently the number of degrees of freedom of the system to be simulated are significantly reduced. Therefore, it is computationally efficient for mesoscale simulations. Like MD, DPDE is based on inter-particle interactions and consequently it is easily extendable. Simulation methodologies such as DEM are also based on inter-

particle interactions and thus preserve the simplicity and extensibility of MD. However, unlike DPDE, DEM is based on continuum mechanics phenomenologies and require separate heat transport solution. DPDE has a rigorous statistical mechanics approach with in-built heat transport. DPDE incorporates in a rigorous manner the fundamental principle of energy conservation in addition to mass and momentum conservation and therefore is well suited to model phenomenon where energy exchanges need to be explicitly taken into account. The built in energy conservation in the DPDE formulation allows heat transfer to be simulated without the need for separately solving heat transport equations. DPDE has already been demonstrated to successfully model phenomenon at the atomic and molecular length scales for gases and polymers from where it originated. However, DPDE has not been applied to solids and at micrometer length scales. This work is the first attempt to extend DPDE methodology to model shock response of HE materials at mesoscale.

CHAPTER 2

OBJECTIVES

The detailed discussion in the preceding chapter shows that MD is a well-established simulation technique at the atomic and molecular length scales while FEM is a well-established modeling and simulation methodology for length scales above few microns. However, the two methods and others like DEM, are deficient in simulating materials' response at micron and sub-micron mesoscale with heterogeneities. DPDE method has the requisite features for simulating the mesoscale response on account of being based on sound statistical mechanics basis, built-in heat transport, and being derived from fundamental molecular level void of any continuum mechanics phenomenologies. However, the method has not been applied at micron and submicron length scale of any material in general and of solids in particular. The objectives of the present research work are to:

1. Develop and extend DPDE method to simulate response of solid materials at micron and sub-micron length scales found at materials' mesoscale.
2. Develop and integrate in-situ averaging method to retrieve in-situ deformation parameters from DPDE simulation results for comparison with available analytical solution and experimental data.
3. Validate the results at progressive stages of development with the results available in literature for ideal gas, equation-of-state of DPD fluid and

analytical results for one dimensional (1D) Fourier heat flow and quasi-static compression of solids at micron length scales.

4. Simulate the shock response of HE materials at micron length scales for an assumed planar plate impact experiments and compare the retrieved in-situ averaged shock quantities with experimental data.

CHAPTER 3

SIMULATION METHODOLOGIES

The detailed formulation of DPD and DPDE are now presented as it is extended and applied in this work. The formulation is generic and can be used for any loading condition by specifying appropriate initial and boundary conditions. A generic methodology for averaging discrete particle output obtained from a particle method to obtain continuum field quantities is also presented.

3.1 DPD Formulation

In DPD, the particles interact via a conservative force that takes into account the chemical interaction between the particles, a dissipative force and a random force[46]. The dissipative forces tend to extract energy from the system while the random forces input energy into the system. The combination of dissipative and random forces acts as a thermostat. When the system is coarse grained, the degrees of freedom of the system are reduced. The dissipative and random forces tend to compensate, in an average manner, for the lost degrees of freedom of the system, a key feature that distinguishes stochastic methodologies such as DPD and DPDE from coarse grained MD. Each DPD particle, 'i', is characterized by a position vector ${}^t\mathbf{r}_i$, mass m_i and momentum ${}^t\mathbf{p}_i$. The total force, ${}^t\mathbf{f}_i$, exerted on the particle 'i' by its neighboring particle 'j', at time *t*, is given as[46]

$$ {}^t\mathbf{f}_i = \sum_{j \neq i} \left({}^t\mathbf{F}_{ij}^P + {}^t\mathbf{F}_{ij}^D + {}^t\mathbf{F}_{ij}^R \right) \tag{61} $$

Here, the force components ${}^{t}\mathbf{F}_{ij}^{P}$, ${}^{t}\mathbf{F}_{ij}^{D}$, ${}^{t}\mathbf{F}_{ij}^{R}$ are respectively the conservative inter-particle potential force, dissipative force and random force between the particles 'i' and 'j' as specified in equation (30) and the sum runs over all particles within a cut off radius r_c. In the DPD simulation, the cut off radius was assumed to be unity.

In this work, the conservative force between the DPD particles was taken to be a soft repulsive interaction of equation (22) with[46] $a_{ij} = a$

$$\begin{aligned} {}^{t}\mathbf{F}_{ij}^{P} &= a\left(1 - {}^{t}r_{ij}\right){}^{t}\mathbf{n}_{ij} \qquad \left({}^{t}r_{ij} < 1\right) \\ &= 0 \qquad\qquad\qquad\qquad \left({}^{t}r_{ij} \geq 1\right) \end{aligned} \tag{62}$$

Here, a is the repulsion parameter that controls the strength of the soft repulsive interaction. Different materials can be modeled by changing the value of the repulsion parameter a.

The dissipative and random forces are given as[46]:

$$\begin{aligned} {}^{t}\mathbf{F}_{ij}^{D} &= -\gamma_{ij}\omega^{D}\left[{}^{t}\mathbf{n}_{ij} \cdot {}^{t}\mathbf{p}_{ij}\right]{}^{t}\mathbf{n}_{ij} \\ {}^{t}\mathbf{F}_{ij}^{R} &= m_{ij}\sigma_{ij}\omega^{R}\varsigma_{ij}\Delta t^{-0.5}\,{}^{t}\mathbf{n}_{ij} \end{aligned} \tag{63}$$

where γ_{ij} and σ_{ij} are respectively the amplitudes of the dissipative and random forces, ω^{D} and ω^{R} are the weight functions of the dissipative and random forces respectively as defined in equation (5). ς_{ij} is a random number from the standard normal distribution with zero mean and unit variance.

As demonstrated by Espanol and Warren[42], the dissipative and random forces are not independent. The amplitudes of the dissipative and random force are related to one another by dissipation-fluctuation theorem as given in equation (64)

$$\sigma^2 = 2\gamma\left(\frac{k_B T}{m}\right) \tag{64}$$

For DPD simulation, the mass m was taken to be unity, in which case equation (64) and equation (21) become identical. The weight functions of the dissipative and random forces are related by the dissipation- fluctuation theorem and in this work were assumed to be of the form[46]

$$\begin{aligned} \omega^D = \left(\omega^R\right)^2 &= \left(1 - \frac{{}^t r_{ij}}{r_c}\right)^2 \qquad \text{for } {}^t r_{ij} < r_c \\ &= \quad 0 \qquad\qquad \text{for } {}^t r_{ij} \geq r \end{aligned} \tag{65}$$

where r_c is the interaction range for the dissipative and random interactions. For DPD simulation, the interaction range was taken to be unity.

The Newton's equations of motion of the particles for unit mass are given as:

$$\frac{d\,{}^t\mathbf{r}_i}{dt} = {}^t\mathbf{v}_i, \qquad \frac{d\,{}^t\mathbf{v}_i}{dt} = {}^t\mathbf{f}_i \tag{66}$$

The equations of motion were integrated using the modified velocity-Verlet suggested by Groot and Warren[46]

$$\begin{aligned} {}^{t+\Delta t}\mathbf{r}_i &= {}^t\mathbf{r}_i + \Delta t\,{}^t\mathbf{v}_i + \frac{1}{2}(\Delta t)^2\,{}^t\mathbf{f}_i \\ {}^{t+\Delta t}\tilde{\mathbf{v}}_i &= {}^t\mathbf{v}_i + \lambda \Delta t\,{}^t\mathbf{f}_i \\ {}^{t+\Delta t}\mathbf{f}_i &= \mathbf{f}_i\left({}^{t+\Delta t}\mathbf{r}_i, {}^{t+\Delta t}\tilde{\mathbf{v}}_i\right) \\ {}^{t+\Delta t}\mathbf{v}_i &= {}^t\mathbf{v}_i + \frac{1}{2}\Delta t\left({}^t\mathbf{f}_i + {}^{t+\Delta t}\mathbf{f}_i\right) \end{aligned} \tag{67}$$

Here λ is a constant. Following Groot and Warren[46], the constant λ was taken to be 0.5.

The DPD method conserves both mass and momentum. However, it is essentially an isothermal method and cannot be used where energy and temperature changes need to

be explicitly taken into account. This is a severe limitation if phenomenon such as heat conduction and shock propagation in solids need to be modeled. This limitation of DPD is overcome by adding energy conservation to the DPD methodology to obtain the DPDE methodology.

3.2 DPDE Formulation

In the DPDE methodology, the particles interact via deterministic conservative forces and stochastic dissipative and random forces just as for DPD. In addition, the present work introduces an artificial viscosity force for the first time in the DPDE formulation to suppress the numerical oscillations associated with shock loading of materials. Similar to DPD, in the DPDE formulation, each DPDE particle, 'i', is characterized by a position vector ${}^t\mathbf{r}_i$, mass m_i and momentum ${}^t\mathbf{p}_i$. The total force exerted on the particle 'i' by its neighboring particle 'j', at time *t*, ${}^t\mathbf{f}_i$, is the given as

$$ {}^t\mathbf{f}_i = \sum_{j \neq i} \left({}^t\mathbf{F}_{ij}^P + {}^t\mathbf{F}_{ij}^D + {}^t\mathbf{F}_{ij}^R + {}^t\mathbf{F}_i^{ext} + {}^t\mathbf{F}_{ij}^v \right) \tag{68} $$

Here, ${}^t\mathbf{F}_{ij}^P$, ${}^t\mathbf{F}_{ij}^D$ and ${}^t\mathbf{F}_{ij}^R$ are the same force components as for DPD in equation(61). ${}^t\mathbf{F}_i^{ext}$ is the external force acting on particle 'i.' ${}^t\mathbf{F}_{ij}^v$ is the artificial viscosity force between the particles. DPDE is based on integrating the equations of motion of particles subject to the forces in equation (68), and in this sense is similar to MD simulations .

The functional form of the dissipative and random forces is the same as for the DPD methodology and specified above in equation (63). It is assumed in this work that the fluctuation-dissipation theorem is valid at the micron length scale and that the weight

functions of the dissipative and random forces in DPDE are given by equation (65) similar to DPD.

In this first attempt to extend DPDE to micron length scale, the inter-particle potential force is adapted from the work of Yano et al.[4], which is analogous to the Lennard-Jones potential force and is given as:

$$ {}^{t}\mathbf{F}_{ij}^{P} = \frac{A\alpha_{LJ} mn}{(n-m)} \left[\left(\frac{r_0}{{}^{t}r_{ij}} \right)^{n+1} - \left(\frac{r_0}{{}^{t}r_{ij}} \right)^{m+1} \right] {}^{t}\mathbf{n}_{ij} \tag{69} $$

where A is the cross sectional area of the particle, r_0 is the equilibrium inter-particle separation, and α_{LJ}, m and n are material parameters. Different materials can be modeled by determining their material parameters, α_{LJ}, m and n, as well as by using a different functional form of the inter-particle potential.

The artificial viscosity force is given by:

$$ {}^{t}\mathbf{F}_{ij}^{v} = -A \frac{{}^{t}\dot{r}_{ij}}{\left| {}^{t}\dot{r}_{ij} \right|} \left[C_1 \frac{\left| {}^{t}\dot{r}_{ij} \right|}{{}^{t}r_{ij}} + C_2 \left(\frac{{}^{t}\dot{r}_{ij}}{{}^{t}r_{ij}} \right)^2 \right] \quad ; \quad if \;\; {}^{t}\dot{r}_{ij} \left({}^{t}r_{ij} - r_0 \right) > 0 \tag{70} $$

where C_1 and C_2 are constants. The first term inside the brackets of equation (70) represents the linear artificial viscosity while the second term represents the quadratic artificial viscosity. The artificial viscosity term serves to damp out oscillations behind the discontinuous shock front and yields smooth shock wave profiles.

Energy conservation is incorporated in DPDE by assigning to each DPDE particle an internal energy variable u_i, and a meso-temperature θ_i. In this work, the internal energy

and meso-temperature are assumed to be related by an equation of state of the form given in equation (27):

$$u_i = mC_v\theta_i \tag{71}$$

where C_v is the specific heat of the material. Different materials can be modeled by incorporating a different equation of state in the formulation and consequently the formulation of DPDE presented in this work is completely generic. The amplitudes of the dissipative and random forces in the DPDE formulation are related by fluctuation-dissipation theorem as

$$\sigma^2 = 2\gamma\left(\frac{k_B}{m}\right)\Theta_{ij} \tag{72}$$

Equation (72) is the generalization of equation (64) for the case when each particle is assigned a meso temperature variable. Θ_{ij} is defined in terms of the mesoscopic temperatures, θ, of the particles 'i' and 'j', which are defined by equation (71), and is given as

$$\Theta_{ij}^{-1} = \left(0.5\left(\theta_i^{-1} + \theta_j^{-1}\right)\right) \tag{73}$$

It is worthwhile to mention that in DPDE each particle has an individual internal energy and meso-temperature variable associated with it. This allows the description of the system in terms of the energy exchange between the DPDE particles. In contrast, in DPD, the temperature variable is associated with the system as a whole and there is no description of energy exchange between the particles.

The internal energy of the DPDE particles can change by mechanical interaction and by mesoscopic heat conduction. In addition, a shock event is accompanied by energy

dissipation due to the formation of dislocations, vacancies, voids and other defects in the material. A major drawback of the Lennard-Jones like potential is that it does not model the inelastic response, the main mechanism for energy dissipation and defect formation in the repulsive phase. With the loading path being reversible, energy is released asymptotically to zero with the increase in inter-particle distance in the attraction phase. To circumvent this, and to test the temperature phenomenon during shock loading, it is assumed in this work that a certain fraction of the potential energy is dissipated as internal energy. Consequently, the change in internal energy is obtained as a sum of changes in internal energy due to mechanical, conductive, and dissipated potential energy interactions:

$$du_i = du_i^{mech} + du_i^{cond} + du_i^{pot} \tag{74}$$

where du_i^{mech}, du_i^{cond} and du_i^{pot} are respectively, the changes in internal energy due to mechanical interaction, conductive interaction and potential energy dissipated in defect formation in the material. Following Lisal et al.[49], the internal energy change due to mechanical interaction is given by:

$${}^{t+\Delta t}u_i^{mech} = {}^{t}u_i^{mech} - \frac{1}{2}\left[\frac{{}^{t+\Delta t}\mathbf{p}_i \cdot {}^{t+\Delta t}\mathbf{p}_i}{2m_i} - \frac{{}^{t}\mathbf{p}_i \cdot {}^{t}\mathbf{p}_i}{2m_i} + \frac{{}^{t+\Delta t}\mathbf{p}_j \cdot {}^{t+\Delta t}\mathbf{p}_j}{2m_j} - \frac{{}^{t}\mathbf{p}_j \cdot {}^{t}\mathbf{p}_j}{2m_j}\right] \tag{75}$$

The internal energy change due to conductive interaction[49] is given as:

$${}^{t+\Delta t}u_i^{cond} = {}^{t}u_i^{cond} + \Delta t\kappa_{ij}\left(\frac{1}{\theta_i} - \frac{1}{\theta_j}\right)\omega^{Dq} + \sqrt{\Delta t}\alpha_{ij}\omega^{Rq}\varsigma_{ij}^{q} \tag{76}$$

where κ_{ij} is the mesoscopic thermal conductivity, and ω^{Dq} and ω^{Rq} are the weight functions of the dissipative and random forces for mesoscopic heat conduction. The term

ζ_{ij}^{q} is a random number, from the standard normal distribution, with zero mean and unit variance. The weight functions for the dissipative and random interactions for heat transport are related by the fluctuation-dissipation theorem[49] and are given as

$$\omega^{Dq} = \left(\omega^{Rq}\right)^2 = \left(1 - \frac{{}^{t}r_{ij}}{r_c}\right)^2 \tag{77}$$

The mesoscopic thermal conductivity[49], κ_{ij}, is defined as:

$$\kappa_{ij} = \kappa_0 \frac{\left(mC_v\right)^2}{4k_B}\left(\theta_i + \theta_j\right)^2 \tag{78}$$

where κ_0 is a material constant. The parameters κ_{ij} and α_{ij} are related by fluctutation-dissipation theorem[49] by

$$\alpha_{ij}^2 = 2k_B\kappa_{ij} \tag{79}$$

Several integration schemes exist in literature for integrating the equations of motion of the DPDE system[19, 21, 46]. Most of these schemes[19, 49] are variants of the splitting scheme developed originally by Shardlow[21] for DPD. In the Shardlow splitting scheme[21], the equations of motion are integrated in two steps. In the first step, stochastic integration is performed and the velocities are updated for the effect of dissipative and random forces. In the second step, deterministic integration is performed in which the conservative forces are used to update the velocities for a half time step. From the updated velocities, new positions are computed and used to update the conservative forces. Then the velocities are again updated using the new conservative forces for another half time step. Shardlow's splitting scheme is limited to particles of equal mass.

Lisal[49] et al. presented a variation of Shardlow's splitting scheme for particles of unequal mass.

In our work, the integration of equations of motion is done using a modification of the integration scheme presented in Lisal[49] et al. and is given as

$$ {}^{t}\mathbf{v}_i = {}^{t-\Delta t/2}\mathbf{v}_i - 0.5\Delta t\gamma_{ij}\omega^D\left[{}^{t}\mathbf{n}_{ij}\cdot{}^{t-\Delta t/2}\mathbf{v}_{ij}\right]{}^{t}\mathbf{n}_{ij} + 0.5\sqrt{\Delta t}\sigma_{ij}\omega^R\varsigma_{ij}{}^{t}\mathbf{n}_{ij} \tag{80} $$

This takes into account the effect of stochastic forces from time $\left(t-\Delta t/2\right)$ to t. This is followed by integration from t to $\left(t+\Delta t/2\right)$ in which the effect of inter-particle forces, external forces, and artificial viscosity forces, ${}^{t}\mathbf{F}_i^C$, are taken into account and is given as

$$ \begin{aligned} {}^{t+\Delta t/2}\mathbf{v}_i = {}^{t}\mathbf{v}_i &+ 0.5\sqrt{\Delta t}\sigma_{ij}\omega^R\varsigma_{ij}{}^{t}\mathbf{n}_{ij} - 0.5\Delta t\gamma_{ij}\omega^D\left[{}^{t}\mathbf{n}_{ij}\cdot{}^{t}\mathbf{v}_{ij}\right]{}^{t}\mathbf{n}_{ij} \\ &- 0.5\Delta t\gamma_{ij}\omega^D\left[{}^{t}\mathbf{n}_{ij}\cdot\left\{\Delta t^{0.5}\sigma_{ij}\omega^R\varsigma_{ij}{}^{t}\mathbf{n}_{ij} - \Delta t\gamma_{ij}\omega^D\left({}^{t}\mathbf{n}_{ij}\cdot{}^{t}\mathbf{v}_{ij}\right){}^{t}\mathbf{n}_{ij}\right\}\right]{}^{t}\mathbf{n}_{ij} \\ &+ \Delta t\,{}^{t}\mathbf{F}_i^C/m_i \end{aligned} \tag{81} $$

Integration is carried out for $j > i$ and the negative of the stochastic incremental velocities are updated for particle j. In the scheme presented here, the deterministic integration for the update of velocities is carried out in one time step. From the velocities, which are updated for the full effect of stochastic as well as deterministic forces, the positions are updated as

$$ {}^{t+\Delta t}\mathbf{r}_i = {}^{t}\mathbf{r}_i + \Delta t\,{}^{t+\Delta t/2}\mathbf{v}_i \tag{82} $$

Because of the stochastic and random forces built into the formulation, careful numerical experimentation was needed to stabilize the integration scheme. Therefore, initial

simulations were setup to resolve issues with the numerical artifacts of the integration scheme and to obtain an optimum time step.

3.3 Continuum Quantities from Discrete Output of DPDE Method

DPDE is a particle methodology and the output obtained from the DPDE simulation is discrete by its very nature. The updated positions and momenta of the particles that are obtained by integrating the equations of motion need to be suitably averaged to obtain continuum quantities for comparison with experimental data. In this work, a specific particle is tracked in-situ and continuum quantities are obtained by averaging over a cuboidal averaging domain centered on the particle. The in-situ shocked average quantities are calculated in current coordinates using an extension of Hardy's methodology[101, 102]. The details of Hardy's averaging technique[101], comparison with Zimmerman's method[104] and details of Hardy's algorithm are given in Appendix A. The algorithm is briefly discussed below.

The mass density ρ, momentum density $\mathbf{p}$, local mass average velocity $\mathbf{u}$ and stresses $\boldsymbol{\sigma}$ are obtained by averaging the DPDE output over a parallelepiped volume of dimensions $2L_x \times 2L_y \times 2L_z$ centered on a specified particle and tracking its motion. The parallelepiped is centered on the tracked particle in the longitudinal direction and is concentric with the RVE in the lateral direction. The mass density ρ, the momentum density $\mathbf{p}$, the local mass average velocity $\mathbf{u}$ and the stress tensor $\boldsymbol{\sigma}_T$ are given by equation (83)to equation (86) respectively as

$$\rho(\mathbf{R},t) = \sum_i m_i \Delta\left({}^t\mathbf{r}_i - \mathbf{R}\right) \tag{83}$$

$$\mathbf{p}(\mathbf{R},t)=\sum_i m_i\,{}^t\mathbf{v}_i\Delta\left({}^t\mathbf{r}_i-\mathbf{R}\right) \tag{84}$$

$$\mathbf{u}=\frac{\mathbf{p}(\mathbf{R},t)}{\rho(\mathbf{R},t)} \tag{85}$$

$$\boldsymbol{\sigma}_T(\mathbf{R},t)=-\frac{1}{2}\sum_{i=1}^{N}\sum_{j\neq i}^{N}\mathbf{F}_{ij}^C\otimes{}^t\mathbf{r}_{ij}B({}^t\mathbf{r}_i,{}^t\mathbf{r}_j,\mathbf{R})-\sum_{i=1}^{N}m_i\,{}^t\mathbf{w}_i\otimes{}^t\mathbf{w}_i\Delta({}^t\mathbf{r}_i-\mathbf{R}) \tag{86}$$

Here, $\mathbf{R}$ is the current center of the averaging parallelepiped, ${}^t\mathbf{w}_i={}^t\mathbf{v}_i-\mathbf{u}$, m_i is the discretized mass lying inside the averaging domain, $\otimes$ denotes the tensor product of two vectors, Δ is the localization function, and $B\left({}^t\mathbf{r}_i,{}^t\mathbf{r}_j,\mathbf{R}\right)$ is the corresponding bond function[101].

The first term in equation (86) arises from the inter-particle interaction forces and is termed as the potential contribution to the stress tensor. The second term arises from the momentum transport associated with the particles entering or leaving the averaging domain, and is the kinetic contribution to stress tensor. Initially, when the particles are in their equilibrium positions, the potential contribution to stress tensor is negligible and the kinetic component is the main contributor to the stress tensor. However, once the steady state is reached, the relative velocity of particles in the averaging domain is close to zero. Because of compression, there are strong inter-particle repulsions between the particles in the averaging domain. In the steady state, the kinetic contribution is therefore negligible and the stress tensor is dominated by the potential contribution.

A 3D cosine function is used as a localization function in this work[108] and is given as

$$\Delta = \left[A\left(\frac{1}{2}\left(1+\cos\left(\frac{\pi x}{L_x}\right)\right)\right)\left(\frac{1}{2}\left(1+\cos\left(\frac{\pi y}{L_y}\right)\right)\right)\left(\frac{1}{2}\left(1+\cos\left(\frac{\pi z}{L_z}\right)\right)\right)\right]$$
$$\text{for } |x| \le L_x, |y| \le L_y, |z| \le L_y \qquad (87)$$
$$= 0, otherwise$$

The contribution of a specific particle to the continuum quantity at the field point, $\mathbf{R}$, needs to be statistically averaged in a consistent manner. This is because particles at different distances from the field point contribute differently to the field quantity at the location $\mathbf{R}$. The localization function serves to statistically weigh the contribution of a particle to the continuum quantity at the field point.

The bond function is defined as:

$$B\left({}^{t}\mathbf{r}_i, {}^{t}\mathbf{r}_j, \mathbf{R}\right) \equiv \int_0^1 \Delta\left(\tau\, {}^{t}\mathbf{r}_{ij} + {}^{t}\mathbf{r}_j - \mathbf{R}\right) d\tau \qquad (88)$$

and for two particles 'i' and 'j' with coordinates ${}^{t}\mathbf{r}_i$ and ${}^{t}\mathbf{r}_j$, is obtained by integrating the localization function along the line connecting the two particles[101]. The bond function weighs in a statistical manner the contribution of a pair of particles to the stress tensor at the field point $\mathbf{R}$. The detailed algorithm used for computing continuum averages based on equations (83) to equation (86) is presented in Appendix A.

To the best of our knowledge, this is the first time that Hardy's methodology has been extended and applied to obtain continuum quantities from discrete particle output at the mesoscale. It needs to be mentioned that Hardy's averaging method was developed and used for MD simulations. Particles in MD are point masses with infinitesimal size. Having developed from molecular length scale, DPD and DPDE methods also consider point mass particles with infinitesimal size. This is the reason that particle size does not appear in any equation or discussion presented here. Equation (83) to equation (86) will

yield converged in-situ averaged quantities for infinitesimally small particles. The present work keeps the core of DPDE formulation unchanged, and hence, is also independent of particle size. The particle size enters into the formulation through averaging equations (83) to (86)

The particle size independent DPDE is extended to the micron length scale by determining the number of particles from the representative volume element (RVE) size, particle arrangement and assumed inter-particle distance. The RVE mass is equally lumped to the particles. This makes the particle a point mass in this extended form of DPDE too. However, each particle needs to be associated with a finite size to preserve the mass continuity. For example, though not necessary, the natural selection is to choose a sphere of diameter equal to inter-particle distance to obtain close packing for the isotropic case. However, the calculation of m_i will depend on the mass-less space between spheres and overlapping of spheres in the deformed state. It should again be noted that the overlapping does not affect any force quantities of equation (68), which are calculated from the inter-particle distance and mass of particles. But, it will affect the in-situ averaged quantities calculated from equation (83) to equation (86). Two methods were developed to circumvent the resulting non-convergence:

a) For the averaging purpose, an average size (or diameter) was determined for each particle, from its distance from the neighbor, lying either inside the averaging domain or contributing mass inside the domain. Thus, the size varied from particle to particle and at each averaging instance. For this reason, the method will be referred to as the Dynamic Particle Size method while discussing the results.

b) A hexahedron was formed around each contributing particle. The vertices of the hexahedron lie at the center of hexahedrons formed with particle positions as vertices in the IJK ordered particle arrangement. The details of the hexahedron averaging are given in Appendix B.

One of the key parameters observed in shock experiments is the velocity profile at the free surface along with the peak value of the free surface velocity. From the theory of uniaxial shock propagation, the peak value of free surface velocity is equal to the impactor velocity for a symmetrical impact. For comparison with theory, the average value of the free surface velocity was obtained by constructing an averaging domain in the center of the free surface and averaging the velocities of all the particles inside this averaging domain. The size of the averaging domain was initially taken to be $10\mu m \times 10\mu m$ and to test the robustness of the approach and further validate the formulation, the size of the averaging domain was reduced to $4\mu m \times 4\mu m$.

CHAPTER 4

SIMULATION RESULTS AND DISCUSSION

The generic formulation of DPD and DPDE presented in the previous chapter was developed first as DPD and then extended to DPDE. The simulation results are presented first to validate the development at various stages followed by the simulations of shock response of RDX under an assumed planar parallel plate impact experiment.

4.1 DPD Validation with Equation-of-State of a DPD Fluid

The development of DPD method was validated by simulating a DPD fluid and deriving its equation-of-state[46] from the simulation. The simulation was performed in dimensionless units where the particle mass and energy were assigned a value of unity. The maximum interaction range for inter-particle interactions was assumed to be unity. The particles interacted via a soft conservative repulsive interaction that accounted for the chemical interaction between the particles, and the standard dissipative and random forces of the DPD formulation. The form of the conservative soft repulsive interaction used for DPD simulation is specified in equation (62). a is the repulsion parameter that controls the strength of soft repulsive interaction and a was taken to be[46] 25. The repulsive interaction has a sharp cutoff at the inter-particle distance of unity. The equations of motion were integrated using the modified velocity-Verlet scheme suggested by Groot and Warren[46] and given in equation (67). The DPD particles were point particles with no spatial extent and were initially distributed randomly inside the RVE. The time step of the simulation was taken to be 0.04 and the amplitude of the random

force was assumed to be 3.0. The virial pressure was computed as specified in equation (25)

$$p = \rho_n k_B T + \frac{1}{3V}\left\langle \sum_{j>i} \left({}^{t}\mathbf{r}_i - {}^{t}\mathbf{r}_j \right) \cdot \mathbf{F}_{ij}^{C} \right\rangle \tag{89}$$

The quantity $\left(p - \rho_n k_B T \right)$ is defined as the reduced pressure.

The RVE consisted of a cube of edge length 10 units in which 3000 DPD particles were placed at random. Periodic boundary conditions were imposed on RVE in all three directions so that a particle leaving the RVE from one wall of the RVE entered through the opposite wall. Figure 2 below shows the RVE with DPD particles randomly distributed in it.

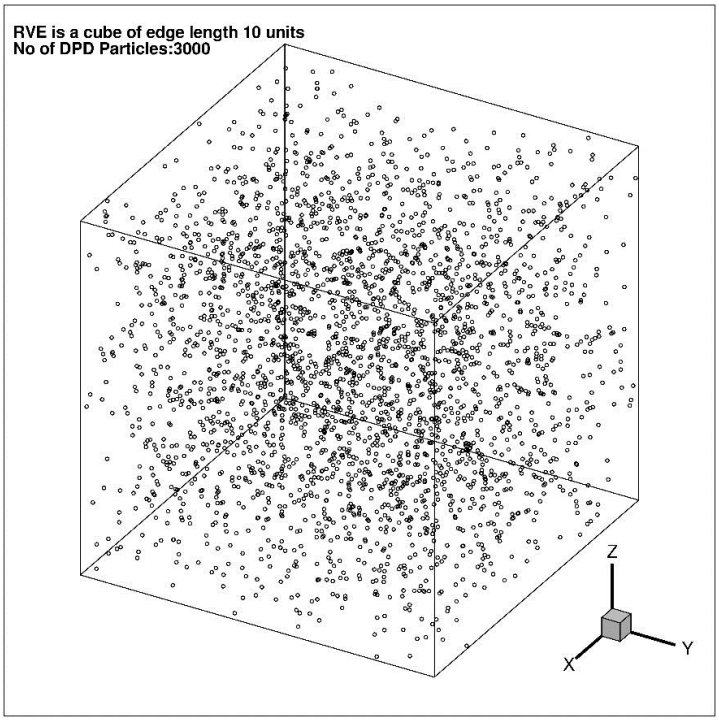

Figure 2 RVE for simulation of equation of state of a DPD fluid

Simulations were performed by varying the number of particles in the RVE from 3000 to 7000 in increments of 1000 particles. This corresponded to increasing the number density of particles in the RVE from three to seven in increments of unity. The reduced pressure normalized by the repulsion parameter a was computed for different values of number density ρ_n.

The simulation results are shown in figure 3 below along with the equation of state of the DPD fluid reported by Groot and Warren[46].

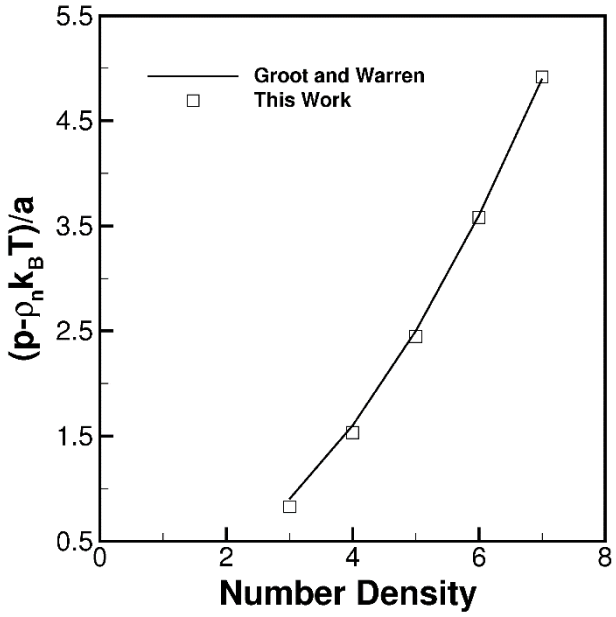

Figure 3 Reduced pressure normalized by interaction parameter, a, as a function of number density of DPD particles obtained from DPD simulations

The present simulation results agree well with the equation-of-state simulation result of Groot and Warren[46], given earlier in equation (26),

$$p - \rho_n k_B T = \delta a \rho_n^{\,2} \qquad (\delta = 0.101 \pm 0.001) \tag{90}$$

4.2 DPDE Validation with Simulation of an ideal gas

The DPDE development was first validated by simulating the equilibrium temperature attained in an ideal gas under imposed kinetic and internal energies. The ideal gas was modeled by setting the interaction parameter of the conservative force in the DPDE simulation to zero. The RVE was a cubic volume 10 units on an edge in which 6000 DPDE particles were initially placed at random. The system was initially provided a total energy of 375000 units equivalent to a temperature of 1 unit. Periodic boundary conditions were imposed on the simulation box in all three directions. Figure 4 below shows the RVE for the DPDE simulation of ideal gas

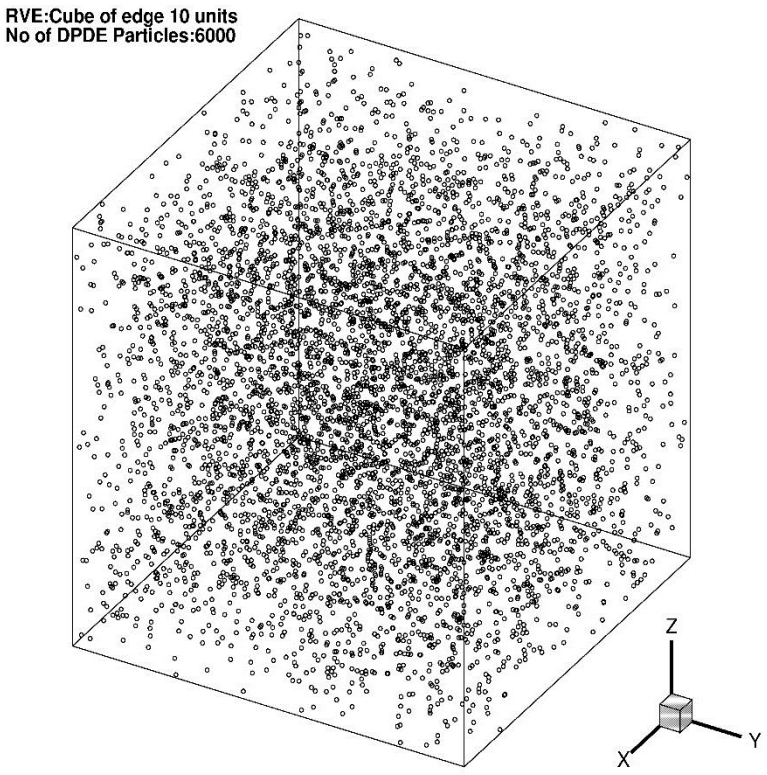

Figure 4 RVE for DPDE simulation of an ideal gas

The total energy of an ideal gas was the sum of internal energies of the DPDE particles and their kinetic energies. For an ideal gas, the total energy is a function of temperature only. Two cases were simulated.

In the first case, the DPDE particles were given an initial kinetic energy and assigned an initial meso-temperature value so that the kinetic temperature (KT) was greater than the theoretical equilibrium temperature (TT) and the meso- temperature (MT) was less than the equilibrium temperature. Figure 5 shows the evolution of the kinetic temperature and meso-temperature of the ideal gas for this case. It was observed that both the meso and the kinetic temperature evolved towards the theoretical equilibrium temperature demonstrating that particles exchanged energy as the ideal gas approached the equilibrium state.

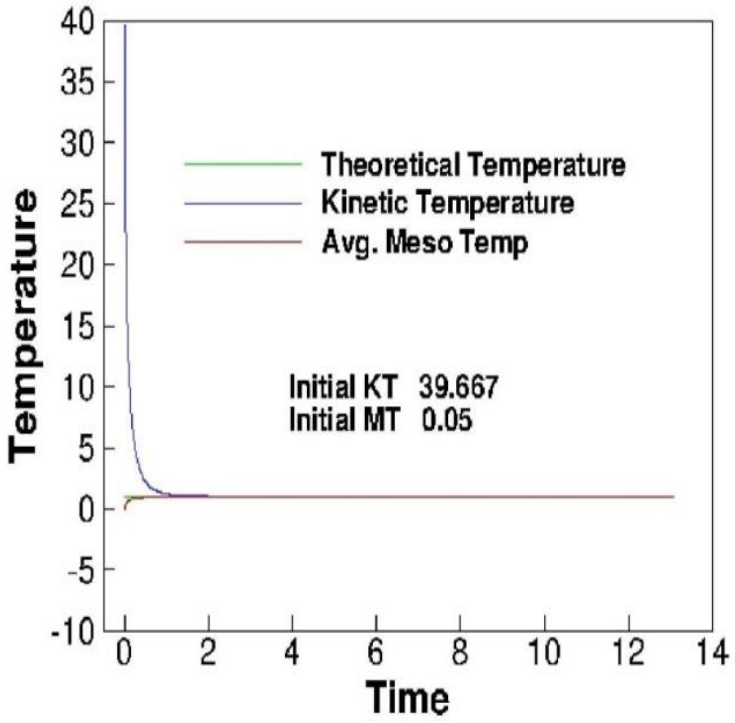

Figure 5 Approach to equilibrium of an ideal gas showing evolution of temperature (MT<TT<KT). The temperature and time are in arbitrary units

Figure 6 shows the evolution of the kinetic, internal and total energies for the same case. The kinetic energy decreased and the internal energy increased while the total energy remained constant. This correlates with the decrease in kinetic temperature and an increase in meso temperature as shown in figure 5. The energy was transferred from the kinetic to the internal energy of the meso particles.

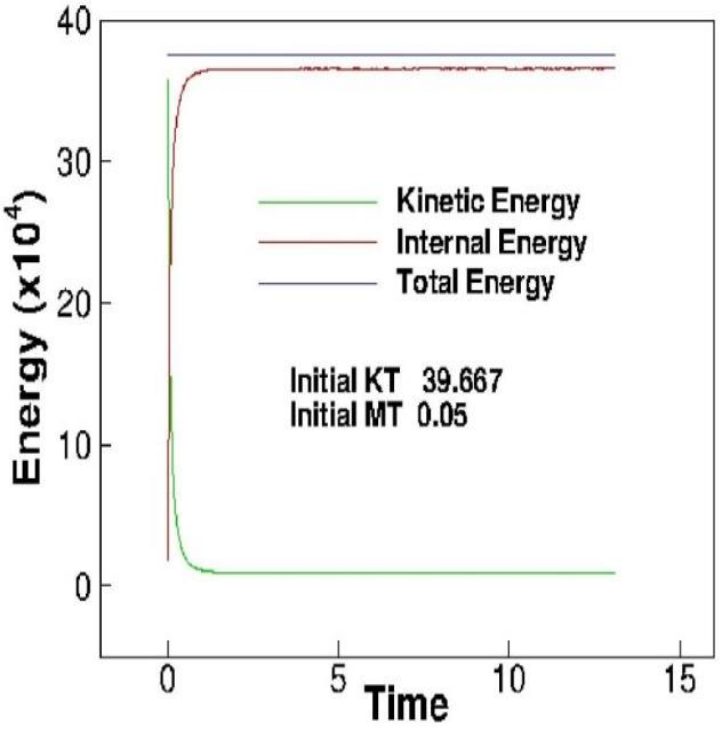

Figure 6 Approach to equilibrium of an ideal gas showing evolution of kinetic and internal energy (MT<TT<KT). The energy and time are in arbitrary units

In the second case, the DPDE particles were given an initial kinetic energy and assigned an initial meso-temperature value so that the kinetic temperature (KT) was lower than the theoretical equilibrium temperature (TT) and the initially assigned meso-temperature (MT) was greater than the equilibrium temperature. Figure 7 shows the

evolution of the kinetic and meso-temperature for the ideal gas for this case. Again, the system evolved to equilibrium with the meso-temperature decreasing and the kinetic temperature increasing until both converge to the theoretical equilibrium temperature.

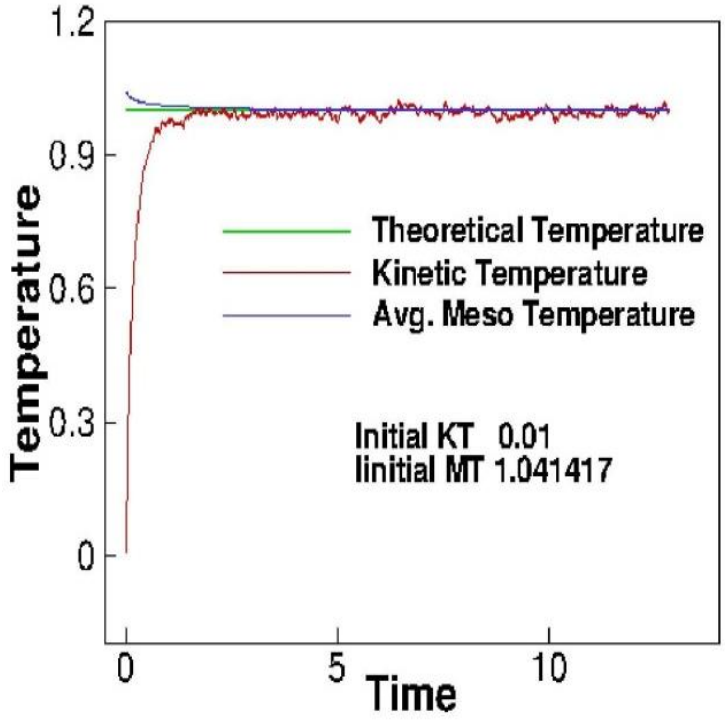

Figure 7 Approach to equilibrium of an ideal gas showing evolution of temperature (KT<TT<MT). The temperature and time are in arbitrary units.

Figure 8 shows the evolution of internal, kinetic and total energies for this case. The kinetic energy increased at the expense of the internal energy of the meso-particles which correlates with the increase in kinetic temperature at the expense of average meso temperature in Figure 7. The total energy remained constant demonstrating energy conservation in DPDE.

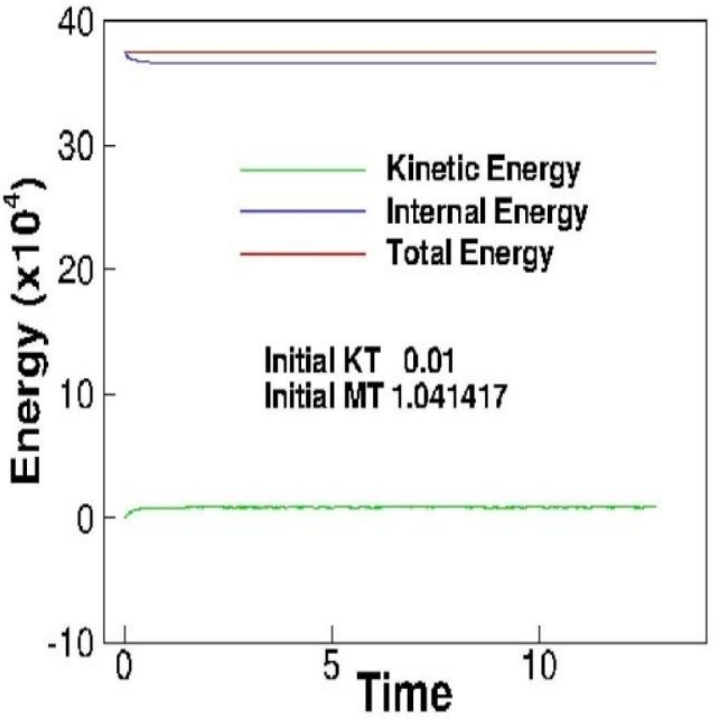

Figure 8 Approach to equilibrium of an ideal gas showing evolution of kinetic and internal energy (KT<TT<MT). The energy and time are in arbitrary units

4.3 DPDE Validation with One Dimensional Fourier Heat Flow in RDX

DPDE development was next validated by simulating one dimensional Fourier heat flow in a RVE of RDX with dimensions of $80\mu m \times 8\mu m \times 80\mu m$ as shown in figure 9 below.

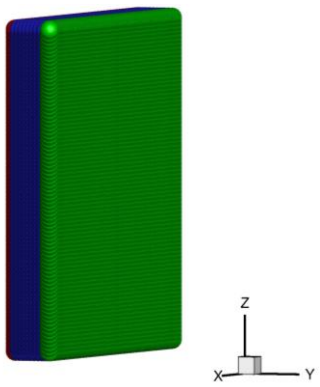

Figure 9 RVE for DPDE simulation of one dimensional Fourier heat flow in a slab of RDX sandwiched between two constant temperature walls.

The RVE was composed of $1.0\mu m$ diameter DPDE particles, yielding a total of 51200 RVE particles. The DPDE particles were representative of RDX in terms of physical and mechanical properties. The mass density, ρ, and specific heat, C_v, of RDX were obtained from Miller[109]. The particles interacted via inter-particle potential, dissipative, and random forces. The inter-particle potential force was of the Lennard-Jones form as specified in equation (69). The values of m and n parameters of the Lennard-Jones form of interaction were 2.0 and 4.0 respectively, adopted from Yano et al[4]. The material properties used in the simulation of Fourier heat flow are specified in table 1 below.

Table 1: Material parameters used in the simulation of 1D Fourier heat flow

ρ	C_v	α_{LJ}	$\sigma_{ij} = \sigma$	C_1	C_2
(kg/m^3)	($J/kg/^0K$)	(GPa)	($ms^{-1.5}$)	(kg/m/s)	(kg/m)
1820.0	1046.0	2.1964	$2.34x10^{-4}$	0.0	0.0

The initial temperature of the RVE particles was set at 300.0 K. The RVE was bounded by walls normal to the Y direction. The cold wall was maintained at a temperature of 297.0 K while the temperature of the hot wall was maintained at 303.0 K. Dissipative and random interactions allowed the particles to exchange energy leading to the change in the meso-temperature of the DPDE particles. The inter-particle potential force, a function of inter-particle spacing, played a very limited role in this simulation because the displacement of DPDE particles from their initial positions was minimal and random in nature.

For the simulation of Fourier heat flow, the fraction of potential energy dissipated as internal energy was set to zero so that the heat transport occurred solely by mesoscopic heat conduction. Simulations were run for different values of time step, Δt, and, parameter, κ_0, of equation (78). The simulations were used to obtain temperature vs. distance profiles at different times. The thermal diffusivity was determined from the simulation using the one dimensional form of the heat equation which is given as

$$\frac{\partial T}{\partial t} = \alpha \frac{\partial^2 T}{\partial x^2} \qquad (91)$$

,

where T, t and x are respectively the temperature, time and position respectively, and α is the thermal diffusivity.

To calculate the thermal diffusivity from the simulation, the first derivative of temperature with respect to time on the LHS and the second derivative of temperature with respect to position on the RHS of equation (91) were determined by curve fitting the temperature vs. time and temperature vs. position profiles respectively. For this purpose, the three dimensional simulation was first reduced to one dimensional case by

averaging the temperature and position of all particles lying in individual X-Z planes. This provided 8 values of temperature vs. position along the direction of heat flow, the Y-direction. The temperature vs. time and temperature vs. position profiles were fit by a cubic polynomial and their first and second derivatives were obtained by analytically differentiating the curve fit equation. The thermal diffusivity α was then obtained using equation (91). Numerical simulations showed that the temperature evolution converged to the same value irrespective of the time step Δt, provided $\Delta t \leq 1.4\times10^{-10}$ seconds. It was also observed that the time evolution of temperature profile was a strong function of the parameter κ_0, which determines the mesoscopic thermal conductivity of the material. The thermal diffusivity was computed for different values of parameter κ_0 and compared with experimental values. It was found that the value of $\kappa_0 = 0.152\times10^{-6}$ yielded a thermal diffusivity in reasonable agreement with the experiment[109] and therefore this value of parameter κ_0 was used for subsequent simulations of quasistatic compression and plate impact experiments.

Figure 10 shows the temperature as a function of time at the center (4.5μm) along heat propagation Y coordinate for a κ_0 parameter of 0.152×10^{-6} and cubic polynomial fit, using a time step of 1.423×10^{-10} seconds.

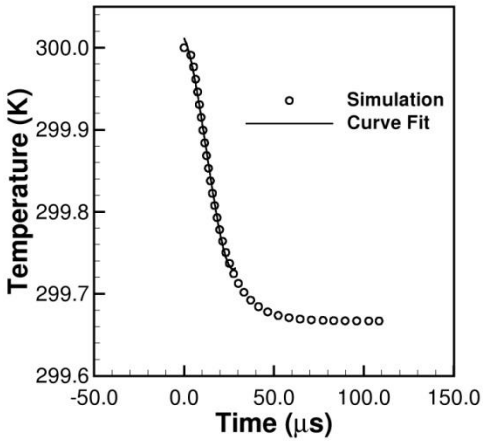

Figure 10 Temperature evolution as a function of time at the center (4.5μm) along heat propagation direction.

Figure 11 shows the corresponding temperature profiles as a function of position along the Y direction, the direction of heat flow, at different times.

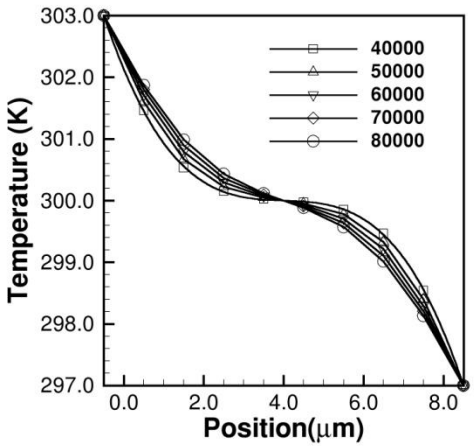

Figure 11 Temperature as a function of position at five different time steps

Table 2 shows the corresponding computed thermal diffusivities at different times, obtained from the present simulations.

Table 2: Computed Values of Thermal Diffusivity

Time Step No	$\alpha \times 10^{6}\ \ m^{2}s^{-1}$
40000	0.119
50000	0.148
60000	0.179
70000	0.210
80000	0.244

The simulated evolution of temperature with time was validated by comparison with an analytical solution. The analytical solution of the heat conduction equation (91) for an infinite solid plate of thickness l whose ends at $x = 0$ and $x = l$ are maintained at constant temperatures is given by[110]:

$$T(x,t) = T_H + (T_C - T_H)\frac{x}{l} + \left(\frac{2}{\pi} \sum_{n=1}^{\infty} \frac{T_C \cos(n\pi) - T_H}{n} \cdot \sin\left(\frac{n\pi x}{l} \right) \cdot \exp\left(\frac{-\alpha n^2 \pi^2 t}{l^2} \right) \right) - 2T_{in} \left(\sum_{n=1}^{\infty} \frac{\cos(n\pi) - 1}{n\pi} \cdot \sin\left(\frac{n\pi x}{l} \right) \cdot \exp\left(\frac{-\alpha n^2 \pi^2 t}{l^2} \right) \right) \quad (92)$$

where T_H is the temperature of hot end at $x = 0$ and T_C is the temperature of cold end at $x = l$. T_{in} is the initial temperature of the solid and α is the thermal diffusivity which is assumed to be a constant in this analytical solution.

The analytical solution was computed at the experimental value of α 0.108×10^{-6} m^2s^{-1} as well as the lowest and highest values of computed thermal diffusivity shown in the table 2 above i.e. 0.119×10^{-6} and 0.244×10^{-6} m^2s^{-1} respectively.

The temperature as a function of time in the RVE at the Y position of 4.5 μm, which was obtained from simulation, was compared with the analytical solution and the results are shown in figure 12.

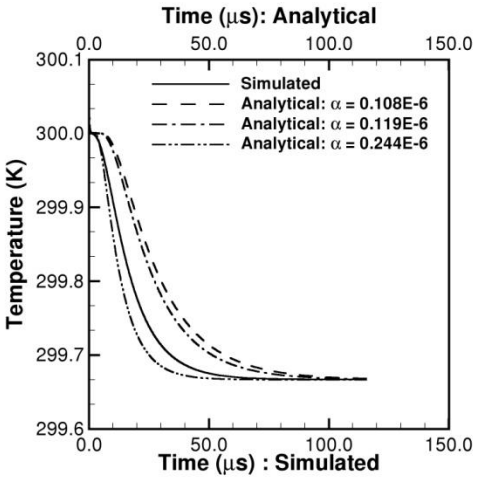

Figure 12 Comparison of analytical 1D Fourier profiles with simulated results.

The thermal diffusivity is a function of temperature in the DPDE formulation while the analytical solution considers constant thermal diffusivity. For this reason, analytical solutions were obtained at experimental values of thermal diffusivity at 295 K as well as the minimum and maximum values of thermal diffusivity obtained from 3D simulations. It was observed that as the thermal diffusivity increases, the system approaches the equilibrium temperature faster. Of the three values of thermal diffusivity used for computing the analytical solution, the experimentally-determined thermal diffusivity value is the lowest. Consequently, heat diffuses most sluggishly at the experimental value of thermal diffusivity. The simulated curve lies in between the two extreme values of diffusivity used for computing the analytical solution. Nevertheless, the value of κ_0 parameter obtained from this validation is used in all the simulations and serves an important validation and procedure proposed in this work.

4.4 DPDE Validation with Quasi-static Compression of RDX

The DPDE development was further validated with quasi-static compression of RDX. The simulated RVE was of dimensions $50\mu m \times 20\mu m \times 20\mu m$ and consisted of 20000 DPDE particles, each of diameter $1\mu m$. The particles were stacked in a simple cubic arrangement to form a rectangular block as shown in figure 13 below.

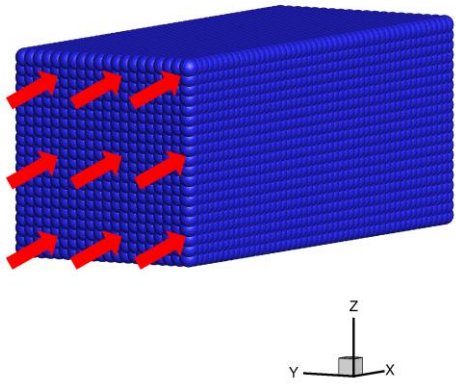

Figure 13 RVE for simulation of quasi-static compression of RDX slab.

The material parameters of RDX given in table 1 were used in the simulation with $\kappa_0 = 0.152 \times 10^{-6}$ as determined from validation with one dimensional Fourier heat conduction. The particles were representative of RDX in terms of physical and thermal properties.

The RVE was loaded quasi-statically along the X direction normal to the YZ plane at one end as shown in figure 13. A total force of 0.5 Newtons was applied gradually in N time steps uniformly distributed over all the particles of the loaded face. The number of time steps N over which the full load was applied on the loaded face was a function of the time step of the simulation. The opposite face, at the other end of the RVE, was held

fixed in place to simulate quasi-static compression. Following the application of full load of 0.5 Newtons in N time steps, the applied load on all of the particles of the loaded face was held constant during the duration of the simulation. The total applied load at time step n, where $n \le N$, on the loaded face was $\frac{0.5n}{N}$. The applied load on each of the 400 particles of the loaded face at time step n, where $n \le N$, was $\frac{0.5n}{400N}$.

For number of time steps n, where $n \ge N$, the total applied load on the loaded face was maintained at 0.5 Newtons and the applied load on each of the 400 particle of the loaded face was held constant at 1.25×10^{-3} Newtons. The maximum load of 0.5 Newtons on the loaded face of the RVE corresponded to an applied stress of 1.25 GPa. A specific particle in the middle of RVE was tracked for calculation of in-situ stress. The particles interacted via deterministic inter-particle potential forces and stochastic dissipative and random forces as specified in equation (69) and equation (63) respectively. For the simulation of quasi-static compression of RDX, the fraction of potential energy dissipated as internal energy was set to zero.

Simulations were also carried out by varying the value of parameter κ_0. It was observed that the evolution of in-situ average stress profile was independent of the value of parameter κ_0 showing negligible heat transport phenomenon during quasi-static compression of RDX. Simulations of quasi-static compression of RDX were performed for three different values of time step Δt as 1.423×10^{-10}, 1.423×10^{-11} and 1.423×10^{-12} seconds. The number of time steps in which full load was applied on the RVE, for three time steps mentioned above was so arranged that the full load was reached at the same

time for the three time steps at which the simulations were performed. This allowed the results for the three time steps to be compared.

Figure 14 shows the evolution of the axial xx component of the stress tensor as a function of time for three different time steps.

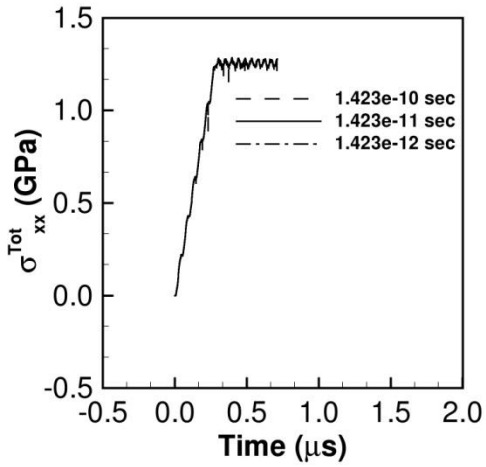

Figure 14 Time evolution of the axial xx component of in-situ stress for three different time steps used in the simulation

It is seen that for the three values of time steps considered in the present simulations, the computed in-situ average axial (xx) stress reached a steady state and oscillated between 1.23 GPa and 1.27 GPa, compared to the applied stress of 1.25 GPa. Further, the evolution of stress with time for the three time steps considered was almost indistinguishable. This demonstrated that the simulation converged to the same value, provided that the time step was less than 1.423×10^{-10} seconds. When the in-situ stress had reached a steady state, the strain in the RVE was computed as a fractional change in length of the RVE. From the computed steady state value of stress and strain, the Young's modulus of RDX was estimated using Hooke's law. This calculated value of Young's modulus was 16.20 GPa compared to the value of 19.29 GPa calculated from

reported values of the shear modulus and bulk modulus of RDX[111, 112]. The close agreement between the two values show that the DPDE extension to micron length scales and Hardy's averaging method predict the quasi-static compression of RDX with reasonable accuracy.

4.5 DPDE Simulation of RDX Plate Impact Experiment

DPDE method was finally used to simulate the shock response of RDX in a planar symmetrical plate impact experiment. Figure 15 (a) shows the schematic of the RVE used in the simulation.

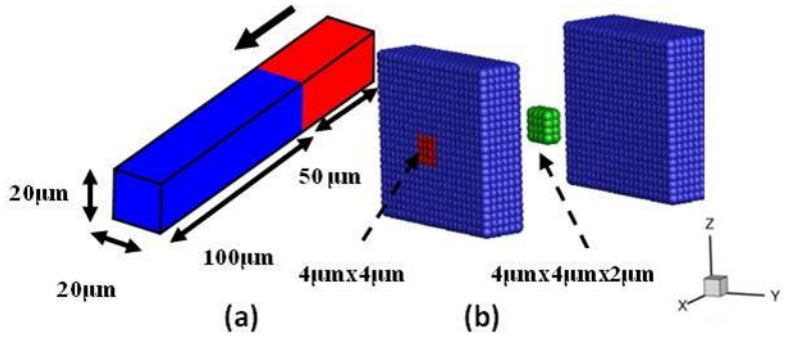

Figure 15 Schematic of (a) Simulation RVE for plate impact experiment and (b) Zoomed view of particle arrangement showing the averaging domain for calculation of free surface velocity (red) and in-situ average quantities (green).

Both the impactor and target plate were of uniform cross section, $20\mu m \times 20\mu m$ with the impactor plate of thickness $50\mu m$ impacting a stationary target plate $100\mu m$ thick. Both the impactor and target were composed of spherical particles $1\mu m$ in diameter stacked in a regular cubic arrangement with an equilibrium separation of $1.0\ \mu m$ between the particles. The micron sized particles constituting the impactor and target mirrored RDX

in physical and thermodynamic properties. The total mass of the RVE was lumped equally among all the particles. The interactions between the particles were modeled by the Lennard-Jones like form of potential force given in equation (69). Both the impactor and target were bounded by walls perpendicular to the Y- and Z- directions with lateral velocities of the particles forming the walls constrained to zero. The interaction between the impactor and target particles at the impactor-target interface was modeled using the inter-particle potential force making the two effectively a single body. Both the impactor and target particles were assigned an initial temperature of 300 K. The impactor particles were assigned a velocity as initial condition while the target particles were initially stationary. Simulations were carried out at two impactor velocities of 208 m/s and 876 m/s. These velocities corresponded respectively to the elastic particle velocity of 104 m/s and plastic particle velocity of 438 m/s for RDX in the experimental data of Hooks et al.[26] for shock propagation in the (100) direction. The averaged in-situ shock quantities were obtained by averaging over a cuboidal averaging domain of dimensions $4\mu m \times 4\mu m \times 2\mu m$ as shown in green in figure 15 (b). The averaging domain was centered with the cross-section of the RVE as it followed a tracked particle in the longitudinal direction. The free surface velocity was computed by averaging the longitudinal velocity of particles on the free surface of the target over an area of $10\mu m \times 10\mu m$ as well as $4\mu m \times 4\mu m$ centered on the free surface. The averaging domain for calculation of free surface velocity is shown in red in figure 15 (b).

The Lennard-Jones form of potential, equation (69), was used to model chemical interactions between the particles. Inter-particle interactions up to and including third nearest neighbors were considered in the simulations. The first nearest neighbors at

$1.0\mu m$ were along the edges of the cube, the second nearest neighbors at $2^{1/2}\mu m$ were along the face diagonals, and the third nearest neighbors at $3^{1/2}\mu m$ were along the body diagonals. Thus, the equilibrium separations along the edge, face diagonal and body diagonal were respectively $1.0\mu m, 2^{1/2}\mu m$ and $3^{1/2}\mu m$. At equilibrium separation, the inter-particle force between the DPDE particles was assumed to be zero. Reduction in inter-particle separation as a result of shock propagation leads to repulsive forces between particles preventing particle overlap. For each of the three neighbor types, the inter-particle interaction was cut off at a constant distance of $1.5\mu m$ beyond the equilibrium separation in tensile loading. The inter-particle potential parameter α was calculated for RDX based on the average value of Young's modulus of RDX of 19.29 GPa. In this work, three sets of (m,n) parameter values for the inter-particle potential, equation(69), were explored: $(2,4),(2,3)$ and $(1,2)$. Figure 16 shows the force as a function of position for the three pairs of (m,n) parameters of the Lennard-Jones potential used in this work

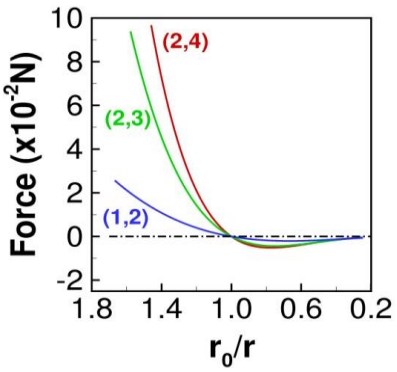

Figure 16 Force as a function of position for three pairs of (m,n) parameters of the Lennard-Jones interaction used in this work

The parameters of dissipative and random forces were adapted from Lisal et al.[49] based on numerical experimentation. The material properties used in the simulation are summarized in Table 1. Additional parameters, obtained from validation in this work or assumed, are given in Table 3 below.

Table 3: Parameters used in the simulation of plate impact experiment

κ_0	C_1	C_2
$\left(\text{msK}^2\right)^{-1}$	(kg/m/s)	(kg/m)
$0.152\text{x}10^{-6}$	3.931	$7.28\text{x}10^{-9}$

In the preliminary simulations of the plate impact experiment using DPDE method, numerical experimentation was first performed to solve tolerance and convergence issues and arrive at a time step that allowed convergence. The algorithm showed numerical instability to the values of computational tolerance used for computing interactions between the particles. The stochastic interactions between the particles were assumed to be zero at equilibrium separation and this prevented numerical instabilities from building and yielding non-physical results. Further, it was required that the projection of the relative velocity of the two particles along the line joining them should be less than a specific value. With this, the simulation was found to be free of numerical instability issues for the computational tolerance range used. The tolerance value used in the simulation results presented in this work was 10^{-5}. Similarly, it was found that the simulation was stable and converged consistently to the same values if the time step of the simulation was less than 1.423×10^{-10} seconds. All of the simulations for the plate impact experiment reported in this work utilized a time step of 1.423×10^{-11} seconds.

4.5.1 Simulated Free Surface Velocity Profiles

Figure 17 shows the free surface velocity profiles obtained from DPDE simulations at 208 m/s with and without artificial viscosity force of equation (70) for impactor velocity of 208 m/s.

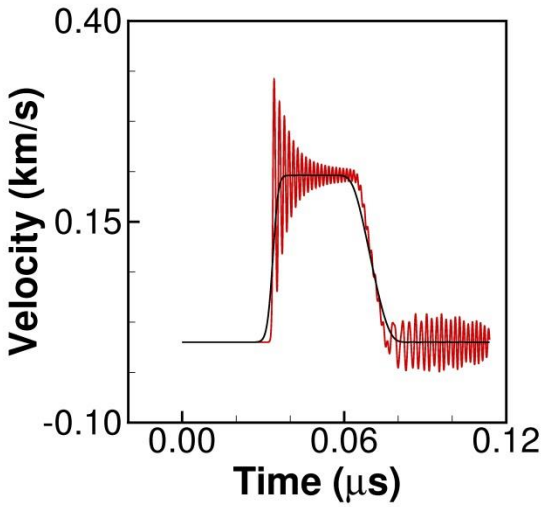

Figure 17 Free surface velocity profiles without (red) and with incorporation of artificial viscosity (black) in the plate impact simulation

The artificial viscosity term effectively damps out the numerical oscillations at the shock front to yield smooth shock wave profiles. Momentum and energy conservation continue to be retained with the introduction of artificial viscosity terms in DPDE. Similar results (not presented) were obtained for the 876 m/s impact velocity. The free surface velocity profiles from averaging over $10\mu m \times 10\mu m$ and $4\mu m \times 4\mu m$ domains were identical (not shown).

Figure 18 shows the free surface velocity profiles for the three sets of (m,n) parameters at two impact velocities.

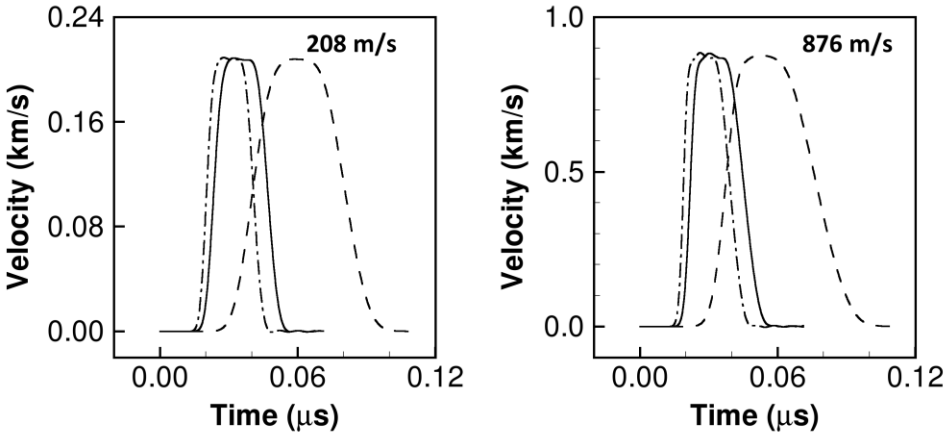

Figure 18 Free surface velocity profiles for 208 m/s impact (left) and 876 m/s impact (right) for three different sets of (m,n) parameters. Legend: (1,2) dashed; (2,3) solid; (2,4) dash-dot

The simulation predicted a steady state shock wave profile with a well-defined free surface peak velocity in agreement with uniaxial shock propagation theory. The peak value of free surface velocity was equal to the impactor velocity for the symmetrical impact. The particle velocity in the impactor and the target post impact was half of the impactor velocity as expected in a symmetrical impact. The peak velocity was independent of the values of (m,n) parameter used in the simulations. The time required for the free surface velocity to reach half its peak value was used to calculate the shock speed. The shock speed was dependent on the values of (m,n) parameters of the inter-particle potential and reduced as the inter-particle stiffness reduced from (2,4) to (1,2).

4.5.2 In-situ Average Mass Density from DPDE Simulations

As mentioned earlier, the core feature of particle size independence of DPDE has been preserved while extending to micron length scale in this work. The particle size enters into the formulation through the averaging method used to extract in-situ

parameters. Simulations were carried out at 208 m/s and in-situ mass density was obtained from equation (83) using the three methods discussed earlier, namely (a) constant particle size, (b) dynamic particle size, and (c) hexahedron averaging. In addition to 1.0 μm diameter spherical particles at 1.0 μm inter-particle distance, two more configurations were used in the simulations, namely, 0.5 μm diameter particles at 1.0 μm and 0.5 μm particles at 0.5 μm inter-particle distance. Figure 19 shows the in-situ mass density for the three methods of averaging.

Figure 19 (a) shows that the mass densities based on constant particle size do not converge. This is because Hardy's methodology[101] for mass averaging was originally developed for point particles. It does not take into consideration the void space in the packing of micron sized spherical particles.

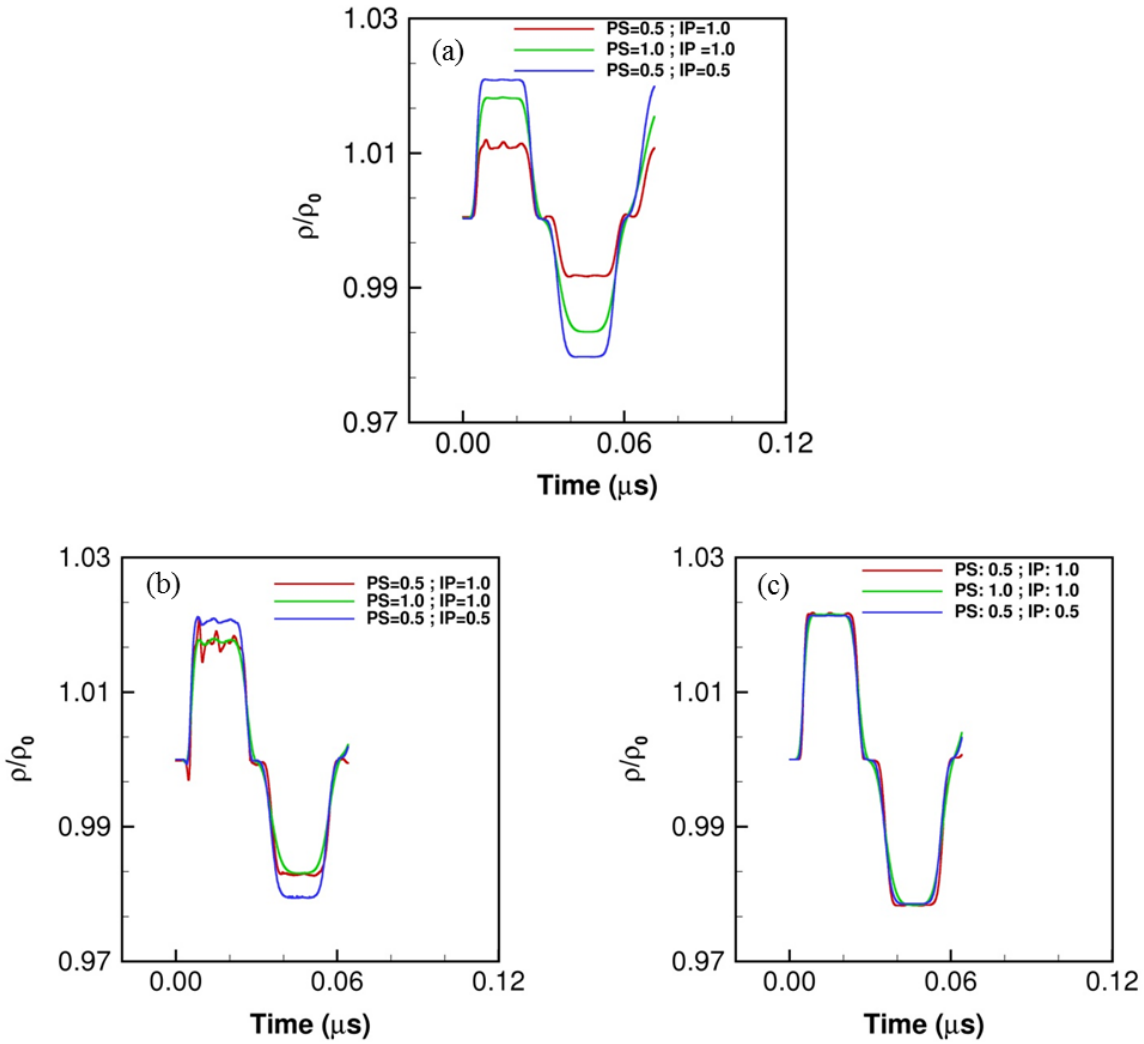

Figure 19 Simulated in-situ mass densities for three particle configurations using Hardy's method for (a) constant particle size (b) dynamic particle size (c) hexahedron averaging developed in this work.

Figure 19 (b) shows the mass averaging using dynamic particle size approach. The dynamic particle size approach is an improvement over the constant particle size method but the convergence for the three configurations is not obtained. Figure 19 (c) shows the convergence in mass density using the hexahedron approach in the formulation for the three configurations. It is clear that the shocked mass densities converge to the same

value independent of particle size and inter-particle spacing when mass averaging is based on the hexahedron approach. The mass averages reported in this work are based on hexahedron averaging.

Figure 20 shows the in-situ mass density for the two impact velocities.

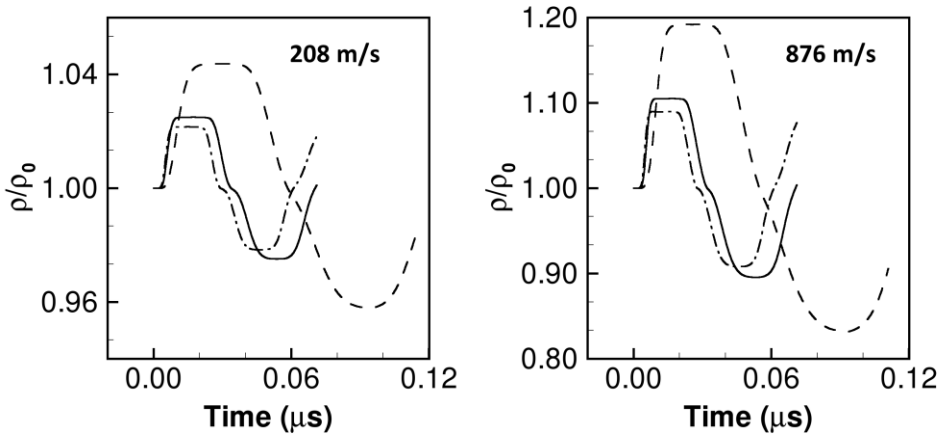

Figure 20 Mass density profiles for 208 m/s impact (left) and 876 m/s impact (right) for three different sets of (m,n) parameters. Legend: (1,2) dashed; (2,3) solid; (2,4) dash-dot

The normalized mass densities clearly show the effect of shock in changing the density of the material as it passes through the RVE. The change in mass density increases as the inter-particle stiffness is reduced from (2, 4) to (2, 1) for a given impact velocity. The in-situ mass density profiles show a well-defined constant peak value. The arrival of the release wave causes the material to decompress thereby reducing the density. Increase in impact velocity increases shock compression for the same values of (m, n) parameters, thus increasing the in-situ mass density seen at 876.0 m/s.

4.5.3 In-situ Longitudinal and Lateral Stress Profiles from DPDE Simulations

Figure 21 shows the in-situ longitudinal stress profiles for the two impact velocities and figure 22 shows the corresponding in-situ lateral stress profiles for the three sets of (m,n) parameters.

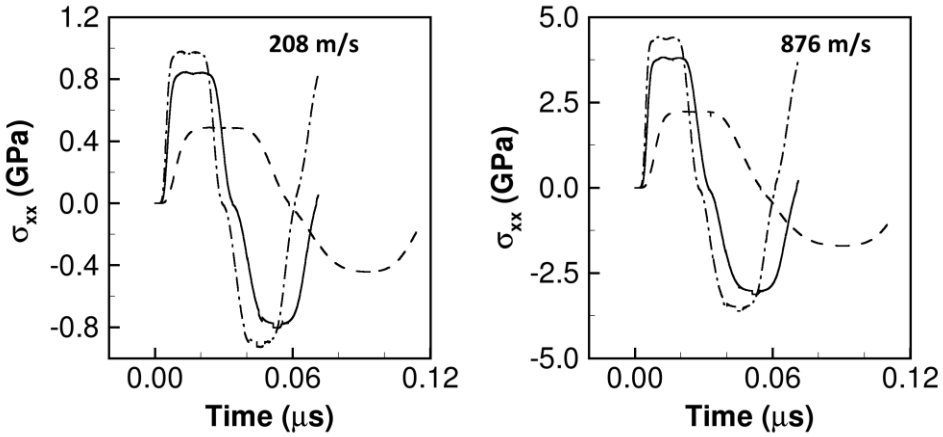

Figure 21 Longitudinal stress profiles for 208 m/s impact (left) and 876 m/s impact (right) for three different sets of (m,n) parameters. Legend: (1,2) dashed; (2,3) solid; (2,4) dash-dot

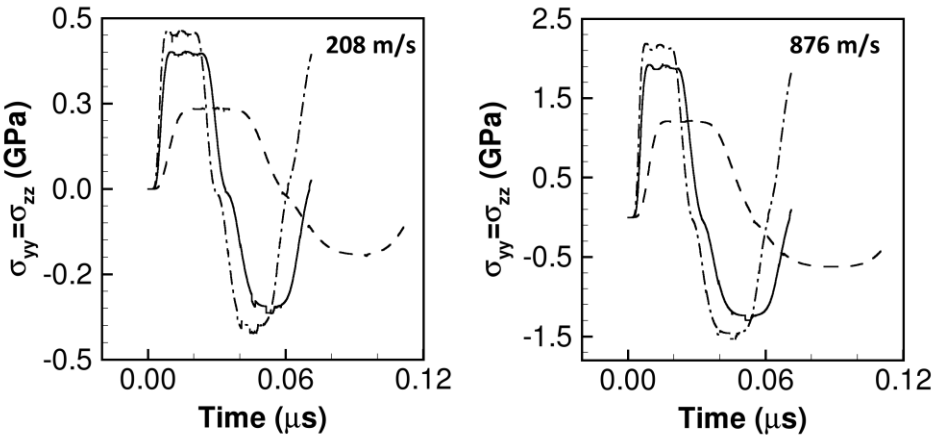

Figure 22 Lateral stress profiles for 208 m/s impact (left) and 876 m/s impact (right) for three different sets of (m,n) parameters. Legend: (1,2) dashed; (2,3) solid; (2,4) dash-dot

The particle size and inter-particle distance were 1.0 μm in these simulations. Both the longitudinal and lateral stress profiles show a well-defined peak stress. The two lateral stresses in the *yy* and zz directions were identical since the particle arrangement has a cubic symmetry and the potential is isotropic. The peak value of lateral stress is approximately equal to half the peak value of the longitudinal stress. The simulation clearly shows a rise to a peak value and then unloading as a result of the arrival of the release wave. The peak values of stresses correlate with the stiffness of the inter-particle potential, i.e. the values of the (m,n) parameters of the Lennard-Jones interaction. Following Yano[4] et al., the Young's modulus for a material in which inter-particle interactions are modeled using Lennard-Jones form of potential[4] as given by equation (69), is proportional to the product of m and n parameters. Therefore (2,4) is more stiff then (2,3) which in turn is stiffer than (1,2). Consequently, for the same displacement, the stress in (2,4) is highest, followed by (2,3) and then (1,2). This is consistent with the opposite trend that is observed in shocked mass densities as shown by figure 20. The most compliant (1,2) shows the highest shocked density followed by (2,3) and then (2,4).

The longitudinal and lateral stresses were nearly identical to those presented in figures 21 and figure 22 respectively for two other configurations namely, 0.5 μm particles at 1.0 μm and 0.5 μm particles at 0.5 μm inter-particle distance and hence have not been shown. Shear stresses, also computed in the simulation, were three to four orders of magnitudes smaller than the normal stresses, oscillatory in nature and have not been shown here. The in-situ mass density and stress profiles show that the simulation at present does not predict the elastic-inelastic shock wave propagation. This is because the

Lennard-Jones form of potential used to model inter-particle interactions in this work is purely elastic in nature.

4.5.4 Temperature Profile from DPDE Simulations

Figure 23 shows the temperature profiles obtained from the simulations for the two impact velocities.

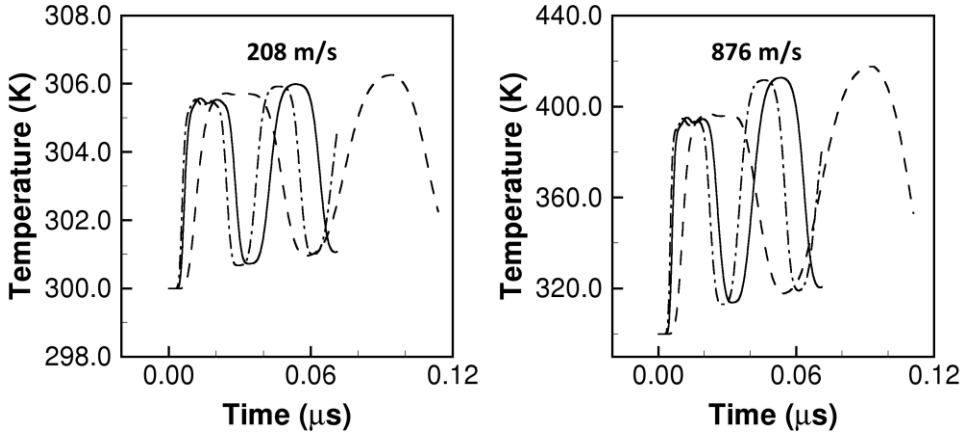

Figure 23 Temperature evolution profiles for 208 m/s impact (left) and 876 m/s impact (right) for three different values of (m,n) parameter. Legend: (1,2) dashed; (2,3) solid; (2,4) dash-dot

Since the inter-particle potential used in the simulation at this stage does not incorporate inelasticity, the temperature rise is obtained by dissipating 90 percent of potential energy as internal energy. The arrival of shock wave is accompanied by a rise in temperature. Since the temperature rise in the simulation is obtained by dissipating a fraction of potential energy as internal energy and because the potential is elastic, the potential energy oscillates reversibly between the extremes of compressed and tensile positions. Consequently, the arrival of the release wave, which results in decompression, reduces

the temperature. As expected, the 876 m/s impact velocity shows a higher temperature rise compared to the 208 m/s impact.

Table 4 summarizes the in-situ shock parameters obtained in the plate impact experiment at two impact velocities.

Table 4: Shock parameters for RDX obtained from DPDE simulations of plate impact experiment

(u_p – particle velocity U – shock velocity)

Impact Velocity (m/s)	m	n	u_p (m/s)	U (m/s)	σ_{xx} (GPa)	σ_{yy} (GPa)	T (^{0}K)
208.0	2	4	105.9	4944.9	0.97	0.45	305.4
	2	3	105.7	4285.2	0.84	0.40	305.5
	1	2	104.2	2494.1	0.49	0.24	305.7
876.0	2	4	446.6	5305.0	4.42	2.11	392.1
	2	3	445.2	4595.9	3.82	1.91	393.7
	1	2	441.1	2704.2	2.23	1.20	396.9

The DPDE method predicts in-situ shock response in qualitative agreement with the uniaxial shock wave propagation theory. The peak longitudinal stress for the (2,3) parameters at 208 m/s impact velocity was 0.84 GPa compared to 0.81 GPa reported in literature[26]. For 876 m/s impact velocity, the longitudinal stress obtained in the simulation was 3.82 GPa as compared to 2.92 GPa, reported in literature[26].

CHAPTER 5

CONCLUSIONS

The extension of DPDE method to micron and sub-micron length scale presented here is generic and can be applied to any physical situation by incorporating appropriate material properties and relevant initial and boundary conditions. The formulation can be applied to different materials by adopting an appropriate inter-particle potential and an equation of state relating the meso temperature to the internal energy for the material of interest. Although, in this work, the external force is assumed to be zero, the effect of interactions with the environment can be incorporated by using an appropriate form for the external force in the formulation. The formulation for averaging discrete particle quantities to obtain in-situ averaged continuum properties is also general and can be applied to DPDE particles of any size irrespective of the specific material properties of the particles.

Due to the lack of any existing source code, the entire development was carried out in-house in stages- DPD followed by extension to DPDE. The development was validated at various stages with equation-of-state for DPD fluid, equilibrium temperature in ideal gas, 1D Fourier heat transport, and quasi-static compression of an RDX sample. The present simulations yielded results in good agreement with analytical results and simulation results available in literature. Moreover, to the best of our knowledge, the DPDE method was applied for the first time to model the 1D Fourier heat flow and quasi-static compression of solid RDX under a distributed load. These simulations serve to

explore and demonstrate the potential of DPDE methodology as a generic mechanics simulation tool. For the Fourier heat flow problem, a steady state temperature profile was obtained in close agreement with the analytical results. The simulation also demonstrated a methodology for obtaining the κ_0 input parameter for DPDE based meso-scale simulations. From the DPDE simulation of quasi-static compression of RDX under distributed load, a value of Young's modulus of RDX was obtained in qualitative agreement with the value of Young's modulus of RDX obtained from literature.

To the best of our knowledge, DPDE methodology was successfully extended to micron and sub-micron length scales for the first time and applied to simulate the symmetrical plate impact experiment of an RDX flyer plate impacting a stationary RDX target. The simulation results were in agreement with the uniaxial shock propagation theory. The inter-particle interactions were modeled by a Lennard-Jones form of potential that included up to third nearest neighbor interactions. Three different sets of (m, n) parameter values for the Lennard-Jones interaction were considered representing reducing stiffness of RDX. The in-situ mass density decreased with increasing stiffness of the inter-particle potential. The free surface velocities, mass density and longitudinal and lateral components of the stress tensor showed a smooth rise to a well-defined peak value as expected from the uniaxial shock wave propagation theory. For the impact velocity of 208 m/s, (m=2, n=3), DPDE simulation yielded peak values of longitudinal stress in close agreement with the literature. The RDX response at 208 m/s impact velocity was elastic, as per the literature data, and was modeled adequately by the reversible Lennard-Jones form of potential used in this work. The Lennard-Jones form of potential does not incorporate inelasticity. Employing an assumption which lacks

justification at this stage, a fraction of potential energy was dissipated as internal energy to model heat generation testing the heat transport capabilities of DPDE under shock loading. Hence, the temperature calculation in this work is to be treated as a model calculation. Due to the absence of inelasticity, the present simulation did not predict the two wave structure at 876 m/s shown by data in literature[26]. The longitudinal stresses at the two impact velocities obtained using 3D averaging are in qualitative agreement with the literature values. Since the 876 m/s impact generates an elastic and plastic wave structure while the inter-particle potential does not incorporate inelasticity, the agreement of 876 m/s impact velocity simulation results with the experimental values is not as close as for the 208 m/s impact.

Artificial viscosity forces were incorporated in the DPDE formulation for the first time, with linear and quadratic artificial viscosity successfully damping the oscillations in the free surface velocity profile. Such oscillations and oscillations due to numerical tolerance become contentious issues in statistical methods of simulations of shock propagation. The present method effectively tries to sidestep these issues and focus on the statistical approach of inter-particle interactions through dissipative and random forces.

The Hardy's averaging methodology was extended for the first time to obtain continuum shock parameters from the discrete output of the DPDE method at micron and submicron length scales. Hardy's methodology was originally developed for point sized particles which will converge to the infinitesimal sized particles used in MD and other methods at molecular length scales. The present DPDE extension to micron length scale is particle size independent but revealed non-convergence of in-situ mass density due to spaces between particles even in the closest packing. To remedy the issue of non-

convergence of mass density with the change in particle size and inter-particle distance in the packing of micron and sub-micron sized spheres, an approach based on hexahedron averaging, to obtain averaged mass density, was developed. This resulted in the convergence of mass density to the same value irrespective of the particle size and inter-particle distance used to model the impactor and target.

It is finally concluded that DPDE method, developed and used at molecular length scale, has been successfully extended as a generic simulation tool exploiting its in-built heat transport characteristics which does not require a separate solution for heat conduction.

CHAPTER 6

FUTURE WORK

This work is the first successful attempt to extend and apply DPDE method to simulate solid materials at micron length scales. DPDE methodology was validated by mesoscale simulation of Fourier heat flow and quasi-static compression of solid HE materials under distributed loads. DPDE methodology was also extended for the first time to simulate shock response of solid HE materials at micron length scales. Since DPDE is a relatively recent simulation technique and has never been applied earlier at micron length scales, the full potential of this method still needs to be explored. Based on the ongoing work at the time of writing this thesis, some pressing future work can be listed as follows.

1. Development of a contact algorithm to model interaction between impactor and target at particle length scale: The interactions between the impactor and target particles at the impactor-target interface was modeled by a Lennard-Jones form of inter-particle forces, making impactor and target effectively one contiguous block. The interaction at the two body contact interface is primarily governed by the impenetrability condition and friction not modeled by the Lennard-Jones potential used in this work.
2. Development of inter-particle potentials at mesoscale incorporating inelasticity: In the absence of inelasticity in the inter-particle potential, the two wave structure was not predicted and the meso-temperature rise was obtained by dissipating a certain fraction of potential energy as internal energy. The incorporation of inelasticity in the inter-

particle potential to simulate the two wave structure and obtain a temperature rise from the inelasticity inbuilt into the potential would be an important component of future work.

3. Incorporating anisotropy: Coupled with the need for potentials at mesoscale is the ability to simulate the anisotropic response of RDX. The initial framework was developed and preliminary simulations were carried out to predict anisotropic response of RDX under shock loading keeping the Lennard-Jones form of inter-particle potential. The preliminary results were encouraging but not presented. However, an intrinsically anisotropic potential that incorporates angular dependence would be needed to fully describe the anisotropic response of RDX.
4. Incorporation of large scale heterogeneities in DPDE: Being a particle method, DPDE is intrinsically well suited to model large scale discontinuities and heterogeneities in the material. Still, the shock response of RDX based PBX upto the point where the reaction in the explosive is initiated would require the development of general methodologies to incorporate large scale deformations and fracture in the DPDE formulation itself. This would be a major milestone in the development of DPDE as a generic formulation for modeling multiphase, heterogeneous HE materials.

APPENDIX A

AVERAGING ALGORITHM

The output obtained from a particle method like MD, DPD, or DPDE are the positions, velocities and forces acting on each of the particles. This output by its very nature is discrete. We now present the details of obtaining continuum field quantities from discrete particle output based on Hardy's work[101]. That is, from the information on particle positions, velocities, and forces obtained in a particle method, we want to obtain continuum fields such as mass density, momentum density, energy density, heat flux and stress.

Hardy's approach[101] relies on constructing an averaging domain around a point where the continuum field quantities are desired and then averaging over the particles contained within this averaging domain. The contribution of a particle inside the averaging domain to the field quantity is taken statistically into account through the localization function[101]. The localization function is generally taken to be a smooth function that vanishes outside of the averaging domain and is normalized so that its integral over the entire simulation system is unity[101]. In three dimensions, the localization function has the dimensions of inverse volume. In Hardy's original work[101], this approach is illustrated by a one dimensional localization function that has the form of a top hat function[101]. Other localization functions such as cosine functions can be used as well[102]. The bond function is the integral of a localization function along the line connecting two

particles. In one dimension, the bond function has a simple interpretation as a fraction of the line connecting two particles that lies within the averaging domain[101]. The bond function for a pair of particles 'i' and 'j' with position vectors ${}^t\mathbf{r}_i$ and ${}^t\mathbf{r}_j$ respectively, is defined as

$$B\left({}^t\mathbf{r}_i, {}^t\mathbf{r}_j, \mathbf{R}\right) \equiv \int_0^1 \Delta\left(\tau\, {}^t\mathbf{r}_{ij} + {}^t\mathbf{r}_j - \mathbf{R}\right) d\tau \tag{93}$$

Here, $\mathbf{R}$ is the position where the field quantity is desired and τ is a variable of integration that takes values from 0 to 1. The quantity Δ is the localization function. In Hardy's original work[101], the localization function is taken to be

$$\begin{aligned} \Delta_{1D}\left({}^t\mathbf{r}_i - \mathbf{R}\right) = & \frac{1}{Al}\left(\text{if } X - \frac{1}{2}l < x_i < X + \frac{1}{2}l\right) \\ = & \ 0 \text{ otherwise} \end{aligned} \tag{94}$$

Here, l is the length of averaging domain and A is the area of averaging domain. The volume of the averaging domain is, therefore, Al. X and x_i are respectively the X coordinates of the center of averaging domain and the particle 'i'. Other localization functions can be used as well. The cosine localization function is given as[102]

$$\Delta_1\left(x\right) = \frac{1}{AW}\left\{\begin{array}{c} 0.5\left[1 + \cos\left(\dfrac{\pi x}{W}\right)\right], if\ |x| \le W \\ 0, \qquad \text{otherwise} \end{array}\right\} \tag{95}$$

Here, $2W$ is the width of averaging domain of area A and x is the distance from the center of the averaging domain. The mass, momentum and energy densities are given in terms of localization function Δ as

$$\rho(\mathbf{R},t)=\sum_i m_i\Delta\left({}^t\mathbf{r}_i-\mathbf{R}\right) \tag{96}$$

$$\mathbf{p}\left(\mathbf{R},t\right)=\sum_i m_i\,{}^t\mathbf{v}_i\Delta\left({}^t\mathbf{r}_i-\mathbf{R}\right) \tag{97}$$

$$E^0\left(\mathbf{R},t\right)=\sum_i\left[\frac{1}{2}m_i\left|{}^t\mathbf{v}_i\right|^2+\frac{1}{2}\sum_j\phi_{ij}\right]\Delta\left({}^t\mathbf{r}_i-\mathbf{R}\right) \tag{98}$$

Here, $\rho(\mathbf{R},t)$ and $\mathbf{p}\left(\mathbf{R},t\right)$ are respectively the mass and momentum density at the position $\mathbf{R}$ at time t as defined in equation (83) and equation (84) respectively. $E^0\left(\mathbf{R},t\right)$ is the energy density at the position $\mathbf{R}$ at time t. ϕ_{ij} is the potential from which the forces acting on the particles are derived.

The detailed derivations of the Hardy's[101] equations for averaging are now presented.

$${}^t\mathbf{v}_i\equiv\left({}^t\mathbf{v}_i-\mathbf{u}\right)+\mathbf{u} \tag{99}$$

$$\left({}^t\mathbf{v}_i-\mathbf{u}+\mathbf{u}\right)^2\equiv\left({}^t\mathbf{v}_i-\mathbf{u}\right)^2+\left|\mathbf{u}\right|^2+2\left({}^t\mathbf{v}_i-\mathbf{u}\right)\cdot\mathbf{u} \tag{100}$$

It follows from identity (100) that

$$\left({}^t\mathbf{v}_i\right)^2=\left({}^t\mathbf{v}_i-\mathbf{u}\right)^2+\left|\mathbf{u}\right|^2+2\left({}^t\mathbf{v}_i-\mathbf{u}\right)\cdot\mathbf{u} \tag{101}$$

The net force on the particle is related to the acceleration, ${}^t\mathbf{a}_i$, by Newton's second law as

$$m_i\,{}^t\mathbf{a}_i=\sum_j\mathbf{F}_{ij}={}^t\mathbf{f}_i \tag{102}$$

Newton's third law gives

$$\mathbf{F}_{ij} = -\mathbf{F}_{ji} \tag{103}$$

$\mathbf{F}_{ij}$ is the force on particle 'i' due to particle 'j'. $\mathbf{F}_{ij}$ can include conservative as well as non-conservative forces as in equation (68). $\mathbf{u}$ is the local mass averaged velocity as defined in equation (85).

Consider the function $\dfrac{\partial\Delta\left(\tau\,{}^{t}\mathbf{r}_{ij} + {}^{t}\mathbf{r}_{j} - \mathbf{R}\right)}{\partial\tau}$, where τ varies from 0 to 1. Let $\tau\,{}^{t}\mathbf{r}_{ij} + {}^{t}\mathbf{r}_{j} - \mathbf{R} = \mathbf{Y}$. Using chain rule,

$$\frac{\partial\Delta(\mathbf{Y})}{\partial\tau} = \frac{\partial\Delta(\mathbf{Y})}{\partial\mathbf{Y}}\cdot\frac{\partial\mathbf{Y}}{\partial\tau} = {}^{t}\mathbf{r}_{ij}\cdot\frac{\partial\Delta(\mathbf{Y})}{\partial\mathbf{Y}} = {}^{t}\mathbf{r}_{ij}\cdot\left(\frac{\partial\Delta(\mathbf{Y})}{\partial\mathbf{R}}\right) \tag{104}$$

Integrating equation (104) in the limit $\tau = 0$ to $\tau = 1$

$$\Delta(\mathbf{Y})\big|_{\tau=1} - \Delta(\mathbf{Y})\big|_{\tau=0} = {}^{t}\mathbf{r}_{ij}\cdot\int_{0}^{1} -\nabla_{\mathbf{R}}\left(\Delta\left(\tau\,{}^{t}\mathbf{r}_{ij} + {}^{t}\mathbf{r}_{j} - \mathbf{R}\right)\right)d\tau \tag{105}$$

Substituting for $\mathbf{Y}$, equation (105) gives

$$\Delta\left({}^{t}\mathbf{r}_{i} - \mathbf{R}\right) - \Delta\left({}^{t}\mathbf{r}_{j} - \mathbf{R}\right) = -{}^{t}\mathbf{r}_{ij}\cdot\nabla_{\mathbf{R}}\int_{0}^{1}\Delta\left(\tau\,{}^{t}\mathbf{r}_{ij} + {}^{t}\mathbf{r}_{j} - \mathbf{R}\right)d\tau \tag{106}$$

where the integration w.r.t. to variable τ and the nabla operator are independent operations. The integral on the RHS of equation (106) is the defined as the bond function

$$B\left({}^{t}\mathbf{r}_{i}, {}^{t}\mathbf{r}_{j}, \mathbf{R}\right) \equiv \int_{0}^{1}\Delta\left(\tau\,{}^{t}\mathbf{r}_{ij} + {}^{t}\mathbf{r}_{j} - \mathbf{R}\right)d\tau \tag{107}$$

For averaging, the force $\mathbf{F}_{ij}$ is assumed to be derivable from the potential ϕ_{ij} and is given by

$$\mathbf{F}_{ij}^{C} = -\nabla_i \phi_{ij}\left(\left|{}^{t}\mathbf{r}_{ij}\right|\right) \tag{108}$$

where $\left|{}^{t}\mathbf{r}_{ij}\right|$ is the distance between the particles 'i' and 'j'. Equation (108) can be written as

$$\mathbf{F}_{ij} = -\nabla_i \phi_{ij}\left(\left|{}^{t}\mathbf{r}_{ij}\right|\right) = -\phi_{ij}{}'\left(\left|{}^{t}\mathbf{r}_{ij}\right|\right).\left(\frac{{}^{t}\mathbf{r}_{ij}}{\left|{}^{t}\mathbf{r}_{ij}\right|}\right) \tag{109}$$

The differentiation on ϕ_{ij} in equation (109) is w.r.t. $\left|{}^{t}\mathbf{r}_{ij}\right|$.

Using the definition of $E^0(\mathbf{R},t)$ in equation (98), its time derivative is obtained as,

$$\frac{\partial\left(E^0(\mathbf{R},t)\right)}{\partial t} = \frac{\partial}{\partial t}\sum_i\left[\left(\frac{1}{2}m_i\left|{}^{t}\mathbf{v}_i\right|^2 + \frac{1}{2}\sum_j \phi_{ij}\right)\Delta\left({}^{t}\mathbf{r}_i - \mathbf{R}\right)\right] \tag{110}$$

For brevity, define $T1$ and $T2$ as

$$T1 \equiv \frac{1}{2}m_i\left|{}^{t}\mathbf{v}_i\right|^2 + \frac{1}{2}\sum_j \phi_{ij} \tag{111}$$

$$T2 \equiv \Delta\left({}^{t}\mathbf{r}_i - \mathbf{R}\right) \tag{112}$$

In terms of $T1$ and $T2$, equation (110) can be written as

$$\frac{\partial\left(E^0(\mathbf{R},t)\right)}{\partial t} = \sum_i \frac{\partial(T1)}{\partial t}T2 + T1\frac{\partial(T2)}{\partial t} \tag{113}$$

The first derivative, $\frac{\partial(T1)}{\partial t}$, on the r.h.s. of equation (113) is obtained as

$$\frac{\partial(T1)}{\partial t} = \frac{\partial}{\partial t}\left[\frac{1}{2} m_i {}^t\mathbf{v}_i \cdot {}^t\mathbf{v}_i + \frac{1}{2}\sum_j \phi_{ij}\right] \tag{114}$$

$$\frac{\partial(T1)}{\partial t} = \left[m_i {}^t\mathbf{a}_i \cdot {}^t\mathbf{v}_i + \frac{1}{2}\sum_j \phi_{ij}^{'}\left(\frac{{}^t\mathbf{r}_{ij}}{\left|{}^t\mathbf{r}_{ij}\right|} \cdot {}^t\mathbf{v}_i\right)\right] \tag{115}$$

Using Newton's second law equation (102) and equation (109), equation (115) can be written as

$$\frac{\partial(T1)}{\partial t} = {}^t\mathbf{f}_i \cdot {}^t\mathbf{v}_i + \frac{1}{2}\sum_j \left(-\mathbf{F}_{ij}^C\right)\cdot\left({}^t\mathbf{v}_{ij}\right) \tag{116}$$

Using definition of ${}^t\mathbf{v}_{ij}$ in equation (5) and the second equality in equation (102), equation (116) is transformed as

$$\frac{\partial(T1)}{\partial t} = \frac{1}{2}\sum_j \left(\mathbf{F}_{ij}^C\right)\cdot\left({}^t\mathbf{v}_i + {}^t\mathbf{v}_j\right) \tag{117}$$

The second derivative on the r.h.s. of equation (113) is obtained as

$$\frac{\partial(T2)}{\partial t} = \frac{\partial\Delta\left({}^t\mathbf{r}_i - \mathbf{R}\right)}{\partial t} \tag{118}$$

Using the chain rule, equation (118) is written as

$$\frac{\partial(T2)}{\partial t} = \frac{\partial\Delta\left({}^t\mathbf{r}_i - \mathbf{R}\right)}{\partial t} = -\nabla_{\mathbf{R}}\Delta\left({}^t\mathbf{r}_i - \mathbf{R}\right)\cdot {}^t\mathbf{v}_i \tag{119}$$

Substituting equation (117) and equation (119) in equation (113),

$$\begin{aligned}\frac{\partial\left(E^0(\mathbf{R},t)\right)}{\partial t} = &\sum_i \frac{1}{2}\sum_j \mathbf{F}_{ij}^C \cdot\left({}^t\mathbf{v}_i + {}^t\mathbf{v}_j\right)\Delta\left({}^t\mathbf{r}_i - \mathbf{R}\right) + \\ &\sum_i\left[\left(\frac{1}{2} m_i \left|{}^t\mathbf{v}_i\right|^2 + \frac{1}{2}\sum_j \phi_{ij}\right)\left(-{}^t\mathbf{v}_i \cdot \nabla_{\mathbf{R}}\right)\left(\Delta\left({}^t\mathbf{r}_i - \mathbf{R}\right)\right)\right]\end{aligned} \tag{120}$$

In equation (120) 'i' and 'j' are dummy indices that need to be summed over so they can be interchanged. By Newton's third law $\mathbf{F}_{ij}^{C} = -\mathbf{F}_{ji}^{C}$. So the first double summation in equation (120) can be transformed as

$$\begin{aligned}
&\sum_i \frac{1}{2}\sum_j \mathbf{F}_{ij}^{C} \cdot \left({}^{t}\mathbf{v}_i + {}^{t}\mathbf{v}_j\right)\Delta\left({}^{t}\mathbf{r}_i - \mathbf{R}\right) = \sum_i \frac{1}{2}\sum_j \left(\mathbf{F}_{ij}^{C} \cdot {}^{t}\mathbf{v}_i + \mathbf{F}_{ij}^{C} \cdot {}^{t}\mathbf{v}_j\right)\Delta\left({}^{t}\mathbf{r}_i - \mathbf{R}\right) = \\
&\sum_i \frac{1}{2}\sum_j \mathbf{F}_{ij}^{C} \cdot {}^{t}\mathbf{v}_i \left(\Delta\left({}^{t}\mathbf{r}_i - \mathbf{R}\right)\right) + \mathbf{F}_{ji}^{C} \cdot {}^{t}\mathbf{v}_i \left(\Delta\left({}^{t}\mathbf{r}_j - \mathbf{R}\right)\right) = \\
&\sum_i \frac{1}{2}\sum_j \mathbf{F}_{ij}^{C} \cdot {}^{t}\mathbf{v}_i \left(\Delta\left({}^{t}\mathbf{r}_i - \mathbf{R}\right)\right) + (-\mathbf{F}_{ij}^{C}) \cdot {}^{t}\mathbf{v}_i \left(\Delta\left({}^{t}\mathbf{r}_j - \mathbf{R}\right)\right) = \\
&\sum_i \frac{1}{2}\sum_j \mathbf{F}_{ij}^{C} \cdot {}^{t}\mathbf{v}_i \left(\Delta\left({}^{t}\mathbf{r}_i - \mathbf{R}\right) - \Delta\left({}^{t}\mathbf{r}_j - \mathbf{R}\right)\right) = \\
&\sum_i \frac{1}{2}\sum_j \mathbf{F}_{ij}^{C} \cdot {}^{t}\mathbf{v}_i \left(-\left({}^{t}\mathbf{r}_{ij} \cdot \nabla_{\mathbf{R}}\right) B\left({}^{t}\mathbf{r}_i, {}^{t}\mathbf{r}_j, \mathbf{R}\right)\right)
\end{aligned} \tag{121}$$

where equation (106) has been used to replace the difference in the localization functions by the bond function in the last equality in equation (121). By substituting equation (121) in equation (120), factoring out the nabla operator and transferring the terms with the nabla operator on the LHS, equation (120) reduces to

$$\begin{aligned}
&\frac{\partial\left(E^{0}\left(\mathbf{R},t\right)\right)}{\partial t} + \nabla_{\mathbf{R}} \cdot \left[\frac{1}{2}\sum_{ij}\left(\mathbf{F}_{ij}^{C} \cdot {}^{t}\mathbf{v}_i\right){}^{t}\mathbf{r}_{ij} B\left({}^{t}\mathbf{r}_i, {}^{t}\mathbf{r}_j, \mathbf{R}\right)\right] \\
&\qquad + \nabla_{\mathbf{R}} \cdot \left[\sum_i \left(\frac{1}{2} m_i \left|{}^{t}\mathbf{v}_i\right|^2 + \frac{1}{2}\sum_j \phi_{ij}\right)\left({}^{t}\mathbf{v}_i \Delta\left({}^{t}\mathbf{r}_i - \mathbf{R}\right)\right)\right] = 0
\end{aligned} \tag{122}$$

This is equation (3.7) of Hardy[101].

The equation for the energy E is given by[101]

$$E\left(\mathbf{R},t\right) = \sum_i \left[\frac{1}{2} m_i \left|{}^{t}\mathbf{v}_i - \mathbf{u}\left(\mathbf{R},t\right)\right|^2 + \frac{1}{2}\sum_j \phi_{ij}\right]\Delta\left({}^{t}\mathbf{r}_i - \mathbf{R}\right) \tag{123}$$

When $\mathbf{u} = 0, E = E^{0}$. That is, E^{0} is the value of E at $\mathbf{u} = 0$.

$$E^0(\mathbf{R},t)=\sum_i\left[\frac{1}{2}m_i\left|{}^t\mathbf{v}_i\right|^2+\frac{1}{2}\sum_j\phi_{ij}\right]\Delta\left({}^t\mathbf{r}_i-\mathbf{R}\right) \tag{124}$$

Subtracting equation (123) from equation (124) and rearranging and using equation (101) along with the definition of local velocity $\mathbf{u}$ in equation (85),

$$E^0=E+\frac{1}{2}\rho\left|\mathbf{u}\right|^2 \tag{125}$$

This is equation (3.13) of Hardy[101].

The equation for Q_v in Hardy[101] is

$$Q_v(\mathbf{R},t)=\frac{1}{2}\sum_{ij}\left[\mathbf{F}_{ij}^C\cdot\left[{}^t\mathbf{v}_i-\mathbf{u}(\mathbf{R},t)\right]\right]{}^t\mathbf{r}_{ij}B\left({}^t\mathbf{r}_i,{}^t\mathbf{r}_j,\mathbf{R}\right) \tag{126}$$

When $\mathbf{u}=0$, $Q_v(\mathbf{R},t)=Q_v^0(\mathbf{R},t)$

$$Q_v^0(\mathbf{R},t)=\frac{1}{2}\sum_{ij}\left[\mathbf{F}_{ij}^C\cdot\left[{}^t\mathbf{v}_i\right]\right]{}^t\mathbf{r}_{ij}B\left({}^t\mathbf{r}_i,{}^t\mathbf{r}_j,\mathbf{R}\right) \tag{127}$$

For three vectors $\mathbf{a},\mathbf{b}$ and $\mathbf{c}$, the following tensor product identity holds

$$(\mathbf{a}\cdot\mathbf{b})\mathbf{c}=(\mathbf{b}\cdot\mathbf{a})\mathbf{c}=\mathbf{a}\cdot(\mathbf{b}\otimes\mathbf{c})=\mathbf{b}\cdot(\mathbf{a}\otimes\mathbf{c}) \tag{128}$$

Subtracting equation (126) from equation (127) and using equation (128) and the definition of local velocity, equation (85)

$$Q_v^0(\mathbf{R},t)-Q_v(\mathbf{R},t)=\frac{1}{2}\sum_{ij}\left(\mathbf{F}_{ij}^C\cdot\mathbf{u}(\mathbf{R},t)\right){}^t\mathbf{r}_{ij}B\left({}^t\mathbf{r}_i,{}^t\mathbf{r}_j,\mathbf{R}\right)=-\mathbf{u}\cdot\mathbf{S}_v \tag{129}$$

where $\mathbf{S}_v=-\frac{1}{2}\sum_{ij}\left(\mathbf{F}_{ij}^C\otimes{}^t\mathbf{r}_{ij}\right)B\left({}^t\mathbf{r}_i,{}^t\mathbf{r}_j,\mathbf{R}\right)$. The component form of $\mathbf{S}_v$ is

$$S_v^{\alpha\beta}=-\frac{1}{2}\sum_{ij}F_{ij}^{\alpha}r_{ij}^{\beta}B\left({}^t\mathbf{r}_i,{}^t\mathbf{r}_j,\mathbf{R}\right) \tag{130}$$

Equation (129) and equation (130) are respectively equation (3.14) and equation (4.5) of Hardy.

Similarly, the relationship between Q_k and Q_k^0 be derived in terms of the kinetic contribution to stress tensor $S_k^{\alpha\beta}$.

$$Q_k\left(\mathbf{R},t\right)=\sum_i\left[\frac{1}{2}m_i\left|{}^t\mathbf{v}_i-\mathbf{u}\right|^2+\frac{1}{2}\sum_j\phi_{ij}\right]\left({}^t\mathbf{v}_i-\mathbf{u}\right)\Delta\left({}^t\mathbf{r}_i-\mathbf{R}\right) \tag{131}$$

when $\mathbf{u}=0$, $Q_k\left(\mathbf{R},t\right)=Q_k^0\left(\mathbf{R},t\right)$

$$Q_k^0\left(\mathbf{R},t\right)=\sum_i\left[\frac{1}{2}m_i\left|{}^t\mathbf{v}_i\right|^2+\frac{1}{2}\sum_j\phi_{ij}\right]\left({}^t\mathbf{v}_i\right)\Delta\left({}^t\mathbf{r}_i-\mathbf{R}\right) \tag{132}$$

Subtracting equation (131) from equation (132) and using the equation for energy E in equation (123),

$$Q_k^0\left(\mathbf{R},t\right)-Q_k\left(\mathbf{R},t\right)=E\mathbf{u}+\sum_i\frac{1}{2}m_i\left[\left|{}^t\mathbf{v}_i\right|^2-\left|{}^t\mathbf{v}_i-\mathbf{u}\right|^2\right]\left({}^t\mathbf{v}_i\right)\Delta\left({}^t\mathbf{r}_i-\mathbf{R}\right) \tag{133}$$

Using equation (101), equation (133) is rearranged to

$$Q_k^0(\mathbf{R},t)-Q_k(\mathbf{R},t)=\mathbf{u}\left(E+\frac{1}{2}\rho\left|\mathbf{u}\right|^2\right)+\sum_i\left[m_i\left({}^t\mathbf{v}_i-\mathbf{u}\right)\cdot\left(\mathbf{u}\right)\cdot\left({}^t\mathbf{v}_i-\mathbf{u}+\mathbf{u}\right)\right]\Delta\left({}^t\mathbf{r}_i-\mathbf{R}\right) \tag{134}$$

Using the dyadic identity for the tensor product,

$$\begin{aligned}&\sum_i\left[m_i\left({}^t\mathbf{v}_i-\mathbf{u}\right)\cdot\left(\mathbf{u}\right)\cdot\left({}^t\mathbf{v}_i-\mathbf{u}\right)\right]\Delta\left({}^t\mathbf{r}_i-\mathbf{R}\right)=\\&\sum_i\left[m_i\left(\mathbf{u}\right)\cdot\left(\left({}^t\mathbf{v}_i-\mathbf{u}\right)\otimes\left({}^t\mathbf{v}_i-\mathbf{u}\right)\right)\right]\Delta\left({}^t\mathbf{r}_i-\mathbf{R}\right)=\\&-\mathbf{u}\cdot\left(\sum_i\left[-m_i\left(\left({}^t\mathbf{v}_i-\mathbf{u}\right)\otimes\left({}^t\mathbf{v}_i-\mathbf{u}\right)\right)\right]\Delta\left({}^t\mathbf{r}_i-\mathbf{R}\right)\right)\end{aligned} \tag{135}$$

$\left(\sum_i\left[-m_i\left(\left({}^t\mathbf{v}_i-\mathbf{u}\right)\otimes\left({}^t\mathbf{v}_i-\mathbf{u}\right)\right)\right]\Delta\left({}^t\mathbf{r}_i-\mathbf{R}\right)\right)$ is the kinetic contribution to stress tensor. The component form of the kinetic contribution is given as

$$S_k^{\alpha\beta}\left(\mathbf{R},t\right)=-\sum_i\left[m_i\left(\dot{r}_i^{\alpha}-u^{\alpha}\right)\left(\dot{r}_i^{\beta}-u^{\beta}\right)\right]\Delta\left({}^t\mathbf{r}_i-\mathbf{R}\right) \tag{136}$$

The remaining term of the summation in (134) is

$$\sum_i\left[m_i\left({}^t\mathbf{v}_i-\mathbf{u}\right)\cdot\left(\mathbf{u}\right)\cdot\left(\mathbf{u}\right)\right]\Delta\left({}^t\mathbf{r}_i-\mathbf{R}\right) \tag{137}$$

This can be written as $\left(\mathbf{u}\right)\cdot\left(\mathbf{u}\cdot\left(\mathbf{p}-\rho\mathbf{u}\right)\right)$ which by definition of local velocity in equation (85) is zero. So equation (134) can be written as

$$Q_k^0=Q_k-\mathbf{u}\cdot\mathbf{S}_k+\mathbf{u}\left(E+\frac{1}{2}\rho\left|\mathbf{u}\right|^2\right) \tag{138}$$

Equation (136) and equation (138) are respectively equation (4.3) and equation (3.15) of Hardy[101].

Based on Hardy's work[101], Cauchy stress is to be computed from the following relationship

$$\boldsymbol{\sigma}_T(\mathbf{R},t)=-\frac{1}{2}\sum_{i=1}^{N}\sum_{j\neq i}^{N}\mathbf{F}_{ij}^C\otimes{}^t\mathbf{r}_{ij}B({}^t\mathbf{r}_i,{}^t\mathbf{r}_j,\mathbf{R})-\sum_{i=1}^{N}m_i\,{}^t\mathbf{w}_i\otimes{}^t\mathbf{w}_i\Delta({}^t\mathbf{r}_i-\mathbf{R}) \tag{139}$$

$${}^t\mathbf{w}_i(\mathbf{R},t)\equiv{}^t\mathbf{v}_i-\mathbf{u}(\mathbf{R},t) \tag{140}$$

The first term on the RHS of equation (139) is the potential contribution to the stress tensor as given in component form in equation (130) and requires the calculation of bond function as defined in equation (93). The second term on the RHS of equation (139) is the kinetic contribution to the stress tensor that is given in component form by equation

(136) and requires the calculation of localization function. The localization function is computed as follows.

The localization function need to be computed for every particle within the averaging domain The bond function needs to be computed for every interaction pair (with its neighbors) that this particle forms. The averaging domain to be used can be sphere or a parallelepiped. In this work, a parallelepiped averaging domain has been used. Let us assume an averaging domain in the form of a parallelepiped of dimensions $2L_x, 2L_y$ and $2L_z$ respectively in the X, Y and Z direction of the XYZ coordinate system. The functional form of the localization function, used in this work, is a 3D generalization of the cosine localization function[102, 108] and is assumed to be[108]

$$\begin{aligned}\Delta &= \left[A\left(\frac{1}{2}\left(1+\cos\left(\frac{\pi x}{L_x}\right)\right)\right)\left(\frac{1}{2}\left(1+\cos\left(\frac{\pi y}{L_y}\right)\right)\right)\left(\frac{1}{2}\left(1+\cos\left(\frac{\pi z}{L_z}\right)\right)\right)\right] \\ &\quad \text{for } |x| \le L_x, |y| \le L_y, |z| \le L_y \\ &= 0, otherwise\end{aligned} \tag{141}$$

Relative to the field point (X, Y, Z) , the bounding planes of the averaging domain are at $(-L_x, +L_x)$ normal to the X direction, $(-L_y, +L_y)$ normal to the Y direction and $(-L_z, +L_z)$ normal to the Z direction. Here A is normalization constant. By requiring that the integral of Δ over all space must be unity, the normalization constant A is given as

$$A = \left(\frac{1}{L_x L_y L_z}\right) \tag{142}$$

The localization function becomes

$$\Delta = \left(\frac{1}{L_x L_y L_z}\right)\left[\left(\frac{1}{2}\left(1+\cos\left(\frac{\pi x}{L_x}\right)\right)\right)\left(\frac{1}{2}\left(1+\cos\left(\frac{\pi y}{L_y}\right)\right)\right)\left(\frac{1}{2}\left(1+\cos\left(\frac{\pi z}{L_z}\right)\right)\right)\right]$$
$$\text{for } |x| \le L_x, |y| \le L_y, |z| \le L_y \qquad (143)$$
$$= 0, \textit{otherwise}$$

The localization function can thus be computed from equation (143).

The bond function, for the pair of particles 'i' and 'j' is calculated as follows. Let the Cartesian coordinates of 'i' and 'j' be (x_i, y_i, z_i) and (x_j, y_j, z_j) respectively. The coordinates of a point on the line connecting i and j are

$$\tau(x_i - x_j, y_i - y_j, z_i - z_j) + (x_j, y_j, z_j) \qquad (144)$$

Let (X, Y, Z) be the coordinates of the point where the statistical average is desired. The coordinates of the point on the line connecting 'i' and 'j' relative to the point (X, Y, Z) are

$$\tau(x_i - x_j, y_i - y_j, z_i - z_j) + (x_j, y_j, z_j) - (X, Y, Z) \qquad (145)$$

The (x, y, z) in equation (143) can be expressed in terms of the parameter τ as

$$(x, y, z) \equiv \tau(x_i - x_j, y_i - y_j, z_i - z_j) + (x_j, y_j, z_j) - (X, Y, Z) \qquad (146)$$

Using the definition of bond function

$$B({}^t\mathbf{r}_i, {}^t\mathbf{r}_j, \mathbf{R}) \equiv \int_0^1 \Delta(\tau\, {}^t\mathbf{r}_{ij} + {}^t\mathbf{r}_j - \mathbf{R})\, d\tau \qquad (147)$$

where τ is the variable of integration. The bond function is obtained from localization function equation (143), where (x, y, z) are given in terms of τ by (146). By substituting

equation (146) in equation (143), Δ is expressed in terms of τ which is to be integrated w.r.t. τ with τ varying from 0 to 1 as in equation (147).

Once the localization function and the bond function are computed, summations in equation (139) are computed from the position vectors, velocities and forces on the particles which are output from the particle simulation.

A detailed algorithm to obtain continuum quantities from the discrete output obtained from the DPDE method is presented below. The mathematical formulation and algorithm is based on the work of Hardy[101] extended to account for finite size of particles and for the variation of continuum properties in three dimensions.

1. Choose a particle to be tracked insitu giving its row number as input in the main data matrix. Let its coordinates be (X_I, Y_I, Z_I) in the initial configuration. This is the tracked particle (TP).

2. Find the current coordinates of the tracked particle (X_R, Y_R, Z_R), which serve as the coordinates of the center of averaging domain or the field point $\mathbf{R}$ [101].

3. Construct an averaging domain centered on TP. Let the input dimensions of the averaging domain be $2L_x$, $2L_y$ and $2L_z$ in the X, Y and Z direction respectively. So the averaging domain is a region of RVE bounded by a set of six planes which are given as:

   $X_{max}=X_R+L_x$, $X_{min}=X_R-L_x$, $Y_{max}=Y_R+L_y$, $Y_{min}=Y_R-L_y$, $Z_{max}=Z_R+L_z$ and $Z_{min}=Z_R-L_z$

4. Determine spheres lying in this domain partially or fully. Let the coordinates of the center of the sphere being checked be (X_S, Y_S, Z_S). Let the radius of the sphere be R_s.

A sphere lies fully outside the averaging domain if

$X_s-R_s > X_{max}$ .OR. $X_s+R_s < X_{min}$.OR. $Y_s-R_s > Y_{max}$ .OR. $Y_s+R_s < Y_{min}$.OR. $Z_s-R_s > Z_{max}$ .OR.$Z_s+R_s < Z_{min}$

A sphere lies fully inside the averaging domain if

$X_{max} > X_s+R_s$.&. $X_{min} < X_s-R_s$. &. $Y_{max} > Y_s+R_s$. &. $Y_{min} < Y_s-R_s$. &. $Z_{max} > Z_s+R_s$. &. $Z_{min} < Z_s-R_s$

ELSE sphere lies partially inside the averaging domain

5. By going over all of the spheres of RVE, make a list of all such spheres that lie partially or totally inside the averaging domain. This will be used for computing averaged mass density, averaged energy density, averaged momentum density, mass averaged velocity and kinetic stress. Let this list be L_s. Also count the number of all such spheres. Let this be called N_s.

6. For calculation of potential contribution to stress, make a list of all particle centers that lie within the averaging domain. For this, go over all of the sphere centers in the RVE. Consider a sphere of radius 10^{-9} micron centered around the particle center. Then, proceed as in step 4. Let this list be L_c and let the number of enclosed centers be N_c.

7. The mass density, momentum density and energy density are given respectively as in equation (96), equation (97) and equation (98). For summations in equations (96) to (98) the portion of the sphere enclosed by the averaging domain (or full sphere if the sphere is totally enclosed by the averaging domain) is divided into small volume elements, so that m_i becomes the mass of small volume element.

8. Given below is the procedure to find the total mass of the sphere enclosed by the averaging domain and appropriately weighed by the localization function, m_{encl}

8.1. Choose a sphere from the list L_s. The radius of the sphere is R_s.

8.2.Construct a cube of edge length $2.2\,R_s$ concentric with the sphere.

8.3.Subdivide the cube into subcubes. Here, the cube edge is subdivided into 120 parts. The length of each subcube, L_{sub}, is 0.00916 micron.

8.4.Calculate the mass of each subcube. Let the mass of each subcube be m_{sub}. The number of subcubes be N_{sub}. m_{sub} is calculated as:

$$m_{sub} = \left(\frac{M_{sph}}{V_{sph}} \right) \times L_{sub}^3 \tag{148}$$

where M_{sph} is the input mass of the full sphere and V_{sph} is the sphere volume

8.5. $m_{encl} = 0$

8.6.DO j=1 to N_{sub}

Check if the center of the subcube lies inside the averaging domain and also inside the sphere

8.6.1. Let (X_c, Y_c, Z_c) be the center of the subcube.

8.6.2. To check if the center of the subcube lies inside the averaging domain proceed as in step 6.

8.6.3. To check if the center of the subcube lies inside the sphere:

A point (X_c, Y_c, Z_c) lies inside the sphere of radius R_s centered at (X_s, Y_s, Z_s) if

$$\left(X_c - X_s\right)^2 + \left(Y_c - Y_s\right)^2 + \left(Z_c - Z_s\right)^2 - R_s^2 < 0 \tag{149}$$

8.7.If the center of the subcube lies inside the sphere and also lies inside the averaging domain, compute the localization function for the center of the subcube else check the next subcube.

8.7.1. The localisation function Δ is given as:

$$\Delta = \left(\frac{1}{L_x L_y L_z}\right)\left[\left(\frac{1}{2}\left(1+\cos\left(\frac{\pi x}{L_x}\right)\right)\right)\left(\frac{1}{2}\left(1+\cos\left(\frac{\pi y}{L_y}\right)\right)\right)\left(\frac{1}{2}\left(1+\cos\left(\frac{\pi z}{L_z}\right)\right)\right)\right]$$

for $|x| \le L_x, |y| \le L_y, |z| \le L_y$

$=0, otherwise$

where $(x, y, z) = (\mathrm{X}_c - \mathrm{X}_R, \mathrm{Y}_c - \mathrm{Y}_R, \mathrm{Z}_c - \mathrm{Z}_R)$

8.7.2. $m_{encl} = m_{encl} + (m_{sub} \cdot \Delta)$

8.8.END DO

9. $\rho(\mathbf{R},t) = 0$; $\mathbf{p}(\mathbf{R},t) = 0$; $E^0(\mathbf{R},t) = 0$

10. DO j=1 to N_s

10.1. Take a sphere j and proceed as in step 8 to get m_{encl} for the sphere

$$\rho(\mathbf{R},t) = \rho(\mathbf{R},t) + m_{encl} \tag{150}$$

10.2. Let the velocity of sphere j obtained from the main data matrix be $\mathbf{v}_j$.

$$\mathbf{p}(\mathbf{R},t) = \mathbf{p}(\mathbf{R},t) + (m_{encl} \cdot \mathbf{v}_j) \tag{151}$$

10.3. Let the specific energy of sphere j obtained from the main data matrix be E.

$$E^0 = E^0 + (E \cdot m_{encl}) \tag{152}$$

11. END DO

12. The mass averaged velocity of the averaging domain, $\mathbf{u}$, is given as

$$\mathbf{u}(\mathbf{R},t)=\mathbf{p}(\mathbf{R},t)/\rho(\mathbf{R},t) \tag{153}$$

13. The total stress $(\boldsymbol{\sigma}_T)$ is the sum of kinetic $(\boldsymbol{\sigma}_K)$ and potential contribution $(\boldsymbol{\sigma}_P)$ to stress.

$$\boldsymbol{\sigma}_T=\boldsymbol{\sigma}_K+\boldsymbol{\sigma}_P \tag{154}$$

So to compute total stress, the kinetic and potential contributions to stress need to be computed and then summed up.

14. Given below is the procedure to calculate kinetic contribution to stress. The kinetic component of stress tensor is given as

$$\sum_{i=1}^{N} m_i\, {}^t\mathbf{w}_i \otimes {}^t\mathbf{w}_i \Delta({}^t\mathbf{r}_i-\mathbf{R}) \tag{155}$$

Here m_i is the mass of sphere enclosed by the averaging domain and ${}^t\mathbf{w}_i$ is the velocity of the sphere relative to the mass averaged velocity $\mathbf{u}$ of the averaging domain

14.1. Get the list of all sphere L_s, and the number of such spheres N_s , that lie partially or fully inside the averaging domain.

14.2. $\boldsymbol{\sigma}_K=0$

14.3. DO j=1 to N_s

14.4. Get the absolute velocity of the sphere j, ${}^t\mathbf{v}_j$, from the main data matrix of computation

14.5. Get the mass averaged velocity of the averaging domain, $\mathbf{u}$

14.6. Get the velocity of the sphere relative to the averaging domain, ${}^t\mathbf{w}_j = {}^t\mathbf{v}_j - \mathbf{u}$

14.7. Get m_{encl} as in step 8

14.8. $\boldsymbol{\sigma}_K = \boldsymbol{\sigma}_K + m_{encl}\left({}^t\mathbf{w}_j \otimes {}^t\mathbf{w}_j\right)$

$\otimes$ denotes tensor product of two vectors

14.9. END DO

15. The procedure to calculate potential contribution to stress is given below.

15.1. The potential contribution to stress is given as

$$\boldsymbol{\sigma}_p = \sum_{i=1}^{N}\sum_{j\neq i}^{N} \mathbf{F}_{ij}^C \otimes {}^t\mathbf{r}_{ij} B({}^t\mathbf{r}_i, {}^t\mathbf{r}_j, \mathbf{R}) \qquad (156)$$

where the index i is summed over all centers inside the averaging domain and index j is over all neighbours of particle i.

15.2. Get the list of sphere centers L_c , and the number of such sphere centers N_c , that lie inside the averaging domain from step 6

15.3. $\boldsymbol{\sigma}_p = 0$

15.4. DO i=1 to N_c

Get ${}^t\mathbf{r}_i$

Get the forward neighbor list for particle number 'i', L_f. Let the number of particles in this list be N_{rf}

15.5. DO j=1 to N_{rf}

Get ${}^t\mathbf{r}_j$

Set $\mathbf{F}_{ij}^C = 0$ # Set the force between the particle and its neighbor to be zero

15.6. Compute conservative force between particle i and j, $\mathbf{F}_{ij}^P$

15.7. Compute artificial viscosity force between particle i and j, $\mathbf{F}_{ij}^v$

$$\mathbf{F}_{ij}^C = \mathbf{F}_{ij}^P + \mathbf{F}_{ij}^v$$

$${}^t\mathbf{r}_{ij} = {}^t\mathbf{r}_i - {}^t\mathbf{r}_j$$

15.8. Compute bond function between particle 'i' and 'j'

15.9. The bond function between i and j is given as:

$$B\left({}^t\mathbf{r}_i, {}^t\mathbf{r}_j, \mathbf{R}\right) \equiv \int_0^1 \Delta\left(\tau\, {}^t\mathbf{r}_{ij} + {}^t\mathbf{r}_j - \mathbf{R}\right) d\tau \qquad (157)$$

15.9.1. Compute the lower limit of tau (τ)

The bond function defined in (157) is the integral of localization function along the line connecting the two particles. The localization function is defined to be zero outside of the averaging domain. So the integral in (157) is 0 outside the averaging domain. The lower limit of the definite integral in (157) needs to be adjusted so that the calculation of the definite integral is just upto the boundary of the averaging domain.

15.9.2. Subdivide the (0,1) interval for τ into n parts. Here $n=100$. Each subinterval is of length $\delta\tau$ where

$$\delta\tau = \frac{1}{n}$$

$$\tau_k = 1 - k(\delta\tau) \tag{158}$$

When $k=0$, $\tau_k = 1$ and when $k=n$, $\tau_k = 0$

15.9.3. DO k=1 to n

15.9.4. Using equation (158), compute τ_k.

15.9.5. Compute the coordinates of the point $(\tau_k \mathbf{r}_{ij} + \mathbf{r}_j - \mathbf{R})$. Let the coordinates of this point be (X_k, Y_k, Z_k)

15.9.5.1. Check if (X_k, Y_k, Z_k) lies inside the averaging domain

15.9.5.2. (X_k, Y_k, Z_k) lies inside the averaging domain of dimensions $2L_x$, $2L_y$ and $2L_z$ centered on (X_R, Y_R, Z_R) in the X, Y and Z direction respectively if

$$(X_R - L_x < X_k < X_R + L_x) \& (Y_R - L_y < Y_k < Y_R + L_y) \& (Z_R - L_z < Z_k < Z_R + L_z)$$

IF (X_k, Y_k, Z_k) lies inside the averaging domain CYCLE

ELSE lower limit of definite integral is $(X_{k+0.5}, Y_{k+0.5}, Z_{k+0.5})$ END IF

IF $k=n$, lower limit is 0 END IF

15.9.6. END DO

15.10. The lower limit of integration in equation (157) is thus obtained. Let us call it L_b (lower bound). We now evaluate the integral in equation (157) through trapezoidal rule to obtain the bond function.

15.11. Subdivide the interval $(L_b,1)$ into N sub intervals each of length h. Here, $N=100$. The first point is $x_1 = L_b$, the last point is $x_{N+1} = 1$. Then, by trapezoidal rule

$$I(f) = \int_{L_b}^{1} f(x)dx \approx \frac{h}{2}\left[f(L_b) + f(1)\right] + h\sum_{k=2}^{N} f(x_i) \qquad (159)$$

$$\boldsymbol{\sigma}_p = \boldsymbol{\sigma}_p + \mathbf{F}_{ij}^{C} \otimes {}^{t}\mathbf{r}_{ij} B({}^{t}\mathbf{r}_i, {}^{t}\mathbf{r}_j, \mathbf{R})$$

15.12. END DO

15.13. END DO

15.14. DO i=1 to N_c

15.14.1. Get the backward neighbor list for particle no. i, L_b. Let the number of particles in this list be N_{rb}.

15.14.2. DO j=1 to N_{rb}

15.14.3. Get the enclosed center list for the averaging domain. For a particle 'i', this may contain both its forward and backward neighbors.

15.14.4. Check if particle number ' j' is in the enclosed center list

15.14.5. If particle no. j is in the enclosed center list CYCLE ELSE proceed as in 15.5-15.13

15.14.6. END DO

15.15. END DO

Several assumptions were made to arrive at this formulation.

1. Hardy[101] and Zimmerman[104] assume that the forces are derivable from a potential. In the present work, in addition to a conservative Lennard-Jones force, a dissipative, a random and an artificial viscosity force exist in the formulation. It is assumed that the forces from which stresses are to be computed are the sum of Lennard-Jones and artificial viscosity force, even though no attempt was made to derive potential for the artificial viscosity force.
2. The formulation in Hardy's original work[101] introduces a one dimensional localization function. The present work uses a general form of the localization function in three dimension based on the one dimensional cosine localization function and a scaled cosine localization function appearing in Yang et al[108].
3. The particles in the present work have a finite size while Hardy's method is based on the point sized particles[101]. Finite sized particles can be partially inside the averaging domain with their centers outside. In the three dimensional cosine localization function used in this work, the variation of localization function along the portion of the particle protruding inside the averaging domain was considered. This aspect does not arise in the context of point sized particles

The averaging formulation in material coordinates based on Zimmerman's work[104] is briefly described to highlight the difference and suitability of Hardy's method[101] for this work.

In Zimmerman's work[104], the focus is on computing continuum quantities in the material frame of reference based on output obtained in MD simulations. The first Piola-Kirchhoff (PK1) stress according to Zimmerman is given by

$$\mathbf{P}(\mathbf{X},t) = -\frac{1}{2}\sum_{i=1}^{N}\sum_{j\neq i}^{N}\mathbf{F}_{ij}^{C} \otimes {}^{0}\mathbf{r}_{ij} B(\mathbf{X}) \tag{160}$$

where $\mathbf{P}(\mathbf{X},t)$ is the PK1 stress at the initial undeformed coordinate $\mathbf{X}$ at time t, $\mathbf{F}_{ij}^{C}$ is the force on atom (particle) 'i' due to particle 'j', ${}^{0}\mathbf{r}_{ij}$ is the vector pointing from particle 'j' to 'i' in the undeformed configuration as defined in equation (60) and $B(\mathbf{X})$ is the bond function in initial undeformed coordinates.

Following Hardy[101] (this is not explicit in Zimmerman), the bond function $B(\mathbf{X})$ is defined as the line integral of the localization function $\Delta(\mathbf{X})$, expressed in initial undeformed coordinates, along the line connecting the two particles 'i' and 'j'.

$$B(\mathbf{X}) \equiv \int_{0}^{1} \Delta(\tau\, {}^{0}\mathbf{r}_{ij} + {}^{0}\mathbf{r}_{j} - \mathbf{X}) d\tau \tag{161}$$

Here $\mathbf{X}$ is the initial undeformed coordinate of the point where the field is desired, ${}^{0}\mathbf{r}_{ij}$ is defined in equation (60). $\mathbf{F}_{ij}^{C} \otimes {}^{0}\mathbf{r}_{ij}$ is the tensor product of the force $\mathbf{F}_{ij}^{C}$ with ${}^{0}\mathbf{r}_{ij}$. τ is a variable of integration that assumes values between 0 and 1.

In Zimmerman's work[104], periodic boundary conditions are imposed in all directions of the simulation box and the computation appears to involve all atoms (particles) in the simulation cell. So the summation in equation (160) is over all particles and averaged quantities are for the entire domain. In the present work, the simulation cell

is bounded by walls and averaging is carried out over the selected in-situ volume domain (not full volume). From Hardy's work[101], the sum needs to be taken over the particles whose centers are within the finite averaging domain. Also the force, $\mathbf{F}_{ij}^{C}$, in Zimmerman's work needs to be computed with all atoms in the system; that is for a given atom, all the other atoms in the system need to be considered. However, the present work considers the neighbors within the cutoff distance. Thus, the in-situ averaged quantities in the present work can vary from point to point in the RVE. The reference configuration is arbitrarily chosen to be the undeformed configuration of the system. So ${}^{0}\mathbf{r}_{ij} = {}^{0}\mathbf{r}_{i} - {}^{0}\mathbf{r}_{j}$ in equation (160) is computed from the configuration at time $t = 0$. The localization function is not explicitly stated in Zimmerman[104]. Let the localization function be taken as the step function[101] in accordance with Hardy. Since the localization function has dimensions of inverse of volume and is normalized to 1, the localization function is taken to be ($1/V_0$), inside the averaging domain, where V_0 is the volume of the averaging domain (in the reference configuration) and 0 everywhere else. Then the bond function, which is the line integral of the localization function along the line connecting the two particles, is the fraction of the line connecting the two particles inside the averaging domain in the reference configuration.

APPENDIX B

HEXAHEDRON AVERAGING ALGORITHM

The computation of average mass density in Hardy's[101] approach is based on the assumption of point particles and does not take into account the pore spaces between finite sized particles. Hence, it is sensitive to particle size and inter-particle distance. The algorithm below computes mass density for micron and submicron sized particles based on the construction of hexahedron around each of the particles inside the averaging domain. The hexahedron based mass averaging approach yields converged results irrespective of the size and inter-particle spacing of the particles as shown in figure 24 below.

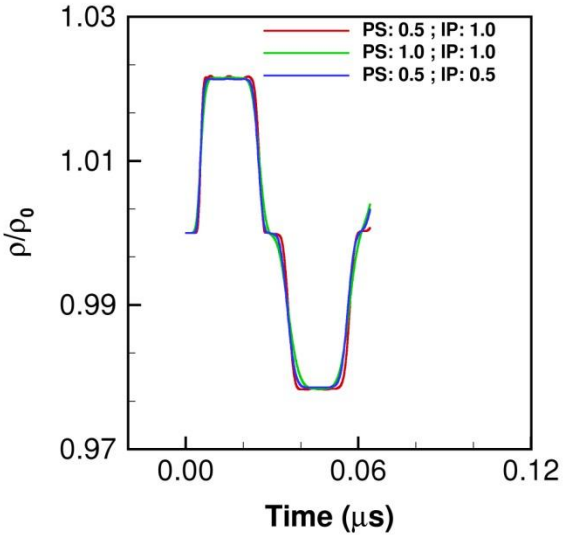

Figure 24 Converged mass densities computed using hexahedron approach.

1. Choose a particle to be tracked insitu giving its row number as input in the main data matrix. Let its coordinates be (X_I, Y_I, Z_I) in the initial configuration. This is the tracked particle (TP).

2. Find the current coordinates of the tracked particle (X_R, Y_R, Z_R). The coordinates of the center of averaging domain or the field point $\mathbf{R}_0$ is (X_R, Y_0, Z_0) for shock propagating along X-direction. Here, Y_0 , Z_0 are the respectively the Y and Z coordinates of the center of RVE cross section.

3. Construct an averaging domain centered on TP. Let the input dimensions of the averaging domain be $2L_x$, $2L_y$ and $2L_z$ in the X, Y and Z direction respectively. So the averaging domain is a region of RVE bounded by a set of six planes which are given as:

   $X_{max}=X_R+L_x$, $X_{min}=X_R-L_x$, $Y_{max}=Y_0+L_y$, $Y_{min}=Y_0-L_y$, $Z_{max}=Z_0+L_z$ and $Z_{min}=Z_0-L_z$

4. Determine if a sphere center lies inside the averaging domain. Let the coordinates of the center of the sphere being checked be (X_S, Y_S, Z_S).

   A sphere lies fully inside the averaging domain if

$$X_s \le X_{\max}.\&.X_s \ge X_{\min}.\&.Y_s \le Y_{\max}.\&.Y_s \ge Y_{\min}.\&.Z_s \le Z_{\max}.\&.Z_s \ge Z_{\min} \quad (162)$$

5. By going over all of the spheres of RVE, make a list of all such sphere centers that lie inside the averaging domain. This will be used for computing averaged mass density. Let this list be L_c. Also count the number of all such spheres. Let this be called N_c .

6. $\rho(\mathbf{R},t)=0$ where ρ is the density.

7. Do $N=1$ to N_c

   Let the IJK ordered coordinates of the sphere number N be (i,j,k). Construct 8 neighboring hexahedrons (H_i) around it whose vertices (V_i) (in terms of IJK ordered coordinates) are given in table 5 below:

Table 5: IJK ordered coordinates of vertices for hexahedron averaging

	V1	V2	V3	V4	V5	V6	V7	V8
H1	i-1,j-1,k-1	i,j-1,k-1	i,j,k-1	i-1,j,k-1	i-1,j-1,k	i,j-1,k	i,j,k	i-1,j,k
H2	i,j-1,k-1	i+1,j-1,k-1	i+1,j,k-1	i,j,k-1	i,j-1,k	i+1,j-1,k	i+1,j,k	i,j,k
H3	i,j,k-1	i+1,j,k-1	i+1,j+1,k-1	i,j+1,k-1	i,j,k	i+1,j,k	i+1,j+1,k	i,j+1,k
H4	i-1,j,k-1	i,j,k-1	i,j+1,k-1	i-1,j+1,k-1	i-1,j,k	i,j,k	i,j+1,k	i-1,j+1,k
H5	i-1,j-1,k	i,j-1,k	i,j,k	i-1,j,k	i-1,j-1,k+1	i,j-1,k+1	i,j,k+1	i-1,j,k+1
H6	i,j-1,k	i+1,j-1,k	i+1,j,k	i,j,k	i,j-1,k+1	i+1,j-1,k+1	i+1,j,k+1	i,j,k+1
H7	i,j,k	i+1,j,k	i+1,j+1,k	i,j+1,k	i,j,k+1	i+1,j,k+1	i+1,j+1,k+1	i,j+1,k+1
H8	i-1,j,k	i,j,k	i,j+1,k	i-1,j+1,k	i-1,j,k+1	i,j,k+1	i,j+1,k+1	i-1,j+1,k+1

8. Find the coordinates of the origin of each of the hexahedrons H_i (i=1 to 8). Let the coordinates of the center of each of the hexahedrons be (X_i,Y_i,Z_i) where i ranges from 1 to 8.

$$X_i=\frac{\sum_{j=1}^{8}H_i(V_{jx})}{8}\ ;\ Y_i=\frac{\sum_{j=1}^{8}H_i(V_{jy})}{8}\ ;\ Z_i=\frac{\sum_{j=1}^{8}H_i(V_{jz})}{8}\qquad \text{(i=1 to 8)} \tag{163}$$

where the subscript i refers to the hexahedron in table 5 (rows), the subscript j refers to the vertex (columns) in table 5 and the subscripts (x,y,z) denote the (X,Y,Z) coordinates of the vertex j respectively. The vertices (X_i,Y_i,Z_i) where $(i=1\text{ to }8)$ are the vertices of the pseudo-hexahedron surrounding the sphere N.

9. The volume of the pseudo-hexahedron, V_{p-hexa} , is then calculated. The volume calculation is based on the premise that any hexahedron can be subdivided into six pyramidal bodies where the vertex of the pyramid is the center of the sphere for which the pseudo-hexahedron has been constructed. Each pyramid has a quadrilateral base and can be subdivided into two tetrahedrons. The volume of the pyramid is the sum of the volume of the two tetrahedrons. Let the coordinates of the vertices of the tetrahedron be given as:

$$\{(x_1, y_1, z_1) ,(x_2, y_2, z_2),(x_3, y_3, z_3),(x_4, y_4, z_4)\}$$

Then the volume of the tetrahedron is given as:

$$V_T = \frac{1}{6}\left\| Det\begin{pmatrix} x_2 - x_1 & x_3 - x_1 & x_4 - x_1 \\ y_2 - y_1 & y_3 - y_1 & y_4 - y_1 \\ z_2 - z_1 & z_3 - z_1 & z_4 - z_1 \end{pmatrix}\right\| \tag{164}$$

10. If V_{P-hexa} be the volume of the pseudo-hexahedron and M be the mass of the particle which is enclosed by the pseudo-hexahedron, the density of pseudo-hexahedron is

$$\rho_{hexa} = \frac{M}{V_{p-hexa}} \tag{165}$$

11. Let N_{sub} may be the number of the sub-hexahedrons into which the pseudo-hexahedron is subdivided. Let $V_{sub-hexa}$ be the volume of the sub-hexahedron. Let $m_{sub} = V_{sub-hexa} \times \rho_{hexa}$ be the mass of the sub-hexahedron into which the pseudo-hexahedron is subdivided.

12. Given below is the procedure to find the total mass of the particle N enclosed by the averaging domain and appropriately weighed by the localization function. Let this mass be m_{encl} .

12.1. $m_{encl} = 0$ # Set enclosed particle mass to be zero

12.2. DO j=1 to N_{sub} # Go over all the sub-hexahedrons

12.2.1. Let (X_C, Y_c, Z_c) be the center of the sub-hexahedron.

12.2.2. Check if the center of the sub-hexahedron lies inside the averaging domain by proceeding as in step 4.

12.2.3. If the center of the sub-hexahedron lies inside the averaging domain, compute the localization function for the center of the sub-hexahedron else check the next sub-hexahedron.

12.2.3.1. The localization function Δ is given as in equation (141)

12.2.3.2. $$m_{encl} = m_{encl} + \left(m_{sub} \cdot \Delta \right) \tag{166}$$

12.3. END DO

$$\rho\left(\mathbf{R}, t\right) = \rho\left(\mathbf{R}, t\right) + m_{encl} \tag{167}$$

13. END DO

APPENDIX C

Manuscript published in the Proceedings of the 18th APS-SCCM/24th AIRAPT Joint Conference, July 7-12, 2013, Seattle, WA, Editors: William Butler and Will Evans, Journal of Physics, Conference Series, vol. 500, P172002, 2014

DPDE-based mesoscale simulations of shock response of HE composites

P Sood[1], S Dwivedi[1*], J Brennan[2], N Thadhani[1] and Y Horie[3]

[1]School of Materials Sci. Eng., Georgia Institute of Technology, Atlanta, GA 30332
[2]U.S. Army Research Laboratory, Aberdeen Proving Ground, MD 21005 USA
[3]Air Force Research Lab (Retd.), Eglin Air Force Base, FL 32547, USA

[*]E-mail: sdwivedi6@mail.gatech.edu

Abstract. The dissipative particle dynamics with energy conservation (DPDE) method is extended to simulate the shock response of high energetic (HE) materials at micron length scales. The symmetrical impact of an RDX impactor and target plates with 1μm diameter spheres is simulated at planar impact velocities of 208 m/s and 876 m/s with a Lennard-Jones-like potential, dissipative, and random forces, and artificial viscosity force between particles. The in situ shock quantities were obtained using Hardy's averaging. In situ longitudinal stresses from simulations were 0.84 and 3.82 GPa. Values from the literature are 0.81 and 2.92 GPa at the two impact velocities, respectively. The uniaxial strain condition was predicted with equal lateral stresses and negligible shear stresses. The higher stress value at 876 m/s may be due to lack of inelasticity in the interparticle potential. The temperature increases of 5.5 ^{0}K and 93.7 ^{0}K, respectively, were predicted assuming dissipation of a fraction of the potential energy. It is concluded that the DPDE method holds promise for a unified computational framework for multi-scale simulations of HE.

1. Introduction

The dissipative particle dynamics with energy (DPDE) conservation method [1,2] may successfully simulate the shock response of condensed phase high energy (HE) materials due to the built-in conservation of mass, momentum, and energy. Developed as the isothermal dissipative particle dynamics (DPD) method and used at molecular scales for gases and liquids [3,4], addition of particle internal energy (DPDE) as a variable allows the temperature variations needed for shock propagation simulation without the need to solve heat transport equations. This method has been extended to coarse grained molecular scales for HE [5] and to nanoscales for polymers [6]. It has yet to be applied at the micron and sub-micron length scales for solids. The shock response of HE, leading to detonation, has a transitory state where (a) the solid phase undergoes deformation, failure, and heating at heterogeneous mesoscale [7]; (b) a decomposed state with energy release and heating; and (c) a gas phase with energy release and heating. Each of these phases coexists with different length scales. Finite element methods have been used for inhomogeneous mesoscale simulation of solids [8], and fluid dynamics methods are used to study detonation under the detonation shock dynamics (DSD) field. No computational tools exist, to the best of our knowledge, that can model and simulate the coupled response of the heterogeneous transitory state with a mixture of phases and length scales.

[*]To whom any correspondence should be addressed.

With the recent focus on particle methods for condensed phase HE [9], the DPDE method may be better suited to this task, given that, on the one hand, it can be extended to the molecular length scale from which it originated, and that evolving failures and phases, on the other hand, can be modeled naturally on-the-fly. For example, using DPDE, solid failures (inter- and intra-grain fracture, voids, etc.) can be modeled by dissociating a particle from its neighbors; different phases can be modeled by transitioning to a different set of interparticle potentials; and permeation can be modeled by decomposing a particle into sub-particles. The present work explores whether the DPDE method is applicable at the micron and sub-micron mesoscale lengths of solids while still preserving its core features.

2. Objectives

The ultimate motivation is to arrive at a unified multiscale, multiphase, simulation framework for HE, while the present objectives are to extend the DPDE method to simulate the shock response of materials at a micron length scale, determine simulation parameters, retrieve in situ averaged shock response parameters for comparison with experimental data, and quantify the in situ shock response for a given impact loading.

3. DPDE Methodology and In Situ Averaged Shock Quantities

For a comprehensive description of the DPDE method, the reader is referred to previous work [2]. Key features of extending this method to the micron length scale and averaging in situ quantities, however, are presented below. It is assumed that the stochastic fluctuation-dissipation theorem is applicable at the micron length scale. Analogous to the molecular dynamics (MD) method, the DPDE method simulates the shock response of materials by integrating a set of equations-of-motion, where the forces on particle i from neighbouring particles, j, are given as,

$$ {}^{t}\mathbf{f}_i = \sum_{j \neq i} \left({}^{t}\mathbf{F}_{ij}^{P} + {}^{t}\mathbf{F}_{ij}^{D} + {}^{t}\mathbf{F}_{ij}^{R} + {}^{t}\mathbf{F}_{i}^{ext} + {}^{t}\mathbf{F}_{ij}^{v} \right) \tag{1} $$

The force components, shown in brackets above from left to right, are the interparticle potential, dissipative, random, and external forces. The left superscript, t, denotes time. The last term represents the artificial viscosity force component used in the DPDE method for the first time. A Lennard-Jones like potential is adopted in this work from [10] and is given as,

$$ {}^{t}\mathbf{F}_{ij}^{P} = \frac{A\alpha mn}{(n-m)} \left[\left(\frac{r_0}{{}^{t}r_{ij}} \right)^{n+1} - \left(\frac{r_0}{{}^{t}r_{ij}} \right)^{m+1} \right] {}^{t}\mathbf{n}_{ij} \tag{2} $$

where A is the cross-sectional area of the particle; α, m, n are the material parameters; and r_0 is the equilibrium separation between particles. Denoting the position vector of particle i by r_i and the position vector from particle j to particle i by $\mathbf{r}_{ij} = r_i - r_j$, the interparticle distance ${}^{t}r_{ij}$ represents the particle separation. The unit vector at time, t, is ${}^{t}\mathbf{n}_{ij} = {}^{t}\mathbf{r}_{ij} / {}^{t}r_{ij}$. Dissipative and random forces are,

$$ {}^{t}\mathbf{F}_{ij}^{D} = -\gamma_{ij}\omega^{D} \left[{}^{t}\mathbf{n}_{ij} \cdot {}^{t}\mathbf{p}_{ij} \right] {}^{t}\mathbf{n}_{ij} \quad ; \quad {}^{t}\mathbf{F}_{ij}^{R} = m_{ij}a_{ij}\omega^{R}\varsigma_{ij}\Delta t^{-0.5}\, {}^{t}\mathbf{n}_{ij} \quad ; \quad \omega^{D} = \left(\omega^{R}\right)^{2} = \left(1 - \frac{{}^{t}r_{ij}}{r_c} \right)^{2} \tag{3} $$

where γ_{ij}, ω^{D} and a_{ij}, ω^{R} are the amplitudes and weight functions of the dissipative and random forces respectively, $\mathbf{p}_i$ is the momentum vector of particle i with $\mathbf{p}_{ij} = \mathbf{p}_i - \mathbf{p}_j$, m_{ij} $(= m_i = m_j)$ is the particle mass, ς_{ij} is a random number from the standard normal distribution with zero mean and unit variance, and Δt is the time step. The final part of equation (3) represents the relationship between ω^{D} and ω^{R} from [2] in which r_c is the interaction range for the dissipative and random interactions. The artificial viscosity force, as a combination of linear and quadratic terms, is given as,

$$ {}^{t}\mathbf{F}_{ij}^{v} = -A\frac{{}^{t}\dot{r}_{ij}}{\left|{}^{t}\dot{r}_{ij}\right|}\left[C_1\frac{\left|{}^{t}\dot{r}_{ij}\right|}{{}^{t}r_{ij}} + C_2\left(\frac{{}^{t}\dot{r}_{ij}}{{}^{t}r_{ij}}\right)^2\right] \quad ; \quad if \;\; {}^{t}\dot{r}_{ij}\left({}^{t}r_{ij} - r_0\right) > 0 \tag{4} $$

where C_1 and C_2 are constants. The stochastic and deterministic integration of the equation-of-motion (1) is carried out using a modification to scheme [2], given in condensed form as,

$$ {}^{t}\mathbf{v}_i = {}^{t-\Delta t/2}\mathbf{v}_i - 0.5\Delta t\gamma_{ij}\omega^D\left[{}^{t}\mathbf{n}_{ij}\cdot{}^{t-\Delta t/2}\mathbf{v}_{ij}\right]{}^{t}\mathbf{n}_{ij} + 0.5\sqrt{\Delta t}a_{ij}\omega^R\zeta_{ij}\,{}^{t}\mathbf{n}_{ij} \tag{5} $$

$$ \begin{aligned} {}^{t+\Delta t/2}\mathbf{v}_i = {}^{t}\mathbf{v}_i &+ 0.5\sqrt{\Delta t}a_{ij}\omega^R\zeta_{ij}\,{}^{t}\mathbf{n}_{ij} - 0.5\Delta t\gamma_{ij}\omega^D\left[{}^{t}\mathbf{n}_{ij}\cdot{}^{t}\mathbf{v}_{ij}\right]{}^{t}\mathbf{n}_{ij} \\ &- 0.5\Delta t\gamma_{ij}\omega^D\left[{}^{t}\mathbf{n}_{ij}\cdot\left\{\Delta t^{0.5}a_{ij}\omega^R\zeta_{ij}\,{}^{t}\mathbf{n}_{ij} - \Delta t\gamma_{ij}\omega^D\left({}^{t}\mathbf{n}_{ij}\cdot{}^{t}\mathbf{v}_{ij}\right){}^{t}\mathbf{n}_{ij}\right\}\right]{}^{t}\mathbf{n}_{ij} \\ &+ \Delta t\,{}^{t}\mathbf{F}_i^C/m_i \end{aligned} \tag{6} $$

where $\mathbf{F}_i^C$ is the sum of the interparticle and artificial viscosity forces. Integration is carried out for $j > i$ and the negative of the stochastic incremental velocities are updated for particle j. Finally, the particle position is updated as,

$$ {}^{t+\Delta t}\mathbf{r}_i = {}^{t}\mathbf{r}_i + \Delta t\,{}^{t+\Delta t/2}\mathbf{v}_i \tag{7} $$

The particle internal energy (u) calculation is performed (as in equation (21) of [2]) for the conductive and mechanical contributions, while the interparticle potential, equation (2), is integrated to determine potential energy. The internal temperature θ_i of particle i is calculated from the relationship ${}^{t+\Delta t}u_i = m_i C_v\,{}^{t+\Delta t}\theta_i$, where C_v is the material specific heat. The in situ averaged shock quantities are calculated following the Hardy method [11] in current coordinates using a 3D cosine function as the localization function Δ.

4. Simulation and Results

4.1 Simulation Procedure

The shock response of RDX was simulated for an assumed planar symmetric plate impact experiment. Figure 1(a) shows the simulation representative volume element (RVE) of a 20 μm x 20 μm cross-section with a 50 μm thick RDX plate impacting a 100 μm thick RDX sample. Both the impactor and sample were modeled as regularly stacked 1μm diameter spheres with a center-to-center equilibrium distance of 1 μm. The total mass of the impactor and sample was lumped equally among their particles. The longitudinal (X-) impact velocity to the impactor particles and 300 ^{0}K temperature to all particles were assigned as initial conditions, while the lateral velocities were constrained for particles at the RVE boundaries as boundary conditions. Instead of using a contact algorithm, the interaction between the impactor and the sample

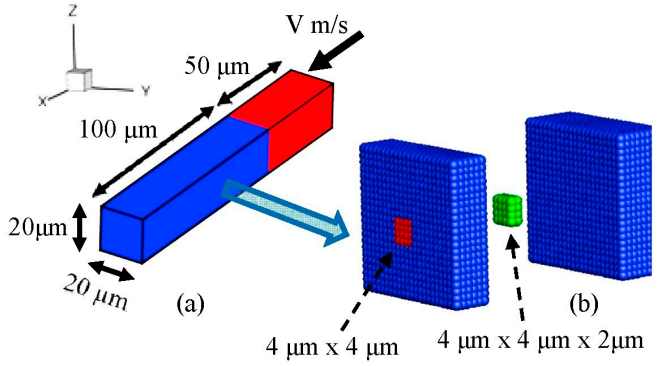

Figure 1. Schematic of (a) simulation RVE and (b) zoomed view showing the averaging domain for free surface velocity (red) and in situ shock quantities (green).

particles was analyzed using the interparticle potential—treating the two as one body. For this reason, results are presented for the time when the release wave from the sample's free surface reaches the impactor-sample interface. Simulations were carried out at impact velocities of 208 m/s and 876 m/s to explore the DPDE method for an elastic particle velocity of 104 m/s and an inelastic particle velocity of 438 m/s, respectively, in the (100) direction of Hooks et al. [12] data. The free surface velocity was calculated by averaging the longitudinal velocity of the particles over a 4 μm x 4 μm surface area, shown in red; the in situ shock parameters were obtained by averaging in a 4 μm x 4 μm x 2 μm volume, shown in green in the zoomed figure 1(b). The averaging volume was centered with the cross-section and longitudinally followed a specified particle center.

4.2 Materials Properties

The properties of materials used in the simulations are summarized in Table 1. The mass density and specific heat values are in the range of experimental values [13,14]. The parameters of the dissipative and random forces were adapted from Lisal et al. [2]. The interparticle potential parameter α [10] was calculated for RDX by adopting an average Young's modulus of 19.29 GPa [15]. Simulations considered the particles' first nearest-neighbor at 1 μm, the second nearest neighbor (face diagonal) at $2^{1/2}$ μm, and the third nearest neighbor (body diagonal) at $3^{1/2}$ μm. A constant cutoff distance of 1.5 μm from the equilibrium position in the attraction (or tensile) phase was used for all three neighbor types. The (m,n) parameters of the interparticle potential given in equation (2) were varied as (2,4), (2,3), and (1,2) reducing the slope of the curve (or, a reduction in the materials stiffness) in the repulsion (or compressive) phase. The value of (2,4) is the same as that used by Tang et al. [10] for HMX. The use of the same α and (m, n) parameters resulted in different potentials for the second and third nearest neighbor types.

Table 1. Materials and DPDE parameters used in simulations.

ρ	C_v	α	$a_{ij} = a$	C_1	C_2
(kg/m^3)	(J/kg/^{0}K)	(GPa)	(ms$^{-1.5}$)	(kg/m/s)	(kg/m)
1820.0	1046.0	2.1964	2.34x10^{-4}	3.931	7.28x10^{-9}

4.3 Results and Discussion

In the initial simulations, tolerance issues and optimal integration time step (Δt) determination were targeted. Simulations were stable and yielded identical results for $\Delta t \leq 0.14 \times 10^{-9}$ seconds. All results presented below are from simulations with a constant Δt of 0.14×10^{-10} seconds. Figure 2 compares the free surface velocity profiles at 208 m/s impact velocity simulated with and without artificial viscosity. Similar results were obtained at an impact velocity of 876 m/s. As found in shock propagation simulations using finite difference/element methods, the linear and quadratic artificial viscosities effectively damp oscillations in the free

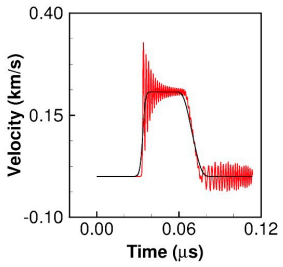

Figure 2. Free surface velocity without (red) and with (black) artificial viscosity at 208 m/s impact velocity.

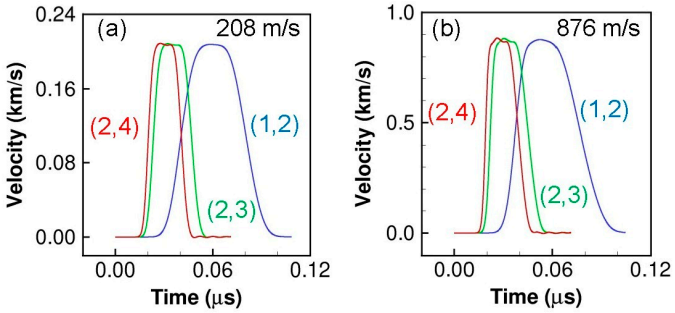

Figure 3. Free surface velocity profiles at (a) 208 m/s and (b) 876 m/s for the three pairs of (m,n) parameters.

surface velocity and other in situ shock quantities predicted by the DPDE method. Figure 3 shows the average free surface velocities at the two impact velocities for the three sets of (m, n) parameters. The simulations predicted a steady peak shock state, independent of the potential parameters, in qualitative agreement with experimental data [12]. The velocity profiles agree with the shock propagation theory. The free surface velocity increases on arrival of the shock wave from the impact surface, attains peak, and remains constant representing the shock state (plateau) under the combined influence of the shock and release waves reflected from the free surface. The velocity begins decreasing to zero after the rarefaction wave from the impactor free surface arrives at the target's free surface. Shock velocity was calculated from the time of the half-rise of the free surface velocity. Shock velocity diminishes and shock rise time increases as the interparticle stiffness drops from (2,4) to (1,2) parameter values.

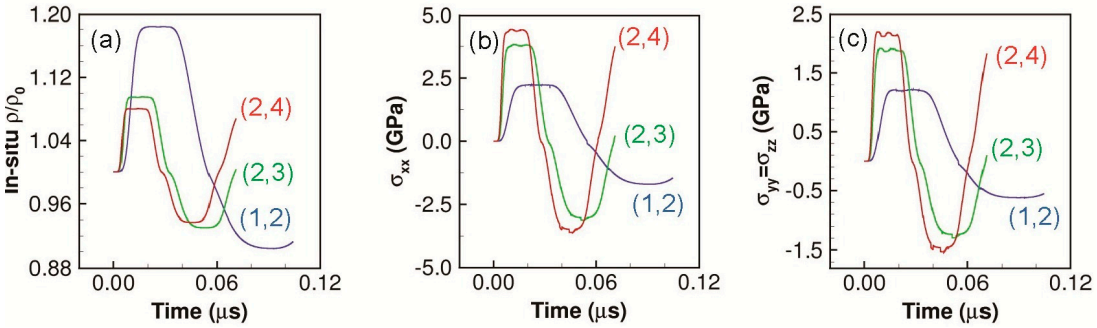

Figure 4. In situ profiles for (a) mass density, (b) longitudinal stress, and (c) lateral stresses at 876 m/s impact velocity for the three pairs of (m,n) parameters.

Figure 4 shows the in situ average mass density, longitudinal stress, and lateral stresses at 876 m/s impact velocity with positive values representing compression. The stresses begin to increase on arrival of the shock wave; they peak, and then remain constant (plateau) until the arrival of the release wave. Due to the proximity of the averaging domain to the impact surface, the rarefaction wave from the impactor's free surface reduces the stress to zero. The stresses become tensile (negative) on arrival of the release wave from the target's free surface. The simulations predicted nearly constant peak values of the shocked mass density increasing with the reduction in the interparticle stiffness. The reduced shock speed and increased compression are associated with lower in situ longitudinal stress.

The method did not predict the measured [12] two wave profiles at 876 m/s attributed to inelastic (plastic) deformation, shown in Figures 3 and 4. The onset of inelastic deformation reduces the slope of the longitudinal stress vs. strain curve and, in turn, reduces the wave speed (termed inelastic wave speed). The data shows two wave profiles due to a slower inelastic wave following the elastic wave. The single wave profile represents either the elastic wave at lower impact stresses (as in the case of 208 m/s) or the elastic wave overtaken by the inelastic wave at higher impact stresses. The Lennard-Jones like potential used in the simulations has a continuously increasing force-displacement slope without any reduction expected at the elastic-inelastic transition. This may be why the measured two wave profile was not predicted at 876 m/s. The peak longitudinal stress values at the two velocities for the (2,3) parameters were 0.84 and 3.82 GPa compared to 0.81 and 2.92 GPa, respectively [12]. The over-prediction may further indicate that the elastic response at 876 m/s was predicted by the simulation because inelasticity limits deviatoric stress, which, in turn, lowers longitudinal stress below the elastic value.

As an approximation, 90% of the potential energy was dissipated as heat to explore heat dissipation and conduction in the DPDE method. Table 2 lists calculated temperature and other in situ quantities in the peak shock state. Moreover, the reduction of in situ longitudinal and lateral stress difference as the (m,n) parameters varied from (2,4) to (1,2), shows the strength of the prediction capability of this method. The stress difference is the material's strength under the uniaxial strain condition as per the von-Mises plasticity theory.

Table 2. In situ average shock parameters (u_p - particle velocity, U - shock velocity).

Impact Velocity (m/s)	m	n	u_p (m/s)	U (m/s)	σ_{xx} (GPa)	σ_{yy} (GPa)	T (^{0}K)
208.0	2	4	105.9	4944.9	0.97	0.45	305.4
	2	3	105.7	4285.2	0.84	0.40	305.5
	1	2	104.2	2494.1	0.49	0.24	305.7
876.0	2	4	446.6	5305.0	4.42	2.11	392.1
	2	3	445.2	4595.9	3.82	1.91	393.7
	1	2	441.1	2704.2	2.23	1.20	396.9

5. Conclusions

The present work successfully extends the DPDE method to simulate the shock response of materials to the micron scale. This method predicted the free surface velocity and in situ average shock response in qualitative agreement with the uniaxial shock wave propagation theory. The longitudinal stress value at the two impact velocities was close to the literature value, however quantitative agreement cannot be established due to the lack of inelasticity in the interparticle potential. The heat dissipation and conduction built into DPDE was verified through an approximation of dissipating a fraction of the potential energy. The calculated temperature rise, therefore, should be treated as a model calculation. Nevertheless, this first use of artificial viscosity led to prediction of a smooth shock wave profile. The present work is being extended to incorporate a contact algorithm to model the impactor-sample interface and interparticle potential with inelasticity. It can be concluded that the present DPDE implementation has potential to link the continuum scale to the micron and sub-micron length scales, preserving the emphasis on interparticle interactions based on potential rather than continuum phenomenological models.

Acknowledgements

This work is supported by a Defense Threat Reduction Agency (DTRA) grant HDTRA1-01-12-0004.

References

[1] Avalos J B and Mackie A D 1997 *Europhys. Lett.* **40** 141
[2] Lisal M, Brennan J K and Avalos J B 2011 *J. Chem. Phys.* **135** 204105-18
[3] Hoogerbrugge P J and Koelman J M V A 1992 *Europhys. Lett.* **19** 155
[4] Groot R D and Warren P B 1997 *J. Chem. Phys.* **107** 4423-35
[5] Brennan J K, Lisal M, Moore J D, Izvekov S, et. al. 2014, *submitted to J Chem. Phys. Comm.*
[6] Ju S-P, Wang Y-C, Huang, G-J and Chang J-W 2013 RSC Advances **3** 8298
[7] Menikoff R 2009 *Proceedings of the APS-SCCM Conference* ed M L Elert, W T Buttler, M D Furnish, W W Anderson and W G Proud. (AIP Publishing) pp 18-25
[8] Dwivedi S K, Asay J R and Gupta Y M 2006 *J. App. Phys.* **100** 083509
[9] Yang G, Fu Y, Hu D and Han X 2013 *Comp. Fluids* **88** 51-59
[10] Tang Z P, Horie Y and Psakhie S G 1997 *High-Pressure Shock Compression of Solids* IV; *High-Pressure Shock Compression of Condensed Matter* ed L Davison, Y Horie and M Shahinpoor. (New York: Springer) pp 143-75.
[11] Hardy R J 1982 Shock waves *J. Chem. Phys.* **76** 622-28
[12] Hooks D E, Ramos K J and Martinez A R 2011 *J. Appl. Phys.* **109** 089901-2
[13] Miller G R and Garroway A N 2001*Naval Research Laboratory Report NRL/MR/6120-01-8585*
[14] Miller M S 1997 *Army Research Laboratory Report ARL-TR-1319*
[15] Haycraft J J, Stevens L L and Eckhardt C J 2006 *J. Chem. Phys.* **124** 024712-11

REFERENCES

[1] Bathe, K.-J., Ramm, E. and Wilson, E. L., "Finite element formulations for large deformation dynamic analysis," International Journal for Numerical Methods in Engineering, vol. 9 (2), pp. 353-386, 1975.

[2] Hansson, T., Oostenbrink, C. and van Gunsteren, W., "Molecular dynamics simulations," Current Opinion in Structural Biology, vol. 12 (2), pp. 190-196, 2002.

[3] Monaghan, J. J., "Smoothed particle hydrodynamics," Reports on Progress in Physics, vol. 68 (8), pp. 1703-1759, 2005.

[4] Yano, K. and Horie, Y., "Discrete-element modeling of shock compression of polycrystalline copper," Physical Review B, vol. 59 (21), pp. 13672-13680, 1999.

[5] Dawson, J. M., "Particle simulation of plasmas," Reviews of Modern Physics, vol. 55 (2), pp. 403-447, 1983.

[6] Liu, W. K., Jun, S. and Zhang, Y. F., "Reproducing kernel particle methods," International Journal for Numerical Methods in Fluids, vol. 20 (8-9), pp. 1081-1106, 1995.

[7] Fermeglia, M. and Pricl, S., "Multiscale modeling for polymer systems of industrial interest," Progress in Organic Coatings, vol. 58 (2–3), pp. 187-199, 2007.

[8] Kadau, K., Germann, T. C. and Lomdahl, P. S., "MOLECULAR DYNAMICS COMES OF AGE: 320 BILLION ATOM SIMULATION ON BlueGene/L," International Journal of Modern Physics C, vol. 17 (12), pp. 1755-1761, 2006.

[9] Mackie, A. D., Avalos, J. B. and Navas, V., "Dissipative particle dynamics with energy conservation: Modelling of heat flow," Physical Chemistry Chemical Physics, vol. 1 (9), pp. 2039-2049, 1999.

[10] Hoogerbrugge, P. J. and Koelman, J. M. V. A., "Simulating Microscopic Hydrodynamic Phenomena with Dissipative Particle Dynamics," EPL (Europhysics Letters), vol. 19 (3), pp. 155-160, 1992.

[11] Holian, B. L. and Lomdahl, P. S., "Plasticity Induced by Shock Waves in Nonequilibrium Molecular-Dynamics Simulations," Science, vol. 280 (5372), pp. 2085-2088, 1998.

[12] Kadau, K., Germann, T. C., Lomdahl, P. S. and Holian, B. L., "Microscopic View of Structural Phase Transitions Induced by Shock Waves," Science, vol. 296 (5573), pp. 1681-1684, 2002.

[13] Ganzenmuller, G. C., Hiermaier, S. and Steinhauser, M. O., "Shock-wave induced damage in lipid bilayers: a dissipative particle dynamics simulation study," Soft Matter, vol. 7 (9), pp. 4307-4317, 2011.

[14] Farrow, M. R. and Probert, M. I. J., "Atomistic molecular dynamics simulations of shock compressed quartz," Journal of Chemical Physics, vol. 135 (4), pp. 044508-07, 2011.

[15] Yano, K. and Horie, Y., "Mesomechanics of the α–ε transition in iron," International Journal of Plasticity, vol. 18 (11), pp. 1427-1446, 2002.

[16] van Beest, B. W. H., Kramer, G. J. and van Santen, R. A., "Force fields for silicas and aluminophosphates based on ab initio calculations," Physical Review Letters, vol. 64 (16), pp. 1955-1958, 1990.

[17] Ahmed, A. and Sadus, R. J., "Phase diagram of the Weeks-Chandler-Andersen potential from very low to high temperatures and pressures," Physical Review E, vol. 80 (6), pp. 061101-09, 2009.

[18] Weeks, J. D., Chandler, D. and Andersen, H. C., "Role of Repulsive Forces in Determining the Equilibrium Structure of Simple Liquids," The Journal of Chemical Physics, vol. 54 (12), pp. 5237-5247, 1971.

[19] Stoltz, G., "A reduced model for shock and detonation waves. I. The inert case," EPL (Europhysics Letters), vol. 76 (5), pp. 849-855, 2007.

[20] Varshni, Y. P. and Bloore, F. J., "Rydberg Function as an Interatomic Potential for Metals," Physical Review, vol. 129 (1), pp. 115-121, 1963.

[21] Shardlow, T., "Splitting for Dissipative Particle Dynamics," SIAM J. Sci. Comput., vol. 24 (4), pp. 1267-1282, 2002.

[22] Maillet, J. B., Soulard, L. and Stoltz, G., "A reduced model for shock and detonation waves. II. The reactive case," EPL (Europhysics Letters), vol. 78 (6), pp. 68001-06, 2007.

[23] Maillet, J. B., Bourasseau, E., Desbiens, N., Vallverdu, G. and Stoltz, G., "Mesoscopic simulations of shock-to-detonation transition in reactive liquid high explosive," EPL (Europhysics Letters), vol. 96 (6), pp. 68007-06, 2011.

[24] Moore, J. D., Izvekov, S., Lisal, M. and Brennan, J. K., "Particle based multiscale modeling of the dynamic response of RDX," AIP Conference Proceedings, vol. 1426 (1), pp. 1237-1240, 2012.

[25] Mescheryakov, Y. I., Mahutov, N. A. and Atroshenko, S. A., "Micromechanisms of dynamic fracture of ductile high-strength steel," Journal of the Mechanics and Physics of Solids, vol. 42 (9), pp. 1435-1457, 1994.

[26] Hooks, D. E., Ramos, K. J. and Martinez, A. R., "Erratum: ``Elastic-plastic shock wave profiles in oriented single crystals of cyclotrimethylene trinitramine (RDX) at 2.25 GPa" [J. Appl. Phys. , 024908 (2006)]," Journal of Applied Physics, vol. 109 (8), pp. 089901-2, 2011.

[27] Andrade, J. and Borja, R., "Finite element simulation of deformation bands in saturated granular media with inhomogeneous porosities at the meso-scale," in *III European Conference on Computational Mechanics*, edited by C. A. Motasoares, J. A. C. Martins, H. C. Rodrigues, J. C. Ambrósio, C. A. B. Pina, C. M. Motasoares, E. B. R. Pereira and J. Folgado (Springer Netherlands, 2006), pp. 582-582.

[28] Bdzil, J. B. and Stewart, D. S., "Modeling two-dimensional detonations with detonation shock dynamics," Physics of Fluids A: Fluid Dynamics (1989-1993), vol. 1 (7), pp. 1261-1267, 1989.

[29] Avalos, J. B. and Mackie, A. D., "Dissipative particle dynamics with energy conservation," EPL (Europhysics Letters), vol. 40 (2), pp. 141-146, 1997.

[30] Español, P., "Dissipative particle dynamics with energy conservation," EPL (Europhysics Letters), vol. 40 (6), pp. 631-636, 1997.

[31] Frisch, U., Hasslacher, B. and Pomeau, Y., "Lattice-Gas Automata for the Navier-Stokes Equation," Physical Review Letters, vol. 56 (14), pp. 1505-1508, 1986.

[32] Chopard, B., Ouared, R., Deutsch, A., Hatzikirou, H. and Wolf-Gladrow, D., "Lattice-Gas Cellular Automaton Models for Biology: From Fluids to Cells," Acta Biotheor, vol. 58 (4), pp. 329-340, 2010.

[33] Koelman, J. M. V. A. and Hoogerbrugge, P. J., "Dynamic Simulations of Hard-Sphere Suspensions Under Steady Shear," EPL (Europhysics Letters), vol. 21 (3), pp. 363-368, 1993.

[34] Boek, E. S., Coveney, P. V., Lekkerkerker, H. N. W. and van der Schoot, P., "Simulating the rheology of dense colloidal suspensions using dissipative particle dynamics," Phys. Rev. E, vol. 55 (3), pp. 3124-3133, 1997.

[35] Liu, M. B., Chang, J. Z., Liu, H. T. and Su, T. X., "MODELING OF CONTACT ANGLES AND WETTING EFFECTS WITH PARTICLE METHODS," International Journal of Computational Methods, vol. 08 (04), pp. 637-651, 2011.

[36] Martys, N. S., "Study of a dissipative particle dynamics based approach for modeling suspensions," Journal of Rheology, vol. 49 (2), pp. 401-424, 2005.

[37] Ripoll, M. and Ernst, M. H., "Model system for classical fluids out of equilibrium," Physical Review E, vol. 71 (4), pp. 041104-14, 2005.

[38] Willemsen, S. M., Hoefsloot, H. C. J. and Iedema, P. D., "Mesoscopic Simulation of Polymers in Fluid Dynamics Problems," Journal of Statistical Physics, vol. 107 (1), pp. 53-65, 2002.

[39] Ripoll, M., Español, P. and Ernst, M. H., "Dissipative Particle Dynamics with Energy Conservation:. Heat Conduction," International Journal of Modern Physics C, vol. 9 (8), pp. 1329-1338, 1998.

[40] Ball, R. C. and Melrose, J. R., "A simulation technique for many spheres in quasi-static motion under frame-invariant pair drag and Brownian forces," Physica A: Statistical Mechanics and its Applications, vol. 247 (1–4), pp. 444-472, 1997.

[41] Español, P., "Fluid particle dynamics: A synthesis of dissipative particle dynamics and smoothed particle dynamics," EPL (Europhysics Letters), vol. 39 (6), pp. 605-610, 1997.

[42] Español, P. and Warren, P., "Statistical Mechanics of Dissipative Particle Dynamics," EPL (Europhysics Letters), vol. 30 (4), pp. 191-196, 1995.

[43] Marsh, C. A., Backx, G. and Ernst, M. H., "Static and dynamic properties of dissipative particle dynamics," Physical Review E, vol. 56 (2), pp. 1676-1691, 1997.

[44] Reinecke, S. and Kremer, G. M., "A generalization of the Chapman-Enskog and Grad methods," Continuum Mech. Thermodyn, vol. 3 (3), pp. 155-167, 1991.

[45] Marsh, C. A. and Coveney, P. V., "Detailed balance and H -theorems for dissipative particle dynamics," Journal of Physics A: Mathematical and General, vol. 31 (31), pp. 6561-6568, 1998.

[46] Groot, R. D. and Warren, P. B., "Dissipative particle dynamics: Bridging the gap between atomistic and mesoscopic simulation," The Journal of Chemical Physics, vol. 107 (11), pp. 4423-4435, 1997.

[47] Flory, P. J., "Thermodynamics of High Polymer Solutions," The Journal of Chemical Physics, vol. 10 (1), pp. 51-61, 1942.

[48] Huggins, M. L., "Solutions of Long Chain Compounds," The Journal of Chemical Physics, vol. 9 (5), pp. 440-440, 1941.

[49] Lisal, M., Brennan, J. K. and Avalos, J. B., "Dissipative particle dynamics at isothermal, isobaric, isoenergetic, and isoenthalpic conditions using Shardlow-like splitting algorithms," Journal of Chemical Physics, vol. 135 (20), pp. 204105-18, 2011.

[50] Zhang, C. and Deem, M. W., "Multicanonical molecular dynamics by variable-temperature thermostats and variable-pressure barostats," The Journal of Chemical Physics, vol. 138 (3), pp. 034103-09, 2013.

[51] Sutton, A. P. and Chen, J., "Long-range Finnis–Sinclair potentials," Philosophical Magazine Letters, vol. 61 (3), pp. 139-146, 1990.

[52] Malescio, G., "Intermolecular potentials - past, present, future," Nat Mater, vol. 2 (8), pp. 501-503, 2003.

[53] Stone, A. J., "Intermolecular Potentials," Science, vol. 321 (5890), pp. 787-789, 2008.

[54] Mie, G., "Zur kinetischen Theorie der einatomigen Körper," Annalen der Physik, vol. 316 (8), pp. 657-697, 1903.

[55] Morse, P. M., "Diatomic Molecules According to the Wave Mechanics. II. Vibrational Levels," Physical Review, vol. 34 (1), pp. 57-64, 1929.

[56] Jones, J. E., "On the Determination of Molecular Fields. II. From the Equation of State of a Gas," Proceedings of the Royal Society of London. Series A, vol. 106 (738), pp. 463-477, 1924.

[57] Smith, G. D. and Bharadwaj, R. K., "Quantum Chemistry Based Force Field for Simulations of HMX," The Journal of Physical Chemistry B, vol. 103 (18), pp. 3570-3575, 1999.

[58] Mishin, Y., Farkas, D., Mehl, M. J. and Papaconstantopoulos, D. A., "Interatomic potentials for monoatomic metals from experimental data and ab initio calculations," Physical Review B, vol. 59 (5), pp. 3393-3407, 1999.

[59] Stoneham, A. M. and Harding, J. H., "INTERATOMIC POTENTIALS IN SOLID-STATE CHEMISTRY," Annual Review of Physical Chemistry, vol. 37, pp. 53-80, 1986.

[60] Zhang, Y., Pan, M.-X. and Wang, W.-H., "Mie Potential and Equation of State of $Zr_{48}Nb_8Cu_{14}Ni_{12}Be_{18}$ Bulk Metallic Glass," Chinese Physics Letters, vol. 18 (6), pp. 805-807, 2001.

[61] Bridgman, P. W., "Pressure-Volume Relations for Seventeen Elements to 100,000 Kg/Cm^3," Proceedings of the American Academy of Arts and Sciences, vol. 74 (13), pp. 425-440, 1942.

[62] Magomedov, M. N., "The calculation of the parameters of the Mie-Lennard-Jones potential," High Temp, vol. 44 (4), pp. 513-529, 2006.

[63] Lafitte, T., Apostolakou, A., Avendaño, C., Galindo, A., Adjiman, C. S., Müller, E. A. and Jackson, G., "Accurate statistical associating fluid theory for chain

molecules formed from Mie segments," The Journal of Chemical Physics, vol. 139 (15), pp. 154504-37, 2013.

[64] Girifalco, L. A. and Weizer, V. G., "Application of the Morse Potential Function to Cubic Metals," Physical Review, vol. 114 (3), pp. 687-690, 1959.

[65] Lincoln, R. C., Koliwad, K. M. and Ghate, P. B., "Morse-Potential Evaluation of Second- and Third-Order Elastic Constants of Some Cubic Metals," Physical Review, vol. 157 (3), pp. 463-466, 1967.

[66] Lee, A. R., Kalotas, T. M. and Adams, N. A., "Modified Morse Potential for Diatomic Molecules," Journal of Molecular Spectroscopy, vol. 191 (1), pp. 137-141, 1998.

[67] Zarkova, L. and Hohm, U., "Effective (n-6) Lennard-Jones Potentials with Temperature-Dependent Parameters Introduced for Accurate Calculation of Equilibrium and Transport Properties of Ethene, Propene, Butene, and Cyclopropane†," Journal of Chemical & Engineering Data, vol. 54 (6), pp. 1648-1655, 2009.

[68] Al-Matar, A. K., Tobgy, A. H. and Suleiman, I. A., "The phase diagram of the Lennard-Jones fluid using temperature dependent interaction parameters," Mol. Simul., vol. 34 (3), pp. 289-294, 2008.

[69] Abell, G. C., "Empirical chemical pseudopotential theory of molecular and metallic bonding," Physical Review B, vol. 31 (10), pp. 6184-6196, 1985.

[70] Brenner, D. W., Shenderova, O. A., Harrison, J. A., Stuart, S. J., Ni, B. and Sinnott, S. B., "A second-generation reactive empirical bond order (REBO) potential energy expression for hydrocarbons," Journal of Physics: Condensed Matter, vol. 14 (4), pp. 783-802, 2002.

[71] Hehr, B. D., Hawari, A. I. and Gillette, V. H., "Molecular dynamics simulations of graphite at high temperatures," Nuclear Technology, vol. 160 (2), pp. 251-256, 2007.

[72] Ackland, G. J., "Temperature dependence in interatomic potentials and an improved potential for Ti," Journal of Physics: Conference Series, vol. 402 (1), pp. 012001-09, 2012.

[73] Holian, B. L., Voter, A. F., Wagner, N. J., Ravelo, R. J., Chen, S. P., Hoover, W. G., Hoover, C. G., Hammerberg, J. E. and Dontje, T. D., "Effects of pairwise versus many-body forces on high-stress plastic deformation," Physical Review A, vol. 43 (6), pp. 2655-2661, 1991.

[74] Bringa, E. M., Cazamias, J. U., Erhart, P., Stölken, J., Tanushev, N., Wirth, B. D., Rudd, R. E. and Caturla, M. J., "Atomistic shock Hugoniot simulation of single-crystal copper," Journal of Applied Physics, vol. 96 (7), pp. 3793-3799, 2004.

[75] Zimmerman, J. A., Winey, J. M. and Gupta, Y. M., "Elastic anisotropy of shocked aluminum single crystals: Use of molecular dynamics simulations," Physical Review B, vol. 83 (18), pp. 184113-07, 2011.

[76] Daw, M. S. and Baskes, M. I., "Embedded-atom method: Derivation and application to impurities, surfaces, and other defects in metals," Physical Review B, vol. 29 (12), pp. 6443-6453, 1984.

[77] Germann, T. C., Holian, B. L., Lomdahl, P. S. and Ravelo, R., "Orientation Dependence in Molecular Dynamics Simulations of Shocked Single Crystals," Physical Review Letters, vol. 84 (23), pp. 5351-5354, 2000.

[78] Berne, B. J. and Pechukas, P., "Gaussian Model Potentials for Molecular Interactions," The Journal of Chemical Physics, vol. 56 (8), pp. 4213-4216, 1972.

[79] Gay, J. G. and Berne, B. J., "Modification of the overlap potential to mimic a linear site--site potential," The Journal of Chemical Physics, vol. 74 (6), pp. 3316-3319, 1981.

[80] Cleaver, D. J., Care, C. M., Allen, M. P. and Neal, M. P., "Extension and generalization of the Gay-Berne potential," Physical Review E, vol. 54 (1), pp. 559-567, 1996.

[81] Berardi, R., Fava, C. and Zannoni, C., "A generalized Gay-Berne intermolecular potential for biaxial particles," Chemical Physics Letters, vol. 236 (4–5), pp. 462-468, 1995.

[82] Stillinger, F. H. and Weber, T. A., "Computer simulation of local order in condensed phases of silicon," Physical Review B, vol. 31 (8), pp. 5262-5271, 1985.

[83] Smith, G. D., Bharadwaj, R. K., Bedrov, D. and Ayyagari, C., "Quantum-Chemistry-Based Force Field for Simulations of Dimethylnitramine," The Journal of Physical Chemistry B, vol. 103 (4), pp. 705-713, 1999.

[84] Mishin, Y., "Interatomic Potentials for Metals," in *Handbook of Materials Modeling*, edited by S. Yip (Springer Netherlands, 2005), pp. 459-478.

[85] Reith, D., Pütz, M. and Müller-Plathe, F., "Deriving effective mesoscale potentials from atomistic simulations," Journal of Computational Chemistry, vol. 24 (13), pp. 1624-1636, 2003.

[86] Forrest, B. M. and Suter, U. W., "Accelerated equilibration of polymer melts by time-coarse-graining," The Journal of Chemical Physics, vol. 102 (18), pp. 7256-7266, 1995.

[87] Bolhuis, P. G., Louis, A. A., Hansen, J. P. and Meijer, E. J., "Accurate effective pair potentials for polymer solutions," Journal of Chemical Physics, vol. 114 (9), pp. 4296-4311, 2001.

[88] Chennamsetty, N., Bock, H., Lísal, M. and Brennan, J. K., "An Introduction to Coarse-Graining Approaches: Linking Atomistic and Mesoscales," in *Process Systems Engineering* (Wiley-VCH Verlag GmbH & Co. KGaA, 2011), pp. 43-84.

[89] Izvekov, S. and Voth, G. A., "A Multiscale Coarse-Graining Method for Biomolecular Systems," The Journal of Physical Chemistry B, vol. 109 (7), pp. 2469-2473, 2005.

[90] Izvekov, S., Chung, P. W. and Rice, B. M., "Particle-based multiscale coarse graining with density-dependent potentials: Application to molecular crystals (hexahydro-1,3,5-trinitro-s-triazine)," The Journal of Chemical Physics, vol. 135 (4), pp. 064109-16, 2011.

[91] Mukherjee, B., Delle Site, L., Kremer, K. and Peter, C., "Derivation of Coarse Grained Models for Multiscale Simulation of Liquid Crystalline Phase Transitions," The Journal of Physical Chemistry B, vol. 116 (29), pp. 8474-8484, 2012.

[92] Steve, O. N., Carlos, F. L., Goundla, S. and Michael, L. K., "Coarse grain models and the computer simulation of soft materials," Journal of Physics: Condensed Matter, vol. 16 (15), pp. R481-R512, 2004.

[93] Oberbrodhage, J., Morgner, H., Tapia, O. and Siegbahn, H. O. G., "Molecular dynamics simulation of the free surface of liquid formamide," International Journal of Quantum Chemistry, vol. 63 (6), pp. 1123-1131, 1997.

[94] Böddeker, B. and Teichler, H., "Dynamics near free surfaces of molecular dynamics simulated $Ni_{0.5}Zr_{0.5}$ metallic glass films," Physical Review E, vol. 59 (2), pp. 1948-1956, 1999.

[95] Altenhoff, A. M., Walther, J. H. and Koumoutsakos, P., "A stochastic boundary forcing for dissipative particle dynamics," Journal of Computational Physics, vol. 225 (1), pp. 1125-1136, 2007.

[96] Revenga, M., Zúñiga, I. and Español, P., "Boundary conditions in dissipative particle dynamics," Computer Physics Communications, vol. 121–122 (0), pp. 309-311, 1999.

[97] Revenga, M., Zúñiga, I., Español, P. and Pagonabarraga, I., "Boundary Models in DPD," International Journal of Modern Physics C, vol. 09 (08), pp. 1319-1328, 1998.

[98] Wang, L., Ge, W. and Li, J., "A new wall boundary condition in particle methods," Computer Physics Communications, vol. 174 (5), pp. 386-390, 2006.

[99] Pivkin, I. V. and Karniadakis, G. E., "A new method to impose no-slip boundary conditions in dissipative particle dynamics," J. Comput. Phys., vol. 207 (1), pp. 114-128, 2005.

[100] Irving, J. H. and Kirkwood, J. G., "The Statistical Mechanical Theory of Transport Processes. IV. The Equations of Hydrodynamics," The Journal of Chemical Physics, vol. 18 (6), pp. 817-829, 1950.

[101] Hardy, R. J., "Formulas for determining local properties in molecular-dynamics simulations: Shock waves," The Journal of Chemical Physics, vol. 76 (1), pp. 622-628, 1982.

[102] Hardy, R. J., Root, S. and Swanson, D. R., "Continuum Properties from Molecular Simulations," AIP Conference Proceedings, vol. 620 (1), pp. 363-366, 2002.

[103] Zimmerman, J. A., WebbIII, E. B., Hoyt, J. J., Jones, R. E., Klein, P. A. and Bammann, D. J., "Calculation of stress in atomistic simulation," Modelling and Simulation in Materials Science and Engineering, vol. 12 (4), pp. S319-S332, 2004.

[104] Zimmerman, J. A., Jones, R. E. and Templeton, J. A., "A material frame approach for evaluating continuum variables in atomistic simulations," Journal of Computational Physics, vol. 229 (6), pp. 2364-2389, 2010.

[105] Shen, S. and Atluri, S. N., "Atomic-level Stress Calculation and Continuum-Molecular System Equivalence.," cmes, vol. 6 (1), pp. 91-104, 2004.

[106] Subramaniyan, A. K. and Sun, C. T., "Continuum interpretation of virial stress in molecular simulations," International Journal of Solids and Structures, vol. 45 (14–15), pp. 4340-4346, 2008.

[107] Eapen, J., Li, J. and Yip, S., "Statistical field estimators for multiscale simulations," Physical Review E, vol. 72 (5), pp. 056712-16, 2005.

[108] Yang, J. Z., Wu, X. and Li, X., "A generalized Irving--Kirkwood formula for the calculation of stress in molecular dynamics models," The Journal of Chemical Physics, vol. 137 (13), pp. 134104-17, 2012.

[109] Miller, M. S., "Thermophysical properties of cyclotrimethylenetrinitramine," Journal of Thermophysics and Heat Transfer, vol. 8 (4), pp. 803-805, 1994.

[110] Carslaw, H. S. and Jaeger, J. C., *Conduction of heat in solids*. (Clarendon Press, Oxford, 1959).

[111] Schwarz, R. B., Hooks, D. E., Dick, J. J., Archuleta, J. I. and Martinez, A. R., "Resonant ultrasound spectroscopy measurement of the elastic constants of cyclotrimethylene trinitramine," Journal of Applied Physics, vol. 98 (5), pp. 056106-03, 2005.

[112] Haycraft, J. J., Stevens, L. L. and Eckhardt, C. J., "The elastic constants and related properties of the energetic material cyclotrimethylene trinitramine (RDX) determined by Brillouin scattering," The Journal of Chemical Physics, vol. 124 (2), pp. 024712-11, 2006.